

FILTERED TRACTOGRAPHY

A Thesis
Presented to
The Academic Faculty

by

James G. Malcolm

In Partial Fulfillment
of the Requirements for the Degree
Doctor of Philosophy in the
Electrical and Computer Engineering

Georgia Institute of Technology
May 2011

FILTERED TRACTOGRAPHY

Approved by:

Yogesh Rathi, Advisor
Department of Psychiatry
Harvard Medical School

Allen Tannenbaum
Electrical and Computer Engineering
Georgia Institute of Technology

Anthony Yezzi
Electrical and Computer Engineering
Georgia Institute of Technology

Patricio Vela
Electrical and Computer Engineering
Georgia Institute of Technology

Hongwei Wu
Electrical and Computer Engineering
Georgia Institute of Technology

Sylvain Bouix
Department of Psychiatry
Harvard Medical School

Date Approved: 21 Oct 2010

TABLE OF CONTENTS

LIST OF TABLES	vi
LIST OF FIGURES	vii
SUMMARY	xii
I BACKGROUND	1
1.1 Overview of Diffusion Imaging	1
1.2 Modeling	2
1.2.1 Imaging the tissue	2
1.2.2 Parametric models	3
1.2.3 Nonparametric models	3
1.2.4 Regularization	4
1.2.5 Characterizing tissue	5
1.3 Tractography	6
1.3.1 Deterministic tractography	6
1.3.2 Probabilistic tractography	7
1.3.3 Global tractography	7
1.3.4 Validation	9
1.4 Applications	9
1.4.1 Volume segmentation	10
1.4.2 Fiber clustering	11
1.4.3 Connectivity	12
1.4.4 Tissue analysis	13
1.5 Summary	13
II FILTERED TRACTOGRAPHY	19
2.1 Summary	19
2.2 Modeling local fiber orientations	20
2.2.1 Diffusion tensors	21
2.2.2 Watson directional function	22
2.3 Estimating the fiber model	24

2.4	The algorithm	27
III	RESULTS	29
3.1	Tensors	29
3.1.1	Synthetic tractography	31
3.1.2	Angular resolution	32
3.1.3	Estimated quantities	33
3.1.4	Volume fractions	34
3.1.5	Three-fiber crossings	35
3.1.6	<i>In vivo</i> tractography	35
3.2	Watson directional functions	39
3.2.1	Signal reconstruction and angular resolution	40
3.2.2	<i>In vivo</i> tractography	40
IV	WEIGHTED MIXTURES	56
4.1	Summary	56
4.1.1	The weighted model	56
4.1.2	Constrained estimation	57
4.2	Experiments	58
4.2.1	Synthetic validation	59
4.2.2	<i>In vivo</i> tractography	60
4.3	Summary	62
V	VALIDATION	63
5.1	Summary	63
5.2	Results and Discussion	64
VI	TRACT-BASED STATISTICAL ANALYSIS	66
6.1	Summary	66
6.2	Introduction	66
6.3	Our contributions	68
6.4	Method	68
6.5	Tractography and fiber comparison	69
6.6	Results	72

6.6.1	Synthetic validation	72
6.6.2	<i>In vivo</i> model comparison	73
6.7	Conclusion	74
VII	SUMMARY	76
	REFERENCES	78

LIST OF TABLES

LIST OF FIGURES

<p>1.1 Comparison of various models within a coronal slice (a) passing through the corpus callosum. In (b) the original signal appears noisy. In (c) a single tensor fit provides a robust estimate of the principal diffusion direction. In (d) a two-tensor model is fit to planar voxels and the two axes are reported [118]. In (e) spherical harmonics provide a smoothed non-parametric estimate of the signal surface eliminating much of the noise seen in (b) [41].</p> <p>1.2 Cutaway showing tractography throughout the left hemisphere colored by FA to indicate diffusion strength [101]. From this view, the fornix and cingulum bundle are visible near the center.</p> <p>1.3 Tractography from the center of the corpus callosum (seed region in yellow). The single-tensor model (left) captures only the corona radiata and misses the lateral pathways known to exist. The two-tensor method [101] (right) reveals many of these missing pathways (highlighted in blue). (From [101])</p> <p>1.4 Segmenting the corpus callosum using the graph cut technique from [96] (side view). The Euclidean mapping (b) does not take into account the structure of the underlying tensor manifold. The Riemannian mapping (c) takes this structure into account when computing statistics and so produces a correct segmentation. (From [96])</p> <p>1.5 Full-brain streamline tractography clustered using affinity propagation [99]. Viewed from the outside (left) and inside cutting away the left hemisphere (right). Among the visible structures, we see the cingulum bundle (yellow), internal capsule (red), and arcuate (purple).</p> <p>1.6 Fronto-occipital fibers from the right hemisphere using streamline tractography and clustered into bundles (a) [99]. Viewing the most representative fiber in each bundle (b) we see a fiber from one cluster (red) that appears to have wandered off the pathway. (From [99])</p> <p>1.7 The brain viewed as a network of weighted connections. Each edge represents a possible connection and is weighted by the strength of that path. Many techniques from network analysis are applied to reveal hubs and subnetworks within this macroscopic view.</p> <p>1.8 Plotting FA as a function of arc-length to examine local fluctuations. Fibers are selected that connect the left and right seed regions (green). Notice how the FA from single-tensor (blue) is lower in regions of crossing compared to two-tensor FA (red). (From [97])</p> <p>1.9 System overview illustrating relation between the neural fibers, the measured scanner signal, and the unscented Kalman filter as it is used to estimate the local model. At each step, the filter uses its current model state ($\hat{\mathbf{x}}_t$) to predict the observed scanner signal ($\bar{\mathbf{y}}_{t+1 t}$) and then compares that against the actual measured signal (\mathbf{y}_t) in order to update its internal model state ($\hat{\mathbf{x}}_{t+1}$).</p>	<p>15</p> <p>16</p> <p>16</p> <p>17</p> <p>17</p> <p>17</p> <p>17</p> <p>18</p> <p>18</p> <p>18</p> <p>20</p>
-------------------------------------------------------------------------------------------------------------------------------------------------------------------------------------------------------------------------------------------------------------------------------------------------------------------------------------------------------------------------------------------------------------------------------------------------------------------------------------------------------------------------------------------------------------------------------------------------------------------------------------------------------------------------------------------------------------------------------------------------------------------------------------------------------------------------------------------------------------------------------------------------------------------------------------------------------------------------------------------------------------------------------------------------------------------------------------------------------------------------------------------------------------------------------------------------------------------------------------------------------------------------------------------------------------------------------------------------------------------------------------------------------------------------------------------------------------------------------------------------------------------------------------------------------------------------------------------------------------------------------------------------------------------------------------------------------------------------------------------------------------------------------------------------------------------------------------------------------------------------------------------------------------------------------------------------------------------------------------------------------------------------------------------------------------------------------------------------------------------------------------------------------------------------------------------------------------------------------------------------------------------------------------------------------------------------------------------------------------------------------------------------------------------------------------------------------------------------------------------------------------------------------------------------------------------------------------------------------------------------------------------------------------------------------------------------------------------------------------------------------------------------------------------------------------------------------------------------------------------------------------------------------------------------------------------------------------------------------------------------------------------------------------------------------------------------------------------------------------------------------------------	---------------------------------------------------------------------------------------------------------------

2.10 Comparison of tractography using a single-tensor model and the proposed two-component model with filtering. While the single-tensor model misses many of the lateral branches from the corpus callosum, the filter provides a stable estimate of the two-component model capable of revealing the lateral transcallosal pathways. Seed region indicated with yellow.	21
2.11 Watson directional functions are capable of representing various diffusion patterns and fiber orientations.	23
3.12 One fiber passing through an example synthetic field and the estimated ODFs within crossing region (<i>blue box</i>) using (unsharpened) spherical harmonics (SH) and the filter. The filter provides consistent angular resolution while SH modeling at those same locations sometimes misses or is off. Above and below the crossing region, the filter aligns both tensor components to fit the single-tensor signal.	30
3.13 The error in estimated crossing angle (a) and estimated fractional anisotropy (b)-(d) at various volume fractions: 50%-50% (top row), 60%-40% (middle row), 70%-30% (bottom row). Where appropriate, we compare among single-tensor least-squares (<i>green</i>), sharpened spherical harmonics (<i>red</i>), two-tensor Levenberg-Marquardt (<i>blue</i>), and the proposed filtered two-tensor (<i>black</i>). Through all examples, the filtered technique provides the most consistent and accurate results.	43
3.14 The filtered approach (<i>black</i>) is able to resolve three-fiber crossings with improved accuracy and at sharper angles compared to using sharpened spherical harmonics (<i>red</i>). Both low-noise and high-noise experiments are shown. . .	44
3.15 Tractography using various methods, seeded at the center of the corpus callosum. Single-tensor reconstructs only the dominate callosal radiata (a). Spherical harmonics pick up some of the lateral branches (b). Initializing a Levenberg-Marquardt solver with an independent single tensor estimate finds only the radiata (c), while initializing instead with its previous estimate (d) finds little more than spherical harmonics. Only filtered tractography picks up the lateral paths consistent with the underlying anatomy. Fibers exiting ± 22 mm around the mid-sagittal plane are indicated in <i>blue</i> . Seed region indicated in <i>yellow</i>	45
3.16 Tracing fibers originating from the center of the entire corpus callosum with views from above (<i>top rows</i>) and front-to-back (<i>bottom rows</i>). The proposed filtered tractography is able to find many of the lateral projections (<i>blue</i>) while single-tensor is unable to find any and few are found with sharpened spherical harmonics. Seed region indicated in <i>yellow</i>	46
3.17 Successive snapshots of filtered two-tensor tracing from both the corpus callosum (<i>red</i>) and internal capsule (<i>yellow</i>), viewed from right hemisphere. Here we see the lateral pathways from the corpus cross the motor tracts from the internal capsule.	46

3.18	The three-tensor filtered approach is able to trace through this intersection of the corticospinal tract (<i>blue</i>), corpus callosum (<i>red</i>), and superior longitudinal fasciculus (<i>green</i>).	47
3.19	A portion of the superior longitudinal fasciculus as it crosses a section of the lateral pathways emanating from the corpus callosum. These fibers were extracted using two regions of interest (<i>yellow</i>). While LM reconstructs several of these fibers, filtered estimation produces a more consistent bundle with deeper, uniform penetration into the frontal and occipital lobes. No such fibers were found using the comparison methods.	47
3.20	Tracing of the right cingulum bundle using various methods. From full-brain seeding, fibers were selected that passed through any two gates (<i>yellow</i>). While all methods here produce some false-positives (<i>e.g.</i> partial voluming onto the splenium, genu, or tapetum), the filtered methods appear to produce the fullest cingulum reconstructions.	48
3.21	Tracing of the right inferior fronto-occipital fasciculus using various methods. From full-brain seeding, fibers were selected that passed through any two gates (<i>yellow</i>). Spherical harmonics and Levenberg-Marquardt show sparse and irregular connectivity. Filtered single- and two-tensor results appear to have deeper and more uniform penetration into the occipital lobe.	48
3.22	A view of the previous figure from above. Note the consistent deeper penetration of the filtered techniques. The two-tensor method infiltrates many minor pathways into the temporal lobe.	49
3.23	Mean squared error (MSE) between reconstructed signal and ground truth signal at various crossing angles (<i>low-noise on left, high-noise on right</i>). Notice how the increased noise has little effect on the filter (<i>black</i>) compared to using matching pursuit (<i>blue</i>) or sharpened spherical harmonics (<i>red</i>).	49
3.24	Average angle error at various crossing angles comparing all three techniques: matching pursuit (<i>blue</i>), sharpened spherical harmonics (<i>red</i>), and the proposed filter (<i>black</i>). The filter provides stable and consistent estimation compared to either alternative technique. Each subfigure shows both the low-noise and high-noise experiments (<i>left, right</i>).	50
3.25	Filtered tractography picks up many fiber paths consistent with the underlying structures. Both single-tensor streamline and sharpened spherical harmonics are unable to find the majority of these pathways. Fibers existing ± 22 mm around the mid-sagittal plane are indicated in blue. Seed region indicated in yellow.	50
3.26	Closeup of upper right in Figure 3.25c and Figure 3.25d.	51
3.27	Closeup of frontal fibers in Figure 3.31c and Figure 3.31d viewed from above.	51
3.28	Frontal view with seeding in the internal capsule (<i>blue</i>). While both single-tensor and spherical harmonics tend to follow the dominant corticospinal tract to the primary motor cortex, the filtered approach follows many more pathways. Seed region indicated in yellow.	52

3.29	View from above showing cortical insertion points for each method. FA backdrop is taken near the top of the brain. The filtered approach shows more lateral insertions compared to single-tensor and spherical harmonic tracts.	53
3.30	Side view with seeding in the internal capsule (<i>yellow</i>). Filtered tractography finds many insertions into cortical regions of the parietal and occipital lobes. Seed region indicated in yellow.	54
3.31	Tracing fibers originating from the center of the entire corpus callosum with views from above (<i>top rows</i>) and front-to-back (<i>bottom rows</i>). The proposed filtered tractography is able to find many of the lateral projections (<i>blue</i>) while single-tensor is unable to find any and few are found with sharpened spherical harmonics. Seed region indicated in yellow.	55
4.32	Comparison of sharpened spherical harmonics (<i>red</i>) against filtered approach (<i>black</i>) over several different metrics: detection rate, angular resolution, estimated primary fiber weight (<i>rows, top to bottom</i>). Each column is a different primary fiber weighting. The filter provides superior detection rates, accurate angular resolution, and consistent weight estimation. Trendlines indicate mean while dashed bars indicate one standard deviation.	59
4.33	Filtered tractography picks up many fiber paths consistent with the underlying structures. Both single-tensor streamline and sharpened spherical harmonics are unable to find the majority of these pathways. Seed region indicated in yellow.	60
4.34	Tracing fibers originating from the center of the entire corpus callosum viewed from above. The proposed filtered tractography is able to find many of the lateral projections (<i>blue</i>) while single-tensor is unable to find any and few are found with sharpened spherical harmonics. Seed region indicated in yellow.	61
5.35	Baseline image from the synthetic phantom (3mm, $b=1500$) overlayed with ground truth and selected fiber tracts (colored) and seed points (white). The filter is capable of tracing through regions of crossing, branching, and fanning.	64
6.36	For each patient, we seed in three different cortical regions and select only those fibers that connect the hemispheres.	69
6.37	Single-tensor tractography finds no connections. Two-tensor passes through the region of crossing (<i>red/yellow boundary</i>). FA curves show drop in single-tensor FA (<i>blue</i>) in this region (<i>indicated by dashed white line</i>).	70
6.38	Two-tensor fibers overlayed with FA intensity using both models (<i>red to yellow is low to high</i>). Both methods show high FA in the corpus callosum but single-tensor FA drops as fibers enter the gray matter.	71
6.39	Estimated fractional anisotropy (FA) using single-tensor (<i>blue</i>) and two-tensor (<i>red</i>) models on synthetic data with known FA (<i>dashed black</i>). The two-tensor model accurately captures the FA across a wide range of angles and eigenvalues.	72

6.40 Average of various tensor metrics as a function of arc-length using single-tensor (*blue*) and two-tensor (*red*) models comparing normal patients (*solid lines*) with schizophrenic patients (*dotted lines*). Rows show FA, trace, eigenvalue ratio. Areas of statistical significance are indicated along the bottom (*black dashes indicate 95% confidence*). While each metric generally indicates the same area of significance (*looking down columns*), the areas of significance vary with each model (*comparing red and blue*)

73

SUMMARY

Computer vision encompasses a host of computational techniques to process visual information. Medical imagery is one particular area of application where data comes in various forms: X-rays, ultrasound probes, MRI volumes, EEG recordings, NMR spectroscopy, etc. This dissertation is concerned with techniques for accurate reconstruction of neural pathways from diffusion magnetic resonance imagery (dMRI).

This dissertation describes a filtered approach to neural tractography. Existing methods independently estimate the diffusion model at each voxel so there is no running knowledge of confidence in the estimation process. We propose using tractography to drive estimation of the local diffusion model. Toward this end, we formulate fiber tracking as recursive estimation: at each step of tracing the fiber, the current estimate is guided by those previous.

We argue that this approach is more accurate than conventional techniques. Experiments demonstrate that this filtered approach significantly improves the angular resolution at crossings and branchings. Further, we confirm its ability to trace through regions known to contain such crossing and branching while providing inherent path regularization.

We also argue that this approach is flexible. Experiments demonstrate using various models in the estimation process, specifically combinations of Watson directional functions and rank-2 tensors. Further, this dissertation includes an extension of the technique to weighted mixtures using a constrained filter.

CHAPTER I

BACKGROUND

1.1 *Overview of Diffusion Imaging*

The advent of diffusion magnetic resonance imaging (dMRI) has provided the opportunity for non-invasive investigation of neural architecture. While structural MRI has long been used to image soft tissue and bone, dMRI provides additional insight into tissue microstructure by measuring its microscopic diffusion characteristics. To accomplish this, the magnetic field induces the movement of water while the presence of cell membranes, fibers, or other macromolecules hinder this movement. By varying the direction and strength of the magnetic fields, we essentially use the water molecules as a probe to get a sense of the local tissue structure.

At the lowest level this diffusion pattern provides several insights. For example, in fibrous tissue the dominant direction of allowed diffusion corresponds the underlying direction of fibers. In addition, quantifying the anisotropy of the diffusion pattern can also provide useful biomarkers. Several models have been proposed to interpret scanner measurements, ranging from geometric abstractions to those with biological motivation. In Section 1.2 we will introduce various models and methods for interpreting the diffusion measurements.

By connecting these local orientation models, tractography attempts to reconstruct the neural pathways. Tracing out these pathways, we begin to see how neurons originating from one region connect to other regions and how well-defined those connections may be. Not only can we examine properties of the local tissue but we begin to see the global functional architecture of the brain, but for such studies, the quality of the results relies heavily on the chosen fiber representation and the method of reconstructing pathways. In Section 1.3 we will describe several techniques for tracing out pathways.

At the highest level, neuroscientists can use the results of local modeling and tractography to examine individuals or groups of individuals. In Section 1.4 we will survey

approaches to segment tissue with boundaries indistinguishable with structural MRI, apply network analysis to characterize the macroscopic neural architecture, reconstruct fiber bundles from individual fiber traces, and analyze groups of individuals.

1.2 Modeling

1.2.1 Imaging the tissue

The overall signal observed in an dMRI image voxel (millimetric) is the superposition of signals from many underlying molecules probing the tissue (micrometric). Thus, the image contrast is related to the strength of water diffusion. At each image voxel, diffusion is measured along a set of distinct gradients, $\mathbf{u}_1, \dots, \mathbf{u}_n \in \mathbb{R}^3$, producing the corresponding signal, $\mathbf{s} = [s_1, \dots, s_n]^T \in \mathbb{R}^n$. A general weighted formulation that relates the measured diffusion signal to the underlying fiber architecture may be written as,

$$s_i = s_0 \sum_j w_j e^{-b_j \mathbf{u}_i^T D_j \mathbf{u}_i}, \quad (1.1)$$

where s_0 is a baseline signal intensity, b_j is the b-value, an acquisition-specific constant, w_j are convex weights, and D_j is a tensor describing a diffusion pattern. One of the first acquisition schemes developed, diffusion tensor imaging (DTI) utilizes these measurements to compute a Gaussian estimate of the diffusion orientation and strength at each voxel [14, 26].

Going beyond this macroscopic description of diffusion, various higher resolution acquisition techniques have been developed to capture more information about the diffusion pattern. One of the first techniques, Diffusion Spectrum Imaging (DSI) measures the diffusion process at various scales by sampling densely throughout the voxel [61, 151]. From this, the Fourier transform is used to convert the signal to a diffusion probability distribution. Due to the large number of samples acquired (usually more than 256 gradient directions), this scheme provides a much more accurate description of the diffusion process. However, on account of the large acquisition time (of the order of 1-2 hours per subject), this technique is not typically used in clinical scans and its use is restricted to few research applications.

Instead of spatially sampling the diffusion in a lattice throughout the voxel, a spherical shell sampling could be used [143]. Using this sampling technique, the authors in [144]

demonstrated that the shape of the diffusion probability could be recovered from the images acquired on a single spherical shell. This significantly reduced the acquisition time, while providing most of the information about the underlying diffusion in the tissue. This naturally led to the application of techniques for estimating functions on a spherical domain. For example, Q-ball imaging (QBI) demonstrated a spherical version of the Fourier transform to reconstruct the probability diffusion as an isosurface [143].

To begin studying the microstructure of fibers with these imaging techniques, we need models to interpret these diffusion measurements. Such models fall broadly into two categories: parametric and nonparametric.

1.2.2 Parametric models

One of the simplest models of diffusion is a Gaussian distribution: an elliptic (anisotropic) shape indicating a strong diffusion direction while a more rounded surface (isotropic) indicating less certainty in any particular direction (see Figure 1.1c). While robust, assuming this Gaussian model is inadequate in cases of mixed fiber presence or more complex orientations where the signal may indicate a non-Gaussian pattern [6, 51, 146]. To handle these complex patterns, higher resolution imaging and more flexible parametric models have been proposed including mixtures of tensors [2, 22, 69, 84, 117, 118, 146] and directional functions [78, 105, 127]. While these typically require the number of components to be fixed or estimated separately, more continuous mixtures have also been proposed [73]. Further, biologically inspired models and tailored acquisition schemes have been proposed to estimate physical tissue microstructure [10, 11]; see [5] for more.

1.2.3 Nonparametric models

Nonparametric models can often provide more information about the diffusion pattern. Instead of modeling a discrete number of fibers as in parametric models, nonparametric techniques estimate a spherical orientation distribution function indicating potential fiber directions and the relative certainty thereof. For this estimation, an assortment of surface reconstruction methods have been introduced: Q-ball imaging to directly transform the signal into a probability surface [144], spherical harmonic representations [7, 41, 51, 66],

higher-order tensors [13, 17, 113], diffusion profile transforms [70, 114], deconvolution with an assumed single-fiber signal response [72, 141], and more. Figure 1.1e shows a spherical harmonic reconstruction of the signal. Compare this to the original signal in Figure 1.1b.

It is important to keep in mind that there is often a distinction made between the reconstructed diffusion orientation distribution function and the putative fiber orientation distribution function; while most techniques estimate the diffusion function, its relation to the underlying fiber function is still an open problem. Spherical convolution is designed to directly transform the signal into a fiber distribution [4, 7, 70, 141], yet diffusion sharpening strategies have been developed to deal with Q-ball and diffusion functions [43].

While parametric methods directly describe the principal diffusion directions, interpreting the diffusion pattern from model independent representations typically involves determining the number and orientation of principal diffusion directions present. A common technique is to find them as surface maxima of the diffusion function [28, 43, 66, 141], while another approach is to decompose a high-order tensor representation of the diffusion function into a mixture of rank-1 tensors [135].

1.2.4 Regularization

As in all physical systems, the measurement noise plays a nontrivial role, and so several techniques have been proposed to regularize the estimation. One could start by directly regularizing the MRI signal by designing filters based on the various signal noise models [1, 12, 81]. Alternatively, one could estimate the diffusion tensor field and then correct these estimated quantities [142]. For spherical harmonic modeling, a regularization term can be included in the least squares formulation [41, 66]. Attempts such as these to manipulate diffusion weighted images or tensor fields have received considerable attention regarding appropriate algebraic and numeric treatments [20, 49, 80, 142].

Instead of regularizing signal or model parameters directly, an alternative approach is to infer the underlying geometry of the vector field [132]. Another interesting approach treats each newly acquired diffusion image as a new system measurement. Since diffusion tensors and spherical harmonics can be estimated within a least-squares framework, one can

use a Kalman filter to update the estimate and optionally stop the scan when the model parameters converge [123]. Further, this online technique can be used to alter the gradient set so that, were the scan to be stopped early, the gradients up to that point are optimally spread (active imaging) [39].

1.2.5 Characterizing tissue

The goal of diffusion imaging is to draw inferences from the diffusion measurements. As a starting point, one often converts the diffusion weighted image volumes to a scalar volume much like structural MRI or CT images. Starting with the standard Gaussian diffusion tensor model, an assortment of scalar measures have been proposed to quantify the size, orientation, and shape of the diffusion pattern [18, 152]. For example, fractional anisotropy quantifies the deviation from an isotropic tensor, an appealing quantity because it corresponds to the strength of diffusion while remaining invariant to orientation. Derivatives of these scalar measures have also been proposed to capture more information about the local neighborhood [79, 134], and these measures have been extended to high-order tensors [115]. Further, a definition of generalized anisotropy has been proposed to directly characterize anisotropy in terms of variance in the signal, hence avoiding an assumed model [146]. While geometric in nature, studies have shown these to be reasonable proxy measures for neural myelination [21, 74, 108]. Some studies have also examined the sensitivity of such measures against image acquisition schemes [33, 153].

Meaningful visualization of diffusion images is difficult because of their multivariate nature, and much is lost when reducing the spectral signal down to scalar intensity volumes. Several geometric abstractions have been proposed to convey more information. Since the most common voxel model is still the Gaussian diffusion tensor, most of the effort has focused on visualizing this basic element. The most common glyph is an ellipsoid simultaneously representing the size, shape, and orientation; however, since tensors have six free parameters, more elaborate representations have been proposed to visualize these additional dimensions using color, shading, or subtle variations in shape [47, 80, 148, 152]. Apart from tensors, visualization strategies for other models have received comparatively little attention, the

typical approach being to simply to visualize the diffusion isosurface at each voxel.

A vast literature exists on methods of acquisition, modeling, reconstruction, and visualization of diffusion images. For a comprehensive view, we suggest [3, 40, 61, 106, 143, 152].

1.3 Tractography

To compliment the wide assortment of techniques for signal modeling and reconstruction, there is an equally wide range of techniques to infer neural pathways. At the local level, one may categorize them either as tracing individual connections between regions or as diffusing out to estimate the probability of connection between regions. In addition, more global approaches have been developed to consider, not just the local orientations, but the suitability of entire paths when inferring connections.

1.3.1 Deterministic tractography

Deterministic tractography involves directly following the diffusion pathways. Typically, one places several starting points (seeds) in one region of interest and iteratively traces from one voxel to the next, essentially path integration in a vector field. One terminates these fiber bundles when the local diffusion appears weak or upon reaching a target region. Figure 1.2 offers a glimpse from inside the brain using this basic approach. Often additional regions are used as masks to post-process results, *e.g.* pathways from region A but not touching region B.

In the single tensor model, standard streamline tractography follows the principal diffusion direction of the tensor [107], while multi-fiber models often include techniques for determining the number of fibers present or when pathways branch [60, 64, 84]. Since individual voxel measurements may be unreliable, several techniques have been developed for regularization. For example, using the estimate from the previous position [88, 157] as well as filtering formulations for path regularization [59] and model-based estimation [101]. The choice of model and optimization mechanism can drastically effect the final tracts. To illustrate, Figure 1.3 shows tractography from the center of the corpus callosum using a single-tensor model and a two-tensor model using the filtered technique from [101].

1.3.2 Probabilistic tractography

While discrete paths intuitively represent the putative fiber pathways of interest, they tend to ignore the inherent uncertainty in estimating the principle diffusion directions in each voxel. Instead of tracing discrete paths to connect voxels, one may instead query the probability of voxel-to-voxel connections given the diffusion probability distributions reconstructed in each voxel.

Several approaches have been developed based on sampling. For example, one might run streamline tensor tractography treating each as a Monte Carlo sample; the more particles that take a particular path, the more likely that particular fiber pathway [23, 27, 82, 116]. Another approach would be to consider more of the continuous diffusion field from Q-ball or other reconstructions [19, 53, 117, 119, 145, 156]. By making high curvature paths unlikely, path regularization can be naturally enforced within the probabilistic framework. Another approach is to propagate an arrival-time isosurface from the seed region out through the diffusion field, the front evolution force being a function of the local diffusivity [19, 32, 140].

Using the full diffusion reconstruction to guide particle diffusion has the advantage of naturally handling uncertainty in diffusion measurements, but for that same reason it tends toward diffuse tractography and false-positive connections. One option is to constrain diffusivity by fitting a model, thereby ensuring definite diffusion directions yet still taking into account some uncertainty [23, 53, 117]. A direct extension is to introduce a model selection mechanism to allow for additional components where appropriate [22, 52]. However, one could stay with the nonparametric representations and instead sharpen the diffusion profile to draw out the underlying fiber orientations [43, 139].

1.3.3 Global tractography

Despite advances in voxel modeling, discerning the underlying fiber configuration has proven difficult. For example, looking at a single voxel, the symmetry inherent in the diffusion measurements makes it difficult to tell if the observed pattern represents a fiber curving through the voxel or instead represents a fanning pattern. Reliable and accurate fiber resolution requires more information than that of a single voxel. For example, instead of estimating the

fiber orientation, one could instead infer the geometry of the entire neighborhood [133].

Going a step further, one could say that reliable and accurate connectivity resolution requires even more information, beyond simply a voxel neighborhood. In some respects, probabilistic tractography can be seen to take into account more global information. By spawning thousands of particles, each attempting to form an individual connection, probabilistic techniques are able to explore more possibilities before picking those that are likely [116]. However, if these particles still only look at the local signal as they propagate from one voxel to the next, then they remain susceptible to local regions of uncertainty. Even those with resampling schemes are susceptible since the final result is still a product of the method used in local tracing [27, 156].

A natural step to address such problems is to introduce global connectivity information into local optimization procedures of techniques mentioned above. The work of [71] does this by extending the local Bayesian formulation in [22] with an additional prior that draws upon global connectivity information in regions of uncertainty. Similarly, one could use an energetic formulation still with data likelihood and prior terms, but additionally introduce terms governing the number of components present [48].

Another approach is to treat the entire path as the parameter to be optimized and use global optimization schemes. For example, one could model pathways as piecewise linear with a data likelihood term based on signal fit and a prior on spatial coherence of those linear components [83, 129]. One advantage of this path-based approach is that it somewhat obviates the need for a multi-fiber voxel model; however, such a flexible global model dramatically increases the computational burden.

An alternative formulation is to find geodesic paths through the volume. Again using some form of data likelihood term, such methods then employ techniques for front propagation to find globally optimal paths of connection [50, 91, 109, 120, 124].

Tractography is often used in group studies which typically require a common atlas for inter-subject comparison. Beginning with the end in mind, one could determine a reference bundle as a template and use this to drive tractography. This naturally ensures both the general geometric form of the solution and a direct correspondence between subjects [46, 58].

Alternatively, the tract seeding and other algorithm parameters could be optimized until the tracts (data driven) approach the reference (data prior) [34]. Since this requires pre-specifying such a reference bundle, information that may be unavailable or difficult to obtain, one could even incorporate the formulation of the reference bundle into the optimization procedure itself [35].

1.3.4 Validation

In attempting to reconstruct neural pathways virtually, it is important to keep in mind the inherent uncertainty in such reconstructions. The resolution of dMRI scanners is at the level of 1-3mm while physical fiber axons are often an order of magnitude smaller in diameter—a relationship which leaves much room for error. Some noise or a complex fiber configuration could simply look like a diffuse signal and cause probabilistic tractography to stop in its tracks, while a few inaccurate voxel estimations could easily send the deterministic tracing off course to produce a false-positive connection. Even global methods could produce a tract that fits the signal quite well but incidentally jumps over an actual boundary in one or two voxels it thinks are noise. Consequently, a common question is: Are these pathways really present?

With this in mind, an active area of study is validating such results. Since physical dissection often requires weeks of tedious effort, many techniques have been used for validating these virtual dissections. A common starting point is to employ synthetic and physical phantoms with known parameters when evaluating new methods [122]. When possible, imaging before and after injecting radio-opaque dyes directly into the tissue can provide some of the best evidence for comparison [37,93]. Another powerful approach is to apply bootstrap sampling or other non-parametric statistical tests to judge the sensitivity and reproducibility of resulting tractography against algorithm parameters, image acquisition, and even signal noise [33,34,54,76,87,153].

1.4 Applications

Having outlined various models and methods of reconstructing pathways, we now briefly cover several methods of further analysis.

1.4.1 Volume segmentation

Medical image segmentation has a long history, much of it focused on scalar intensity-based segmentation of anatomy. For neural segmentation, structural MRI easily reveals the boundaries between gray-matter and white-matter, and anatomic priors have helped further segment some internal structures [121]; however, the boundaries between many structures in the brain are remain invisible with structural MRI alone. The introduction of dMRI has provided new discriminating evidence in such cases where tissue may appear homogeneous on structural MRI or CT but contain distinct fiber populations.

To begin, most work has focused segmentation of the estimated tensor fields. Using suitable metrics to compare tensors, these techniques often borrow directly from active contour or graph cut segmentation with the approach of separating distributions. For example, one could define a Gaussian distribution of tensors to approximate a structure of interest [38, 131]. For tissues with more heterogeneous fiber populations, *e.g.* the corpus callosum as it bends, such global parametric representations are unsuitable. For this, non-parametric approaches are more appropriate at capturing the variation throughout such structures [96, 128]. Another approach to capture such variation is to limit the parametric distributions to local regions of support, essentially robust edge detection [86].

In Figure 1.4 we see a graph cut segmentation of the corpus callosum [96]. The color-coded fractional anisotropy image is shown for visualization while segmentation was performed on the underlying tensor data. If statistics are computing ignoring the tensor manifold (Euclidean assumption), the final segmentation fails Figure 1.4b. If statistics are computing via a Riemannian mapping that respects this structure, the final segmentation is accurate Figure 1.4c. This highlights the need for appropriate algebraic treatment of tensors and other non-Euclidean models.

An altogether different approach to segmenting a structure is to divide it up according to where portions connect elsewhere. For example, the thalamus contains several nuclei indistinguishable in standard MR or even with contrast. After tracing connections from the thalamus to the cortex, one study demonstrated that grouping these connections revealed the underlying nuclei [24].

1.4.2 Fiber clustering

The raw output of full-brain tractography can produce hundreds of thousands of such tracings, an overwhelming amount of information. One approach to understanding and visualizing such results is to group individual tracings into fiber bundles. Such techniques are typically based around two important design choices: the method of comparing fibers, and the method of clustering those fibers.

In comparing two fibers, one often starts by defining a distance measure, these typically being based on some point-to-point correspondence between the fibers [36, 44, 111]. With this correspondence in hand, one of the most common distances is then to take the mean closest point distance between the two fibers (Hausdorff distance). An alternative is to transform each fiber to a new vector space with a natural norm, *e.g.* a fiber of any length can be encoded with only the mean and covariance of points along its path and then use the L₂ distance [29]. An altogether different approach is to consider the spatial overlap between fibers [149, 150]. Since full-brain tractography often contains many small broken fragments as it tries to trace out bundles, such fragments are often separated from their actual cluster. Measures of spatial overlap may be more robust in such cases. In each of these methods, fibers were only considered as sequences of points, *i.e.* connections and orientations were ignored. Recent work demonstrates that incorporating such considerations provides robust descriptors of fiber bundles [45].

Based on these distances, several methods have been developed to cluster the fibers. Spectral methods typically begin with the construction of a Gram matrix encoding the pairwise affinity between any two fibers. After which normalized cuts can be applied to partition the Gram matrix and hence the fibers [29]. Affinity propagation has recently been demonstrated as an efficient and robust alternative which automatically determines the number of clusters to support a specified cluster size preference [89, 99]. In Figure 1.5 shows how clustering can automatically reveal known structures and provide a more coherent view of the brain. In addition, clustering can be used to judge outliers. For example, Figure 1.6 reveals several streamlines that appear to have gone off track relative to the cluster centers.

Another clustering approach is to use the inner product space itself. For example, one can efficiently group directly on the induced manifold by iteratively joining fibers most similar until the desired clustering emerges [150]. To avoid construction of the large Gram matrix, variants of expectation maximization have been demonstrated to iteratively cluster fibers, an approach that naturally lends itself to incorporating anatomic priors [94, 111, 149]. Alternatively, one can begin with the end in mind by registering a reference fiber bundle template to patients thus obviating any need for later spatial normalization or correspondence [35].

1.4.3 Connectivity

While tissue segmentation can provide global cues of neural organization, it tells little of the contribution of individual elements. Similarly, while clustered tracings are easily visualized, deciphering the flood of information from full-brain tractography demands more comprehensive quantitative analysis. For this, much has been borrowed from network analysis to characterize the neural topology. To start, instead of segmenting fibers into bundles, one can begin by classifying voxels into hubs or subregions into subnetworks [55, 62, 63, 138].

Dividing the brain up into major functional hubs, one can then view it as a graphical network as in Figure 1.7. Each of these edges is then often weighted as a function of connection strength [63], but may also incorporate functional correlation to give further evidence of connectivity.

One of the first results of such analysis was the discovery of dense hubs linked by short pathways, a characteristic observed in many complex physical systems (small-world phenomena). Another interesting finding came from combining anatomic connections from dMRI with neuronal activity provided by fMRI [67]. They found that areas which are functionally connected are often not structurally connected, hence tractography alone does not provide the entire picture.

For a recent review of this emerging field of structural and functional network analysis, we recommend [30].

1.4.4 Tissue analysis

In forming population studies, there are several approaches for framing the analysis among patients. For example, voxel-based studies examine tissue characteristics in regions of interest [9]. Discriminant analysis has been applied to determine such regions [31]. Alternatively, one could also perform regression on the full image volume taking into account not only variation in diffusion but also in the full anatomy [130]. In contrast, tract-based studies incorporate the results of tractography to use fiber pathways as the frame of reference [44, 137], and several studies have demonstrated the importance of taking into account local fluctuations in estimated diffusion [36, 58, 94, 112, 154].

A common approach in many of these studies is to focus on characterizing individual pathways or bundles. To illustrate this analysis, Figure 1.8 shows fibers connecting a small region in each hemisphere. We then average FA plotted along the bundle as a function of arc-length. Further, we plot the FA from both single- and two-tensor models to show how different models often produce very different tissue properties [97].

Several reviews exist documenting the application and findings of using various methods [68, 85, 92].

1.5 *Summary*

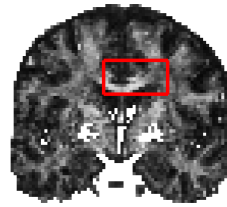
Diffusion MRI has provided an unprecedented view of neural architecture. With each year, we develop better image acquisition schemes, more appropriate diffusion models, more accurate pathway reconstruction, and more sensitive analysis.

In this survey, we began with an overview of the various imaging techniques and diffusion models. While many acquisition sequences have become widely distributed for high angular resolution imaging, work continues in developing sequences and models capable of accurate resolution of biological properties such as axon diameter and degree of myelination [5, 11]. We then reviewed various parametric models starting with the diffusion tensor up to various mixture models as well as high-order tensors. Work continues to develop more accurate and reliable model estimation by incorporating information from neighboring voxels [101, 133]. Further, scalar measures derived from these models similarly benefit from

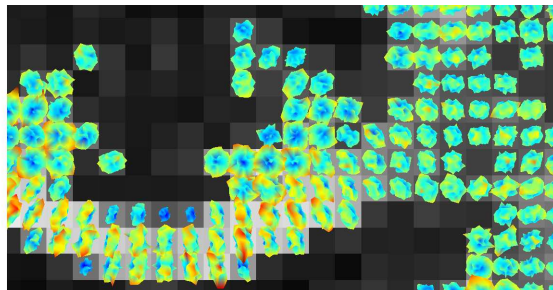
incorporating neighborhood information [134].

Next we outlined various methods of tractography to infer connectivity. Broadly, these techniques took either a deterministic or probabilistic approach. We also documented the recent trend toward global approaches, those that combine local voxel-to-voxel tracing with a sense of the full path [48, 129]. Even with such considerations, tractography is has proven quite sensitive to image acquisition and initial conditions, so much work has gone into validation. Common techniques are the use of physical phantoms [122] or statistical tests like bootstrap analysis [34, 76, 87].

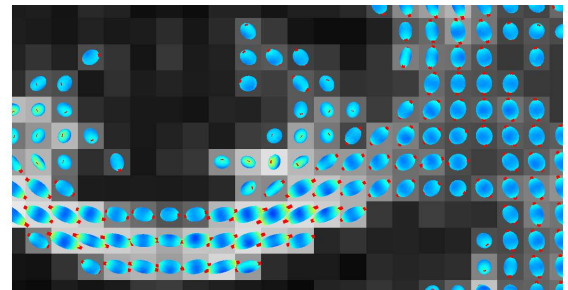
Finally, we briefly introduced several machine learning approaches to make sense of the information found in diffusion imagery. Starting with segmentation, several techniques for scalar intensity segmentation have been extended to dMRI. With the advent of full-brain tractography providing hundreds of thousands of fiber paths, the need to cluster connections into bundles has become increasingly important. The application of network analysis to connectivity appears to be an emerging area of research, especially in combination with alternate imaging modalities [30]. Finally, we noted several approaches to the analysis of neural tissue itself in regions of interest or along pathways.



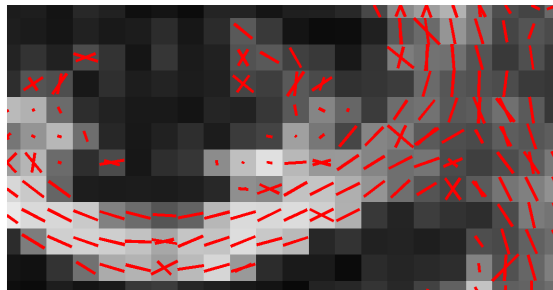
(a) Slice indicating region of interest



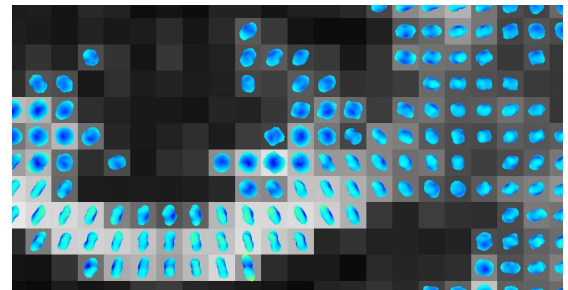
(b) Original signal



(c) Single-tensor with axis



(d) Two-tensor axes



(e) Spherical harmonic signal

Figure 1.1: Comparison of various models within a coronal slice (a) passing through the corpus callosum. In (b) the original signal appears noisy. In (c) a single tensor fit provides a robust estimate of the principal diffusion direction. In (d) a two-tensor model is fit to planar voxels and the two axes are reported [118]. In (e) spherical harmonics provide a smoothed non-parametric estimate of the signal surface eliminating much of the noise seen in (b) [41].



Figure 1.2: Cutaway showing tractography throughout the left hemisphere colored by FA to indicate diffusion strength [101]. From this view, the fornix and cingulum bundle are visible near the center.

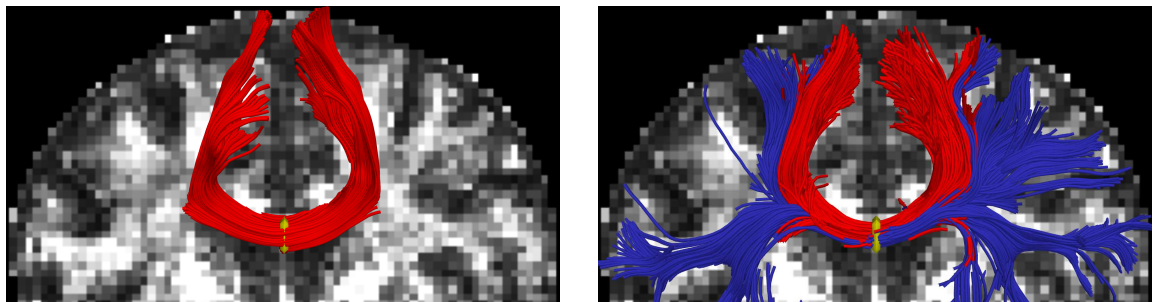
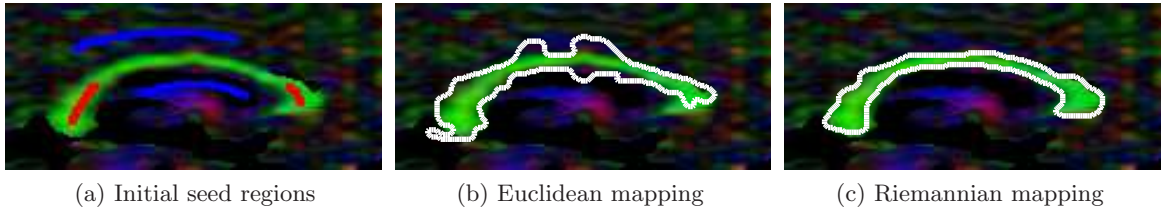


Figure 1.3: Tractography from the center of the corpus callosum (seed region in yellow). The single-tensor model (left) captures only the corona radiata and misses the lateral pathways known to exist. The two-tensor method [101] (right) reveals many of these missing pathways (highlighted in blue). (From [101])



(a) Initial seed regions (b) Euclidean mapping (c) Riemannian mapping

Figure 1.4: Segmenting the corpus callosum using the graph cut technique from [96] (side view). The Euclidean mapping (b) does not take into account the structure of the underlying tensor manifold. The Riemannian mapping (c) takes this structure into account when computing statistics and so produces a correct segmentation. (From [96])

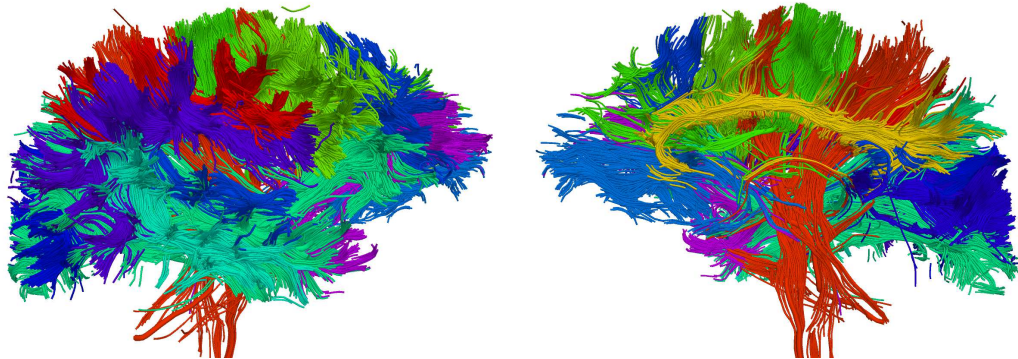
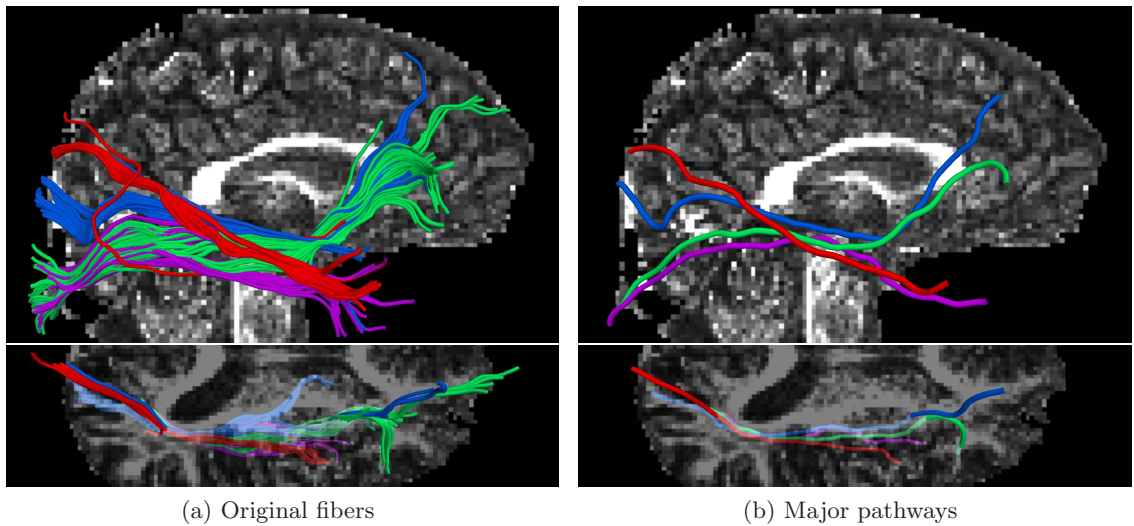


Figure 1.5: Full-brain streamline tractography clustered using affinity propagation [99]. Viewed from the outside (left) and inside cutting away the left hemisphere (right). Among the visible structures, we see the cingulum bundle (yellow), internal capsule (red), and arcuate (purple).



(a) Original fibers

(b) Major pathways

Figure 1.6: Fronto-occipital fibers from the right hemisphere using streamline tractography and clustered into bundles (a) [99]. Viewing the most representative fiber in each bundle (b) we see a fiber from one cluster (red) that appears to have wandered off the pathway. (From [99])

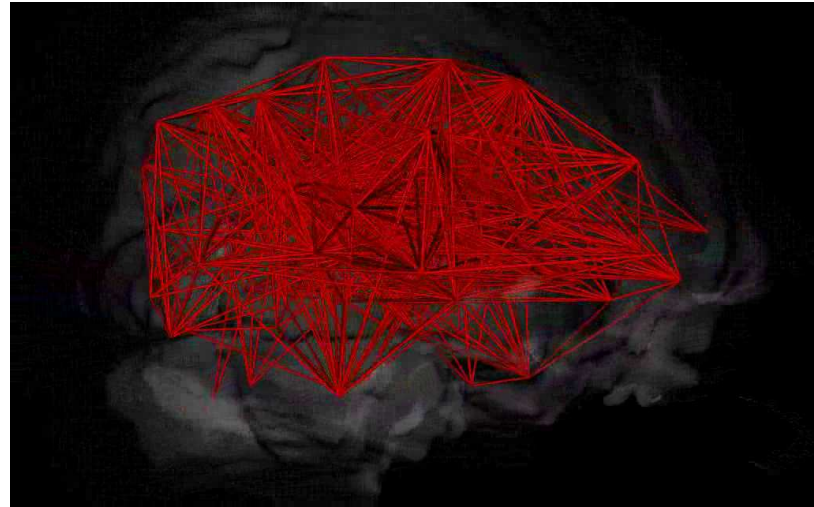


Figure 1.7: The brain viewed as a network of weighted connections. Each edge represents a possible connection and is weighted by the strength of that path. Many techniques from network analysis are applied to reveal hubs and subnetworks within this macroscopic view.

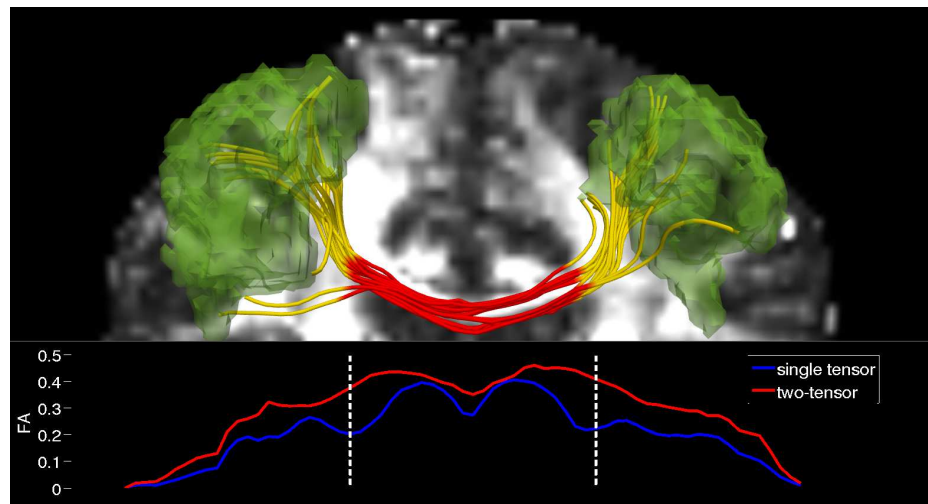


Figure 1.8: Plotting FA as a function of arc-length to examine local fluctuations. Fibers are selected that connect the left and right seed regions (green). Notice how the FA from single-tensor (blue) is lower in regions of crossing compared to two-tensor FA (red). (From [97])

CHAPTER II

FILTERED TRACTOGRAPHY

2.1 *Summary*

Nearly all approaches to tractography fit the model at each voxel independent of other voxels; however, tractography is a causal process: we arrive at each new position along the fiber based upon the diffusion found at the previous position.

We propose to we treat model estimation and tractography as such by placing this process within a causal filter. As we examine the signal at each new position, the filter recursively updates the underlying local model parameters, provides the variance of that estimate, and indicates the direction in which to propagate tractography. Figure 2.9 provides an overview of this recursive process.

To begin estimating within a finite dimensional filter, we model the diffusion signal using a mixture of parametric directional functions. We choose parametric models since they provide a compact representation of the signal parameterized by the principal diffusion direction and scaling parameters influencing anisotropy, and further allows analytic reconstruction of the oriented diffusion function from those parameters [103, 127]. This enables estimation directly from the raw signal without separate preprocessing or regularization. Because the signal reconstruction is nonlinear, we use the unscented Kalman filter to estimate the model parameters and then propagate in the most consistent direction. Using causal estimation in this way yields inherent path regularization and accurate fiber resolution at crossing angles not found with independent optimization. In a loop, the filter estimates the model at the current position, moves a step in the most consistent direction, and then begins estimation again. Since each iteration begins with a near-optimal solution provided by the previous estimation, the convergence of model fitting is improved and many local minima are naturally avoided. This approach generalizes to arbitrary fiber model with finite dimensional parameter space. The bulk of this dissertation is found among [101–103].

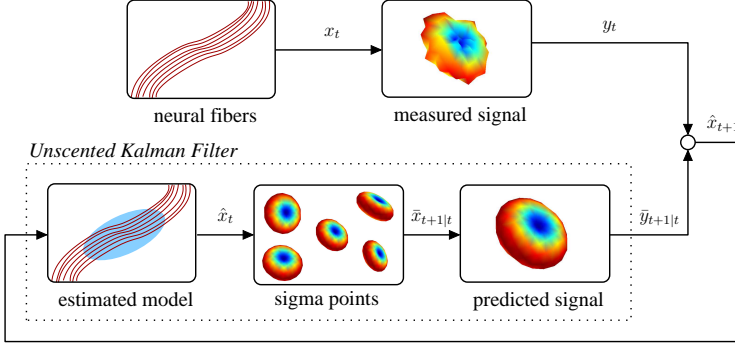


Figure 2.9: System overview illustrating relation between the neural fibers, the measured scanner signal, and the unscented Kalman filter as it is used to estimate the local model. At each step, the filter uses its current model state (\hat{x}_t) to predict the observed scanner signal ($\bar{y}_{t+1|t}$) and then compares that against the actual measured signal (y_t) in order to update its internal model state (\hat{x}_{t+1}).

Several studies have specific relevance to this present work because of their use of a filtering strategy in either orientation estimation or tractography. In extending standard streamline tractography to enhance path regularization, [59] move curve integration into a linear Kalman filter while [157] incorporate a moving least squares estimator. Alternatively, one could use a particle filter to place a prior on the direction of propagation [156]. Since these methods model only the position of the fiber, not the local fiber model, they are inherently focused on path regularization rather than estimating the underlying fiber structure. Finally, [123] proposed using a linear Kalman filter for online, direct estimation of either single-tensor or harmonic coefficients while successive diffusion image slices are acquired, while [39] revisited the technique to account for proper regularization and proposed a method to quickly determine optimal gradient set orderings.

Section 2.2 provides the necessary background on modeling the measurement signal using directional functions and defines the specific fiber models employed in this study. Then, Section 2.3 describes how this model may be estimated using an unscented Kalman filter.

2.2 Modeling local fiber orientations

In diffusion weighted imaging, image contrast is related to the strength of water diffusion, and our goal is to accurately relate these signals to an underlying model of fiber orientation.

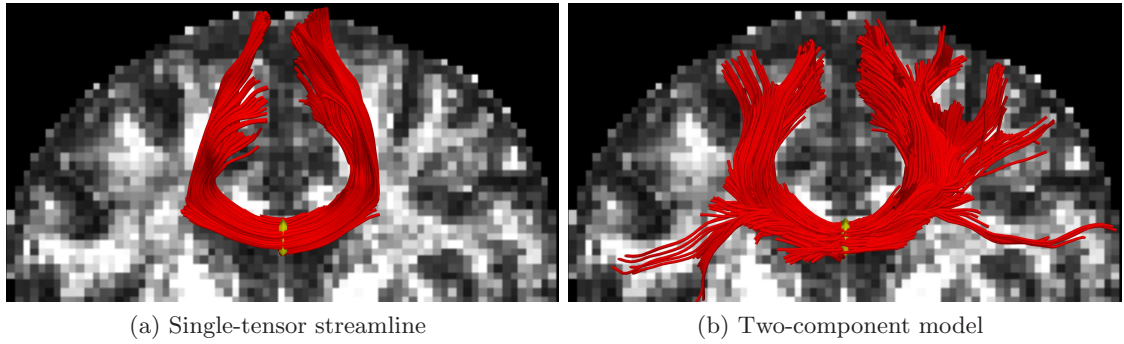


Figure 2.10: Comparison of tractography using a single-tensor model and the proposed two-component model with filtering. While the single-tensor model misses many of the lateral branches from the corpus callosum, the filter provides a stable estimate of the two-component model capable of revealing the lateral transcallosal pathways. Seed region indicated with yellow.

At each image voxel, diffusion is measured along a set of distinct gradients, $\mathbf{u}_1, \dots, \mathbf{u}_n \in \mathbb{S}^2$ (on the unit sphere), producing the corresponding signal, $\mathbf{s} = [s_1, \dots, s_n]^T \in \mathbb{R}^n$. For voxels containing a mixed diffusion pattern, a general weighted formulation may be written as,

$$s_i = s_0 \sum_j w_j e^{-b\mathbf{u}_i^T D_j \mathbf{u}_i}, \quad (2.2)$$

where s_0 is a baseline signal intensity, b is an acquisition-specific constant, w_j are convex weights, and D_j is a tensor matrix describing a diffusion pattern.

We now provide definition to the two primary models employed in this work: equally weighted diffusion tensors [101, 103] and Watson directional functions [127]. Later in chapter 4, we return to extend the method to weighted mixtures of diffusion tensors which requires a different filtering scheme [102].

2.2.1 Diffusion tensors

From the general mixture model above (Equation (1.1)), we choose to start with two components. This choice is guided by several previous studies which found two-fiber models to be sufficient at $b = 1000$ [22, 60, 84, 118, 146, 155]. Also, we assume the shape of each tensor to be ellipsoidal, *i.e.* there is one dominant principal diffusion direction \mathbf{m} with eigenvalue λ_1 and the remaining orthonormal directions have equal eigenvalues $\lambda_2 = \lambda_3$ (as in [53, 78, 117, 118]). Last, as in the study of [155], we fix the weights so that each component

contributes equally. While assuming equally-weighted compartments may limit flexibility, we found that the eigenvalues adjust to fit the signal in much the same way a fully weighted model would adjust. We will revisit this in the experiments and discussion (Section 3.1.4).

These assumptions then leave us with the following model used in this study:

$$s_i = \frac{s_0}{2} e^{-bu_i^T D_1 \mathbf{u}_i} + \frac{s_0}{2} e^{-bu_i^T D_2 \mathbf{u}_i}, \quad (2.3)$$

where D_1, D_2 are each expressible as, $D = \lambda_1 \mathbf{m} \mathbf{m}^T + \lambda_2 (\mathbf{p} \mathbf{p}^T + \mathbf{q} \mathbf{q}^T)$, with $\mathbf{m}, \mathbf{p}, \mathbf{q} \in \mathbb{S}^2$ forming an orthonormal basis aligned to the principal diffusion direction \mathbf{m} . The free model parameters are then $\mathbf{m}_1, \lambda_{11}, \lambda_{21}$, $\mathbf{m}_2, \lambda_{12}$, and λ_{22} . In our current implementation, we restrict each λ to be positive. Extending off the two-tensor model, we can directly formulate a three-tensor version:

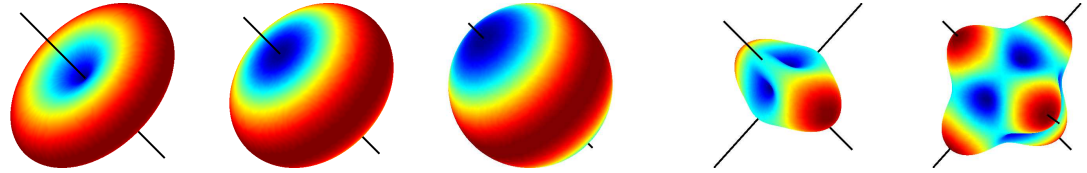
$$s_i = \frac{s_0}{3} \sum_{j=1}^3 e^{-bu_i^T D_j \mathbf{u}_i}, \quad (2.4)$$

with the additional parameters $\mathbf{m}_3, \lambda_{13}$, and λ_{23} .

2.2.2 Watson directional function

Considering a single tensor, we now follow the formulation of Rathi et al. [127] to define the Watson directional function which approximates the apparent diffusion pattern. We begin by noting that any diffusion tensor D can be decomposed as $D = U \Lambda U^T$, where U is a rotation matrix and Λ is a diagonal matrix with eigenvalues $\{\lambda_1, \lambda_2, \lambda_3\}$. These eigenvalues determine the shape of the tensor: ellipsoidal, planar, and spherical. For example, if $\lambda_1 > \lambda_2 > \lambda_3$, then the shape is ellipsoidal with the major axis of the ellipsoid pointing to the eigenvector corresponding to λ_1 . Intuitively, it represents strong diffusion along that particular direction. When $\lambda_1 = \lambda_2 > \lambda_3$, the shape is planar indicating diffusion along orthogonal directions, and finally, when $\lambda_1 = \lambda_2 = \lambda_3$, the diffusion is spherical (isotropic).

The most common of these configurations is ellipsoidal with principal diffusion direction \mathbf{m} and eigenvalue λ_1 , and hence the first step in introducing directional functions is to approximate the tensor by its first eigenvector expansion: $D \approx \lambda_1 \mathbf{m} \mathbf{m}^T$. Using this, each



(a) Reconstructed signals for strong diffusivity ($k = 2$), weak diffusivity ($k = 0.5$), and isotropic diffusion patterns ($k = 0.01$).
(b) Signals for two-fiber and three-fiber mixtures.

Figure 2.11: Watson directional functions are capable of representing various diffusion patterns and fiber orientations.

exponent in Equation (1.1) may then be rewritten,

$$-b\mathbf{u}_i^T D \mathbf{u}_i \approx -b\lambda_1 \mathbf{u}_i^T (\mathbf{m} \mathbf{m}^T) \mathbf{u}_i \quad (2.5)$$

$$= -b\lambda_1 (\mathbf{u}_i^T \mathbf{m})^2 \quad (2.6)$$

$$= -k (\mathbf{u}_i^T \mathbf{m})^2, \quad (2.7)$$

where the scalar k concentration parameter determines the degree of anisotropy. Finally, the general model may be restated:

$$s_i = A \sum_j w_j e^{-k_j (\mathbf{u}_i^T \mathbf{m}_j)^2}, \quad (2.8)$$

where A is a normalization constant such that $\|\mathbf{s}\| = 1$. For purposes of comparison, this normalization will also be done to signals obtained from scanner. Note that, while the diffusion tensor requires six parameters, these Watson functions require four parameters: three for the orientation vector \mathbf{m} and one concentration parameter k . Employing a spherical representation can further reduce the unit vector \mathbf{m} to two spherical coordinates. Figure 2.11a demonstrates how adjusting the k -value produces different diffusion patterns, and Figure 2.11b illustrates two multi-fiber configurations.

From this general mixture model, we choose to start with a restricted form involving two equally-weighted Watson functions. This choice is guided by several previous studies. Behrens et al. [22] showed that at a b -value of 1000 ms/mm^2 the maximum number of detectable fibers is two. Several other studies have also found two-fiber models to be sufficient [84, 118, 146, 155]. Using this as a practical guideline, we started with a mixture of two Watson functions as our local fiber model. Further, following the study of [155],

we assume an equal combination (50%-50%) of the two Watson functions. While the effect of this second choice appears to have little to no effect on experiments, we have yet to quantify any potential loss in accuracy. These assumptions leave us with the following two-fiber model used in this study:

$$s_i = \frac{A}{2} \left(e^{-k_1(\mathbf{u}_i^T \mathbf{m}_1)^2} + e^{-k_2(\mathbf{u}_i^T \mathbf{m}_2)^2} \right). \quad (2.9)$$

where k_1 and \mathbf{m}_1 parameterize the first Watson function, k_2 and \mathbf{m}_2 parameterize the second, and A is again a normalization constant such that $\|\mathbf{s}\| = 1$. Thus, the equally-weighted two-fiber model is fully described by the following parameters: k_1 , \mathbf{m}_1 , k_2 , \mathbf{m}_2 . Extending off the two-Watson model, we can directly formulate the equally-weighted three-Watson model:

$$s_i = \frac{A}{3} \sum_{j=1}^3 e^{-k_j(\mathbf{u}_i^T \mathbf{m}_j)^2}, \quad (2.10)$$

with the additional parameters k_3 and \mathbf{m}_3 .

Finally, from such parameters, Rathi et al. [127] describe how one may compute the ODF analytically by applying the Funk-Radon transform directly to Equation (2.8). The ODF can be reconstructed directly from the same parameters describing the signal without a separate estimation process. For the two-Watson model (Equation (2.9)) the ODF is approximated by,

$$f_i = \frac{B}{2} \left(e^{-\frac{k_1}{2}(1-(\mathbf{u}_i^T \mathbf{m}_1)^2)} + e^{-\frac{k_2}{2}(1-(\mathbf{u}_i^T \mathbf{m}_2)^2)} \right), \quad (2.11)$$

where B is a normalization factor such that $\sum_i f_i = 1$.

2.3 Estimating the fiber model

Given the measured scanner signal at a particular voxel, we want to estimate the underlying model parameters that explain this signal. As in streamline tractography, we treat the fiber as the trajectory of a particle which we trace out. At each step, we examine the measured signal at that position, estimate the underlying model parameters, and propagate forward in the most consistent direction. Figure 2.9 illustrates this filtering process.

To use a state-space filter for estimating the model parameters, we need the application-specific definition of four filter components:

1. The system state \mathbf{x} : the model parameters
2. The state transition $f[\cdot]$: how the model changes as we trace the fiber
3. The observation $h[\cdot]$: how the signal appears given a particular state
4. The measurement \mathbf{y} : the actual signal obtained from the scanner

For our state, we directly use the model parameters, thus the two-fiber model in Equation (2.9) has the following state vector:

$$\mathbf{x} = [\mathbf{m}_1 \ k_1 \ \mathbf{m}_2 \ k_2]^T, \quad \mathbf{m} \in \mathbb{S}^2, k \in \mathbb{R}. \quad (2.12)$$

While each \mathbf{m} could be represented in a reduced spherical form, the antipodes of the spherical parameterization would then introduce nonlinearities which complicate estimation. For the state transition we assume identity dynamics; the local fiber configuration does not undergo drastic change from one position to the next. Our observation is the signal reconstruction, $\mathbf{y} = \mathbf{s} = [s_1, \dots, s_n]^T$ using s_i from Equation (2.9), and our measurement is the actual signal interpolated directly from the diffusion weighted images at the current position.

Since the signal reconstruction is a nonlinear process, we employ an unscented Kalman filter to perform nonlinear estimation. Similar to classical linear Kalman filtering, the unscented version seeks to reconcile the predicted state of the system with the measured state and addresses the fact that those two processes (prediction and measurement) may be nonlinear or unknown. It does this in two phases: first it uses the system transition model to predict the next state and observation, and then it uses the new measurement to correct that state estimate. In what follows, we present the algorithmic application of the filter. For more thorough treatments, see [77, 147].

It is important to note two alternative techniques for nonlinear estimation. First, particle filters are commonly used to provide a multi-modal estimate of unknown systems. With respect to an n -dimensional state space, particle filters require the number of particles to be exponential to properly explore the state space. In contrast, the unscented filter requires only $2n + 1$ particles (sigma points) for a Gaussian estimate that space. Further, for many slowly varying systems, the multi-modal estimate is unnecessary: from one voxel to the

next, fibers tend not to change direction drastically. Second, an extended Kalman filter may also be used to provide a Gaussian estimate after linearizing the system; however, the unscented Kalman filter provides a more accurate estimate with equivalent computational cost and altogether avoids the attempt at linearization [77, 90, 147].

Suppose the system of interest is at time t and we have a Gaussian estimate of its current state with mean, $\mathbf{x}_t \in \mathbb{R}^n$, and covariance, $P_t \in \mathbb{R}^{n \times n}$. Prediction begins with the formation of a set $\mathbf{X}_t = \{\mathbf{x}_i\} \subset \mathbb{R}^n$ of $2n + 1$ *sigma point* states with associated convex weights, $w_i \in \mathbb{R}$, each a perturbed version of the current state. We use the covariance, P_t , to distribute this set:

$$\begin{aligned}\mathbf{x}_0 &= \mathbf{x}_t & w_0 &= \kappa/(n + \kappa) & w_i &= w_{i+n} = \frac{1}{2(n+\kappa)} \\ \mathbf{x}_i &= \mathbf{x}_t + \left[\sqrt{(n + \kappa)P_t} \right]_i & \mathbf{x}_{i+n} &= \mathbf{x}_t - \left[\sqrt{(n + \kappa)P_t} \right]_i\end{aligned}\quad (2.13)$$

where $[A]_i$ denotes the i^{th} column of matrix A and κ is an adjustable scaling parameter ($\kappa = 0.01$ in all experiments). Next, this set is propagated through the state transition function, $\hat{\mathbf{x}} = f[\mathbf{x}] \in \mathbb{R}^n$, to obtain a new predicted sigma point set: $\mathbf{X}_{t+1|t} = \{f[\mathbf{x}_i]\} = \{\hat{\mathbf{x}}_i\}$. Since in this study we assume the fiber configuration does not change drastically as we follow it from one voxel to the next, we may write this identity transition as, $\mathbf{x}_{t+1|t} = f[\mathbf{x}_t] = \mathbf{x}_t$. These are then used to calculate the predicted system mean state and covariance,

$$\begin{aligned}\bar{\mathbf{x}}_{t+1|t} &= \sum_i w_i \hat{\mathbf{x}}_i, \\ P_{xx} &= \sum_i w_i (\hat{\mathbf{x}}_i - \bar{\mathbf{x}}_{t+1|t}) (\hat{\mathbf{x}}_i - \bar{\mathbf{x}}_{t+1|t})^T + Q,\end{aligned}\quad (2.14)$$

where Q is the injected process noise bias used to ensure a non-null spread of sigma points and a positive-definite covariance. This procedure comprises the *unscented transform* used to estimate the behavior of a nonlinear function: spread sigma points based on your current uncertainty, propagate those using your transform function, and measure their spread.

To obtain the predicted observation, we again apply the unscented transform this time using the predicted states, $\mathbf{X}_{t+1|t}$, to estimate what we expect to observe from the hypothetical measurement of each state: $\mathbf{y} = h[\hat{\mathbf{x}}] \in \mathbb{R}^m$. Keep in mind that, for this study, our observation is the signal reconstruction from Equation (2.9), and the measurement itself is

Algorithm 1 Unscented Kalman Filter

- 1: Form weighted sigma points $\mathbf{X}_t = \{w_i, \mathbf{x}_i\}_{i=0}^{2n}$ around current mean \mathbf{x}_t and covariance P_t with scaling factor ζ

$$\mathbf{x}_0 = \mathbf{x}_t \quad \mathbf{x}_i = \mathbf{x}_t + [\sqrt{\zeta P_t}]_i \quad \mathbf{x}_{i+n} = \mathbf{x}_t - [\sqrt{\zeta P_t}]_i$$

- 2: Predict the new sigma points and observations

$$\mathbf{X}_{t+1|t} = f[\mathbf{X}_t] \quad \mathbf{Y}_{t+1|t} = h[\mathbf{X}_{t+1|t}]$$

- 3: Compute weighted means and covariances, e.g.

$$\bar{\mathbf{x}}_{t+1|t} = \sum_i w_i \mathbf{x}_i \quad P_{xy} = \sum_i w_i (\mathbf{x}_i - \bar{\mathbf{x}}_{t+1|t})(\mathbf{y}_i - \bar{\mathbf{y}}_{t+1|t})^T$$

- 4: Update estimate using Kalman gain K and scanner measurement \mathbf{y}_t

$$K = P_{xy}P_{yy}^{-1} \quad \mathbf{x}_{t+1} = \bar{\mathbf{x}}_{t+1|t} + K(\mathbf{y}_t - \bar{\mathbf{y}}_{t+1|t}) \quad P_{t+1} = P_{xx} - K P_{yy} K^T$$

the diffusion-weighted signal, \mathbf{s} , interpolated at the current position. From these, we obtain the predicted set of observations, $\mathbf{Y}_{t+1|t} = \{h[\hat{\mathbf{x}}_i]\} = \{\mathbf{y}_i\}$, and may calculate its weighted mean and covariance,

$$\begin{aligned} \bar{\mathbf{y}}_{t+1|t} &= \sum_i w_i \hat{\mathbf{y}}_i, \\ P_{yy} &= \sum_i w_i (\hat{\mathbf{y}}_i - \bar{\mathbf{y}}_{t+1|t}) (\hat{\mathbf{y}}_i - \bar{\mathbf{y}}_{t+1|t})^T + R, \end{aligned} \quad (2.15)$$

where R is the injected measurement noise bias again used to ensure a positive-definite covariance. The cross correlation between the estimated state and measurement may also be calculated:

$$P_{xy} = \sum_i w_i (\hat{\mathbf{x}}_i - \bar{\mathbf{x}}_{t+1|t}) (\hat{\mathbf{y}}_i - \bar{\mathbf{y}}_{t+1|t})^T. \quad (2.16)$$

As is done in the classic linear Kalman filter, the final step is to use the Kalman gain, $K = P_{xy}P_{yy}^{-1}$, to correct our prediction and provide us with the final estimated system mean and covariance,

$$\mathbf{x}_{t+1} = \bar{\mathbf{x}}_{t+1|t} + K(\mathbf{y}_t - \bar{\mathbf{y}}_{t+1|t}) \quad (2.17)$$

$$P_{t+1} = P_{xx} - K P_{yy} K^T, \quad (2.18)$$

where $\mathbf{y}_t \in \mathbb{R}^m$ is the actual signal measurement taken at this time. Algorithm 1 summarizes this algorithm for unscented Kalman filtering.

2.4 The algorithm

To summarize the proposed technique, we are using the unscented Kalman filter to estimate the local model parameters as we trace out each fiber. For each fiber, we maintain the

Algorithm 2 Main loop repeated for each fiber

- 1: **repeat**
 - 2: Form the sigma points \mathbf{X}_t around \mathbf{x}_t
 - 3: Predict the new sigma points $\mathbf{X}_{t+1|t}$ and observations $\mathbf{Y}_{t+1|t}$
 - 4: Compute weighted means and covariances, *e.g.* $\bar{\mathbf{x}}_{t+1|t}$, P_{xy}
 - 5: Update estimate $(\mathbf{x}_{t+1}, P_{t+1})$ using scanner measurement (\mathbf{y}_t)
 - 6: Proceed in most consistent direction \mathbf{m}_j
 - 7: **until** estimated model appears isotropic
-

position at which we are currently tracing it and the current estimate of its model parameters (mean and covariance). At each iteration of the algorithm, we predict the new state, which in this case is simply identity ($\mathbf{x}_{t+1|t} = \mathbf{x}_t$) as we assume the fiber does not change drastically in character from one position to the next. Our actual measurement \mathbf{y}_t in Equation (2.17) is the diffusion-weighted signal, \mathbf{s} , recorded by the scanner at this position. At subvoxel positions we interpolate directly on the diffusion-weighted images. With these, we step through the equations above to find the new estimated model parameters, \mathbf{x}_{t+1} . Last, we use path integration to move a small step in the most consistent of principal diffusion directions, and then we repeat these steps from that new location. Algorithm 2 outlines the feedback loop between filtering and tractography.

CHAPTER III

RESULTS

The supporting results of this dissertation are divided into three sections. First, we focus on the equally-weighted diffusion tensor model treating both two and three component models. Second, we switch to the Watson directional function as a model and repeat several of these experiments. Last, we extend this technique to weighted mixtures and employ a constrained filter. Also, a Python implementation of filtered tractography is made available in Slicer 3.6.

3.1 *Tensors*

We begin with synthetic experiments to validate our technique against ground truth. After constructing a set of crossing fiber fields, we perform tractography and examine the underlying orientations and branchings (Section 3.1.1). We then turn to more quantitative experiments over a broad range of angles and component weightings, and we confirm that our approach accurately recognizes crossing fibers (Section 3.1.2) and provides a superior estimate of the diffusion process (Section 3.1.3). We then demonstrate estimation of three-fiber crossings (Section 3.1.5). Lastly, we examine a real dataset to demonstrate how causal estimation is able to pick up fibers and branchings known to exist *in vivo* yet absent using an assortment of other techniques (Section 3.1.6). This section follows our work found in [103].

Following the experimental method of generating synthetic data found in [43, 135, 141], we pulled from our real data set the 300 voxels with highest fractional anisotropy (FA) and compute the average eigenvalues among these voxels: $\{1200, 100, 100\} \mu\text{m}^2/\text{msec}$ (FA=0.91). We generated synthetic MR signals according to Equation (1.1) using these eigenvalues to form an anisotropic tensor at $b=1000 \text{ s/mm}^2$ using 81 gradient directions uniformly spread on the hemisphere. We assume $s_0 = 1$ and introduce Rician noise (SNR ≈ 5 dB). For extra experiments at $b=3000$ and alternative noise levels, one can refer to an earlier conference

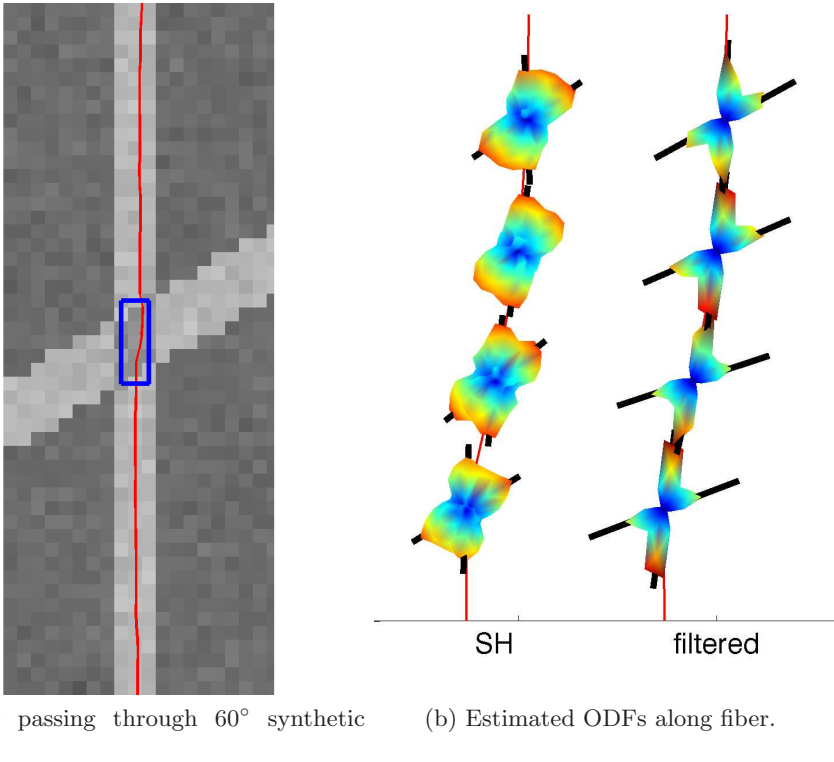


Figure 3.12: One fiber passing through an example synthetic field and the estimated ODFs within crossing region (*blue box*) using (unsharpened) spherical harmonics (SH) and the filter. The filter provides consistent angular resolution while SH modeling at those same locations sometimes misses or is off. Above and below the crossing region, the filter aligns both tensor components to fit the single-tensor signal.

version of this work [101].

In these experiments, we compare against several techniques selected to represent standard alternative models and fitting procedures. First, we include direct (least-squares) single-tensor estimation and streamline tractography [16]. Despite its limited utility in crossing and branching regions, this technique is widely used in both the clinical and neuroscience communities and provides a baseline for comparison. Second, we use the same two-tensor model from Section 2.2 but estimate the model parameters using a Levenberg-Marquardt nonlinear least-squares solver. This shows the effect of filtered estimation versus a standard alternative scheme. Such techniques depend largely on the initialization, and so we employ several variants to remove any uncertainty in initialization. For the synthetic experiments, we initialize with the ground truth. For the *in vivo* experiments, we initialize

with the single-tensor estimate [118] which we loosely refer to as “independent” and we initialize with the estimate at the previous position which we refer to as “causal”. Third, we use spherical harmonics for modeling and fiber-ODF sharpening for peak detection (order $l = 8$, regularization $L = 0.006$) [43,141]. This provides a comparison with an independently estimated, model-free representation. Note that this technique is very similar to spherical deconvolution. We will often refer to this method as “sharpened spherical harmonics”.

The unscented Kalman filter conveniently requires few parameters. Specifically, of importance are the matrices for injecting model noise Q and injecting measurement noise R (see Equation (2.14) and Equation (2.15)). Fortunately, the relative magnitude of each can be determined off-line from the data itself, and typically these are formulated as diagonal matrices (zeros off the diagonal). The injected model noise governs how much variance is allowed in the model: higher values allow more variation but, pushed too far, could lead to inaccurate estimation. We found roughly $q_{\mathbf{m}} \in [0.0015, 0.0030]$ (roughly 2-4°) and $q_{\lambda} \in [25, 100]$ to allow an appropriate amount of angular and diffusive flexibility among our synthetic and *in vivo* experiments as well as among various other patients and across other scanner protocols we have encountered. The injected measurement noise governs how much variance is expected in the measurement: higher values mean we expect more variance and hence trust our measurement less. This value depends on the level of physical noise present which varies depending on the scanner, protocol, or pre-processing, and so some experimentation may be necessary. However, in all our experiments thus far, we have found $r_s \in [0.01, 0.03]$ to quite robust.

3.1.1 Synthetic tractography

While the independent optimization techniques can be run on individually generated voxels, care must be taken in constructing reasonable scenarios to test the causal filter. For this purpose, we constructed an actual 2D field through which to navigate. In the middle is one long fiber pathway where the filter begins estimating a single tensor but then runs into a field of voxels with two crossed fibers at a fixed angle. We generated several similar fields, each at a different fixed angle and component weighting. In Figure 3.12a we show one such

field with a 60° crossing. In our experiments, fibers start from the bottom and propagate upward where they encounter the crossing region. We found that in regions with only one true fiber present (those outside the crossing here), the second component consistently aligned with the first.

In Figure 3.12b we take a closer look at several points along this single fiber as it passes through the crossing region. We examine the reconstructed ODFs produced by the filter as well as those produced by spherical harmonic modeling at those same positions. As reported in [43, 135], spherical harmonics at $b = 1000$ begin to not detect the second component at around 50° - 60° , but instead report a single angle as seen in one of the middle samples in Figure 3.12b. As reported in [135, 139, 155], a close examination of the reported axes shows this bias toward a single averaged axis. In contrast, the filtered results are consistent and accurate. One can note a slight deflection upon entry of the crossing region as the filter attempts to maintain smooth estimates. The deflection is lessened upon exit since the single component allows for the most stable model fit.

3.1.2 Angular resolution

Having verified the underlying behavior, we then began a more comprehensive evaluation and quantified the estimated angle within the crossing regions. Synthetic crossing fields were constructed with a range of crossing angles and weighting combinations. In Figure 3.13a each row is a different weighting: top 50-50, middle 60-40, bottom 70-30. Each graph then plots the angular error as a function of crossing angle, from 15° to 90° . Within the crossing regions, we compared the performance among direct single-tensor estimation, sharpened spherical harmonics, a nonlinear solver (Levenberg-Marquardt), and the proposed filter. By varying the size of the crossing regions in Figure 3.12a or the number of fibers run, we ensured that each technique performed estimation on at least 500 voxels to produce consistent trendlines across this wide range of angles.

Figure 3.13a shows the estimated separating angle reported using spherical harmonics (*red*), the nonlinear solver (*blue*), and the proposed filter (*black*). Over each technique's series of estimations, the trendlines indicate the mean error while the bars indicate one

standard deviation. Consistent with the synthetic results reported in [41, 43], spherical harmonics are generally unable to detect and resolve angles below 50° for $b=1000$ or below 40° for $b=3000$. With a perfect initialization, the Levenberg–Marquardt solver is closer to the solution but shows significant variance from the noise. In contrast, the filtered approach statistically estimates the true underlying signal and so is capable of resolving angles down to the range of $20\text{--}30^\circ$ with 5° error in the equally weighted field (*50-50*) (*top row*) with performance degrading little in the $60\text{--}40$ field (*middle*). In the $70\text{--}30$ field (*bottom*), the trendlines begin to show an asymptotic limit to performance, yet the filter is the only method capable of reasonable estimates at large angles. See [101] for additional experiments at both $b=1000$ and $b=3000$. From these trendlines, one can conclude that the filtered approach provides accurate and consistent angular resolution at crossing angles far below independent estimation.

3.1.3 Estimated quantities

While angular resolution is important in accurately resolving paths, the underlying estimated quantities are important in the analysis of these pathways. We focus on three scenarios: a single fiber (no crossing), a 45° crossing, and an orthogonal 90° crossing. In each scenario we hold constant the primary eigenvalue and adjust the minor eigenvalues to produce fields with a range of diffusion properties. Further, we adjust the crossing weights as in the earlier experiments. We compare among the three techniques estimating diffusion quantities: direct single-tensor estimation (*green*), the two-tensor model with the nonlinear solver (Levenberg–Marquardt initialized with ground truth) (*blue*), and the two-tensor model with the proposed filter (*black*). And finally we judge these techniques using the error in estimated fractional anisotropy (FA), one of the most common proxy measures for diffusion.

The fields with a single fiber (no crossing) serve as another baseline. Figure 3.13b shows that both direct estimation and the filter provide tight estimates of the true FA. Note the increased variance incurred in the nonlinear solver due to noise. In Figure 3.13c, single-tensor estimation begins to show a bias. Levenberg–Marquardt begins to deteriorate

slightly, but the filter continues to provide accurate and consistent estimates. Lastly, in Figure 3.13d, single-tensor estimation provides erroneous estimates while only the multi-component techniques are able to maintain accuracy. Note again how the filter provides tight estimates.

3.1.4 Volume fractions

In the current implementation, we have chosen a model without weights (Equation (2.3)). To examine this assumption, we included experiments over weighted fields to see the effect on estimation. Each row of Figure 3.13 shows a different weighting combination: equal in the top row to most asymmetric in the bottom row.

Despite the equally-weighted assumption, Figure 3.13a shows that the filter is capable of correctly resolving angles in the range of 60-40 and only the most orthogonal angles at 70-30. In all of these runs, the filter maintained tracing of the dominant fiber, drifting little in the most asymmetric cases. At 80-20 no technique was able to reliably detect the minor component.

While the filter had trouble picking up the minor component in the more asymmetric cases, Figure 3.13b-3.13d shows that it maintained accurate estimates of the diffusion processes, perhaps the most important consideration. In these regions where the model does not explicitly fit the data, we found that the filter compensates by adjusting the eigenvalues. For example, changes in the eigenvalues could be interpreted as weights: $e^{-b\mathbf{u}_i^T D \mathbf{u}_i} = e^{-b\mathbf{u}_i^T (D_a + D_b) \mathbf{u}_i} = e^{-b\mathbf{u}_i^T D_a \mathbf{u}_i} e^{-b\mathbf{u}_i^T D_b \mathbf{u}_i} = w e^{-b\mathbf{u}_i^T D_b \mathbf{u}_i}$. In each of the unequally weighted crossings, the filter increases the eigenvalues of the primary component and decreases those of the minor component in order to fit the signal with much the same effect as increasing or decreasing weights. Since all techniques appear to deteriorate beyond the 70-30 weighting, it appears that components of less than 30% contribution will not be reliably detected despite incorporating weights.

The unscented Kalman filter itself places no constraint on the state space except what is statistically likely given the current estimate: all values in the state vector are free to take any value in \mathbb{R} . In our current implementation, we restricted \mathbf{m} to \mathbb{S}^2 and $\lambda_1, \lambda_2 > 0$.

However, this is an ad hoc solution and we have experimented with applying causal filters capable of estimating under model constraints, *e.g.* positive eigenvalues, convex weights [102].

3.1.5 Three-fiber crossings

Resolving three-fiber crossings has proven difficult for many techniques, especially at the lower b -values typically used in clinical scans. For example, [146] found the general multi-tensor model to be unstable for three or more components using data at $b=1077$ with 126 gradients. [25] only reported results for up to two-tensors ($b=700$, 30 gradients). In simulation, [22] found that b -values at upwards of 3000-4000 s/mm² were required for detecting more than two fibers and none were found *in vivo* ($b=1000$, 60 gradients). Further, many studies specifically use at most two orientations [2, 84, 118]. However, spherical shell techniques have had some success in resolving three-fiber crossings. [141] reported such crossings using spherical deconvolution ($b=2971$, 60 gradients). Most recently, [135] demonstrated tensor decomposition as a promising technique for resolving such configurations ($b=1000$, 60 gradients).

Following the synthetic experimental setup of [135], we constructed an additional set of synthetic fields this time with three equally-weighted Gaussian components. Similar to the synthetic fields shown in Figure 3.12a, one fiber is angled up and is the intended orientation to track through the region, but here the other two orientations were set so that the endpoints of the three principal axes formed an equilateral triangle with any two separated by the specified angle. With this setup, Figure 3.14 shows that the filtered approach provides an accurate estimate that reaches to roughly 45° compared to 60-65° for spherical harmonics. A significant bias is apparent at more acute angles using either technique.

3.1.6 *In vivo* tractography

We next test our approach on a real human brain scan acquired on a 3-Tesla GE system using an echo planar imaging (EPI) diffusion weighted image sequence. A double echo option was used to reduce eddy-current related distortions. To reduce impact of EPI spatial

distortion, an eight channel coil was used to perform parallel imaging using Array Spatial Sensitivity Encoding Techniques (GE) with a SENSE-factor (speed-up) of 2. Acquisitions have 51 gradient directions with $b = 900$ and eight baseline scans with $b = 0$. The original GE sequence was modified to increase spatial resolution, and to further minimize image artifacts. The following scan parameters were used: TR 17000 ms, TE 78 ms, FOV 24 cm, 144x144 encoding steps, 1.7 mm slice thickness. All scans had 85 axial slices parallel to the AC-PC line covering the whole brain. In addition, $b=0$ field inhomogeneity maps were collected and calculated.

We first focus on fibers originating in the corpus callosum. Specifically, we seek to trace out the lateral transcallosal fibers that run through the corpus callosum out to the lateral gyri. It is known that single-tensor streamline tractography only traces out the dominant pathways forming the U-shaped callosal radiation (Figure 2.10, 3.15a, and 3.16a). Several studies document this phenomena, among them the works of Descoteaux, Schultz, et al. [43, 135] have side-by-side comparisons. These fibers have been reported in using diffusion spectrum imaging [64], probabilistic tractography [8, 43, 78], and more recently with tensor decomposition [135].

We start with two basic experiments: first examining the tracts surrounding a single coronal slice and second looking at all tracts passing through the corpus callosum. We seed each algorithm multiple times in voxels at the intersection of the mid-sagittal plane and the corpus callosum. We terminate fibers when the generalized fractional anisotropy of the estimated signal (std/rms) fell below 0.1. To explore branchings found using the proposed technique, we consider a component to be branching if it was separated from the primary component by less than 40° with $FA \geq 0.15$. Similarly, with sharpened spherical harmonics, we consider it a branch if we find additional maxima over the same range. Unless otherwise stated, in all experiments we follow the primary fiber from the seeding and its branches, *i.e.* one level of branching. We do not go on to follow the branches on those secondary fibers. While such heuristics are somewhat arbitrary, we found little qualitative difference in adjusting these thresholds.

To demonstrate the flexibility of the proposed filtering strategy with respect to model

choice, we use both the two-tensor fiber model (Equation (2.3)) and the three-tensor fiber model (Equation (2.4)). While this introduced differences in the quantity of branchings detected, we found that using either model resulted in generally the same pathways. This suggests that the filtering itself accounted for most of the differences compared to the other techniques, more so than the choice of two or three components in the fiber model. Further, it is important to note that despite the more complicated multi-fiber models, the filter provides stable and consistent estimates of the appropriate number of compartments. For example, when tracing using the two-tensor fiber through a one-tensor region, the filter overlaps both tensors to fit the signal (above and below the crossing region in Figure 3.12a).

For the first experiment, Figure 3.15 shows tracts originating from within a few voxels intersecting a particular coronal slice. As a reference, we use a coronal slice showing the intensity of fractional anisotropy (FA) placed a few voxels behind the seeded coronal position. Keeping in mind that these fibers are intersecting or are in front of the image plane, this roughly shows how the fibers navigate the areas of high anisotropy (bright regions). Comparable to the results in [43, 135], Figure 3.15b shows that sharpened spherical harmonics only pick up a few fibers intersecting the U-shaped callosal radiata. In contrast, our proposed method traces out many pathways consistent with the apparent anatomy using either the two-fiber or three-fiber model. To emphasize transcallosal tracts, we color as blue those fibers exiting a corridor of ± 22 mm around the mid-sagittal plane. To explore the maximum connectivity found using each approach, this is the one experiment where we followed secondary branches, *i.e.* primary fibers, their branches, and finally branches off those fibers. Figure 3.16 shows a view of the whole brain to see the overall difference between the different methods.

We next combined the filtered tracings from the corpus callosum with those from the internal capsule to demonstrate practically how the filter is able to push through areas of crossing. Figure 3.17 shows successive snapshots as two-tensor filtered tracings from the corpus callosum (*red*) infiltrate those originating in the internal capsule (*yellow*). Since other methods were unable to reconstruct such dense penetration, it is our hope that this method of multi-tensor tractography will provide rich information in connectivity studies.

Figure 3.18 takes a closer look at one area where these fiber pathways merge and shows fragments from the fibers traversing through this region using the three-tensor model.

In the experiments thus far, the decision to branch is somewhat ad hoc. An alternative approach to avoid such thresholds is to perform full-brain tractography following only one path and then select fibers using masks. Along these lines we seeded every voxel with $FA \geq 0.15$ using each technique discussed so far. In addition, we included filtered single-tensor tractography to contrast to the baseline single-tensor streamline.

We select out three well-studied pathways. Figure 3.19 shows the first pathway, a portion of the superior longitudinal fasciculus as it crosses the lateral pathways exposed in earlier figures. Only two techniques were able to produce this portion of the tract: the causal variant of Levenberg-Marquardt (initializes each step with previous solution) and filtered two-tensor tractography. Both share the same general shape, but the filtered version appears to show a superior reconstruction, especially where the endpoints insert. Spherical harmonics were unable to traverse through the lateral crossings here likely due to ambiguous peaks along this corridor, and the single-tensor models are inherently incapable of modeling the crossing.

Figure 3.20 shows the second pathway, the cingulum bundle as it passes through several gates (*yellow*). Each technique incurs false-positive fibers at the ends of the corpus—the genu (anterior) and splenium (posterior)—where partial voluming often leads to fibers straying onto the corpus callosum. While all techniques have difficulty making the posterior bend, they begin to differ in their reconstructions of the main body. Going from streamline single-tensor to filtered single-tensor, we see a fuller reconstruction. Levenberg-Marquardt shows many false positives as it easily finds incorrect minima. Sharpened spherical harmonics provide an accurate although sparse reconstruction. Filtered two-tensor provides a full reconstruction although it produces many false positives.

Last, Figure 3.21 shows tracing of the interior occipital-fronto fasciculus as it spreads and inserts into the occipital and temporal lobes. Streamline single tractography reconstructs the central pathway. Only the filtered techniques provide consistently deeper penetration into the gray matter while retaining coherent paths. Further, only the filtered version of

the two-tensor model reconstructs the known minor insertions into the temporal lobe. This is even more pronounced in the views from above in Figure 3.22.

3.2 Watson directional functions

We now treat the evaluation of the Watson directional function separately. Since this model is an approximation of the tensor diffusion model, we begin with experiments examining reconstruction error as well as those measuring angular error before moving quickly to *in vivo* experiments. This section follows our work in [98].

Throughout these experiments, we draw comparison to three alternative techniques. First, we use the same two-Watson model from Section 2.2 with a variant of matching pursuit for brute force, dictionary-based optimization [104]. In our implementation, we construct a finite dictionary of two-Watson signals at a range of various k -values, essentially discretizing the search space across orientations and k -values. Given a new measured signal, the signal from the dictionary with highest inner product provides an estimate of orientation and concentration. While our signal is produced at 81 gradient directions, we use 341 directions to construct the dictionary, thus any error is due to the method's sensitivity to noise and discretization. Note that by using 341 orientation directions there is roughly an 8° angular difference between offset orientations, hence we see that the angular error is often at most 8° . This approach highlights the effect of using the same model but changing the optimization technique to one that treats each voxel independently. Second, as in the tensor experiments above, we use spherical harmonics for modeling [141] and fiber-ODF sharpening for peak detection as described in [43] (order $l = 8$, regularization $L = 0.006$). This provides a comparison with an independently estimated, model-free representation. Last, when performing tractography on real data, we again include single-tensor streamline tractography as a baseline.

For the Watson model, we found that values on the order of $q_m = 0.001$ (roughly 2°), $q_\lambda = 10$, and $r_s = 0.02$ were quite robust for the appropriate diagonal entries of Q and R (see Equation (2.14) and Equation (2.15)). Off-diagonal entries were left at zero.

3.2.1 Signal reconstruction and angular resolution

In the first experiment, we look at signal reconstruction error. We calculate the mean squared error of the reconstructed signal, \mathbf{s} , against the ground truth signal, $\hat{\mathbf{s}}$ (pure, no noise): $\|\mathbf{s} - \hat{\mathbf{s}}\|^2 / \|\hat{\mathbf{s}}\|^2$. In essence, this is exactly what the filter is trying to minimize: the error between the reconstructed signal and the measured signal. Figure 3.23 shows the results of using the proposed filter, matching pursuit, and spherical harmonics. Over each technique's series of estimations, the trendlines indicate the mean error while the bars indicate one standard deviation. Spherical harmonics (*red*) appear to produce a smooth fit to the given noisy data, while matching pursuit (*blue*) shows the effect of discretization and sensitivity to noise. The two raised areas are a result of the dictionary being constructed with an 8° minimum separation between any pair of orientations. This experiment demonstrates that the proposed filter (*black*) accurately and reliably estimates the true underlying signal.

In the second experiment, we looked at the error in angular resolution by comparing the filtered approach to matching pursuit and sharpened spherical harmonics. Figure 3.24a and Figure 3.24b show the sensitivity of matching pursuit. Consistent with the results reported in [41,43], spherical harmonics are generally unable to detect and resolve angles below 50° for $b=1000$ or below 40° for $b=3000$. Figure 3.24c and Figure 3.24d confirm this, respectively. This experiment demonstrates that for $b=1000$, the filtered approach consistently resolves angles down to $20-30^\circ$ with 5° error compared to independent optimization which fails to reliably resolve below 60° with as much as 15° error. For $b=3000$, the filtered approach consistently resolves down to $20-30^\circ$ with $2-3^\circ$ error compared to independent optimization which cannot resolve below 50° with 5° error.

3.2.2 *In vivo* tractography

As in Section 3.2.2, we first focused on fibers originating in the corpus callosum. We proceed with two basic experiments: first examining the tracts surrounding a single coronal slice and second looking at all tracts passing through the corpus callosum. We seed each algorithm multiple times in voxels at the intersection of the mid-sagittal plane and the

corpus callosum. To explore branchings found using the proposed technique, we considered a component to be branching if it was separated from the primary component by less than 40° with $k \geq 0.6$. Similarly, with sharpened spherical harmonics, we considered it a branch if we found additional maxima over the same range. We terminated fibers when the general fractional anisotropy of the estimated signal (std/rms) fell below 0.1. While such heuristics are somewhat arbitrary, we found little qualitative difference in adjusting these values.

To demonstrate the flexibility of the proposed filtering strategy with respect to model choice, we use both the two-Watson fiber model (Equation (2.9)) and the three-Watson fiber model (Equation (2.10)). While this introduced differences in the quantity of branchings detected, we found that using either model resulted in generally finding the same pathways.

For the first experiment, Figure 3.25 shows tracts originating from within a few voxels intersecting a particular coronal slice. For a reference backdrop, we use a coronal slice showing the intensity of fractional anisotropy (FA) placed a few voxels behind the seeded coronal position. Keeping in mind that these fibers are intersecting or are in front of the image plane, this roughly shows how the fibers navigate the areas of high anisotropy (bright regions). Our proposed method traces out many pathways consistent with the apparent anatomy using either the two-fiber or three-fiber model. To emphasize transcallosal tracts, we color as blue those fibers exiting a corridor of ± 22 mm around the mid-sagittal plane. Figure 3.26 provides a closer inspection of Figure 3.25c and Figure 3.25d where, to emphasize the underlying anatomy influencing the fibers, we use as a backdrop the actual coronal slice passing through the voxels used to seed this run. Such results are obtained in minutes in either our MATLAB or Python implementations. At each step, the cost of reconstructing the signal for few sigma points approaches the cost of a few iterations of weighted least-squares estimation of a single tensor.

For the second experiment, Figure 3.31 shows a view of the whole brain to see the overall difference between the different methods. Here again we emphasize with blue the transcallosal fibers found using the proposed filter. Comparing Figure 3.31c and Figure 3.31d we see several regions that appear to have different fiber density using the two models. This suggests that incorporating model selection into filtered approaches may have a significant

effect. To show the various pathways infiltrating the gyri, Figure 3.27 provides a closeup of the frontal lobe from above (without blue emphasis).

Next we examined fibers passing through the internal capsule to trace out the pathways reaching up into the primary motor cortex at the top of the brain as well as down into the hippocampal regions near the brain stem. Figure 3.28 shows frontal views for each technique with seeding near the cerebral peduncles (*blue*). Figure 3.30 shows this same result from a side view where we can see that the filtered approach picks up the corticospinal pathways. Notice that the two-Watson model picks up the temporopontine and parietopontine tracts and the three-Watson model further reveals the occipitopontine pathways, another indication that the chosen fiber model often affects the results. As reported elsewhere [22, 125], single-tensor tractography follows the dominant corticospinal tract to the primary motor cortex. The same pathways were also found with spherical harmonics. Figure 3.29 shows a view from above where we use a transverse FA image slice near the top of the brain as a backdrop so we can focus on the fiber endpoints. From this we can see how each method infiltrates the sulci grooves, and specifically we see that the filtered method is able to infiltrate sulci more lateral compared to single-tensor tractography.

Note that in the region of intersection between the transcallosal fibers, the corticospinal, and the superior longitudinal fasciculus, the partial voluming of each of these pathways leads the filter to report several end-to-end connections that are not necessarily present, e.g. fibers originating in the left internal capsule do not pass through this region, through the corpus callosum and then insert into the right motor cortex. Many of the lateral extensions are callosal fibers that are picked up while passing through this juncture. It is our hope that such connections may be avoided with the introduction of weighted mixtures, alternative filter formulations, or different heuristic choices in the algorithm.

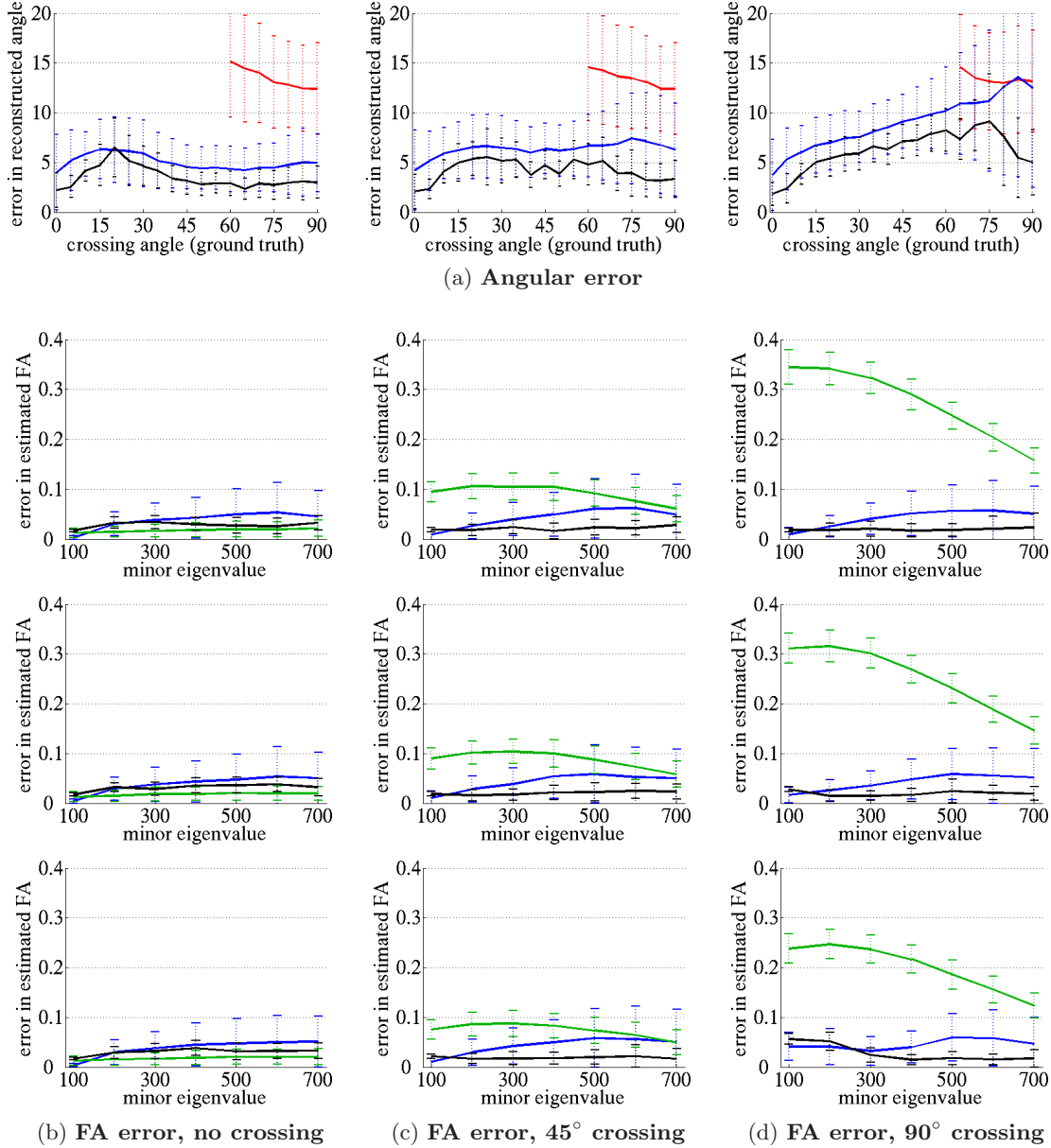


Figure 3.13: The error in estimated crossing angle (a) and estimated fractional anisotropy (b)-(d) at various volume fractions: 50%-50% (top row), 60%-40% (middle row), 70%-30% (bottom row). Where appropriate, we compare among single-tensor least-squares (green), sharpened spherical harmonics (red), two-tensor Levenberg-Marquardt (blue), and the proposed filtered two-tensor (black). Through all examples, the filtered technique provides the most consistent and accurate results.

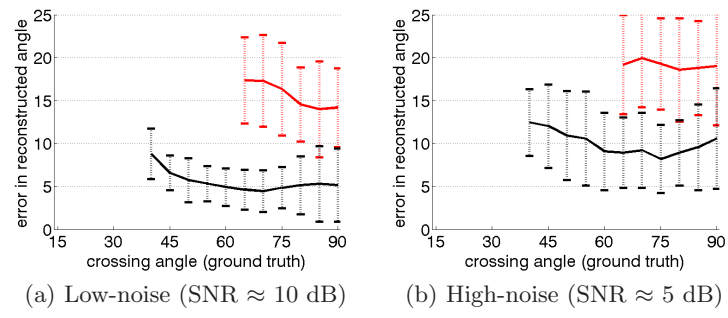


Figure 3.14: The filtered approach (*black*) is able to resolve three-fiber crossings with improved accuracy and at sharper angles compared to using sharpened spherical harmonics (*red*). Both low-noise and high-noise experiments are shown.

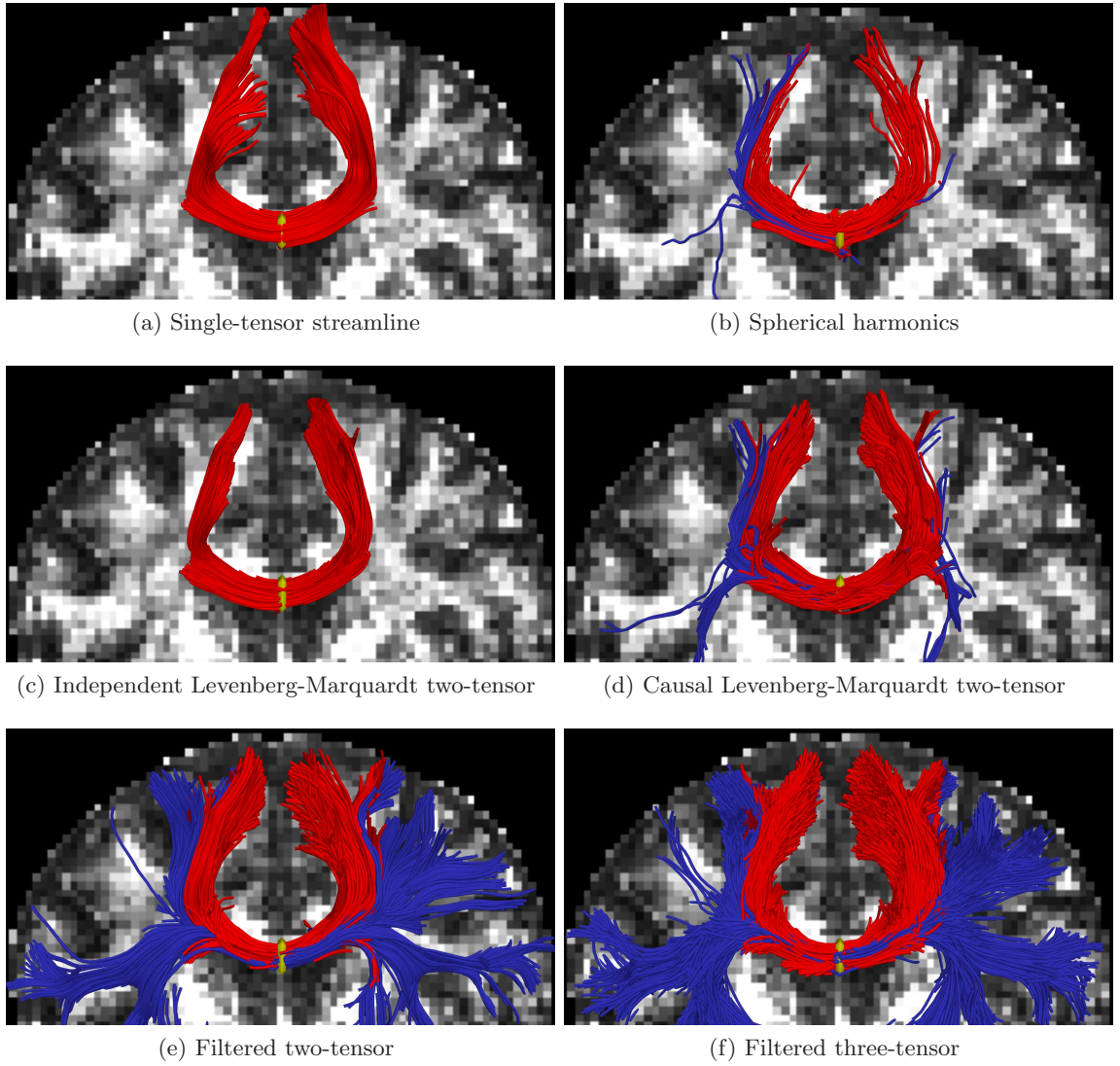


Figure 3.15: Tractography using various methods, seeded at the center of the corpus callosum. Single-tensor reconstructs only the dominate callosal radiata (a). Spherical harmonics pick up some of the lateral branches (b). Initializing a Levenberg-Marquardt solver with an independent single tensor estimate finds only the radiata (c), while initializing instead with its previous estimate (d) finds little more than spherical harmonics. Only filtered tractography picks up the lateral paths consistent with the underlying anatomy. Fibers exiting ± 22 mm around the mid-sagittal plane are indicated in *blue*. Seed region indicated in *yellow*.

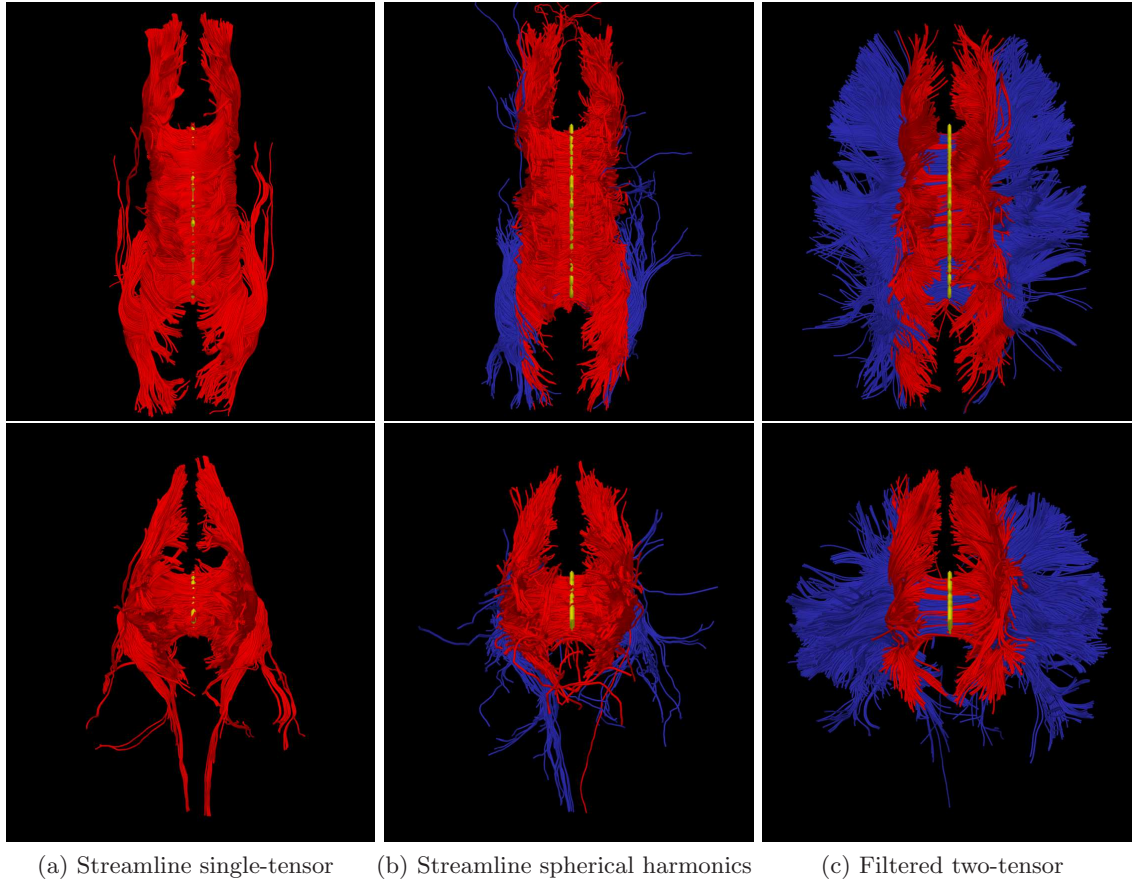


Figure 3.16: Tracing fibers originating from the center of the entire corpus callosum with views from above (*top rows*) and front-to-back (*bottom rows*). The proposed filtered tractography is able to find many of the lateral projections (*blue*) while single-tensor is unable to find any and few are found with sharpened spherical harmonics. Seed region indicated in *yellow*.



Figure 3.17: Successive snapshots of filtered two-tensor tracing from both the corpus callosum (*red*) and internal capsule (*yellow*), viewed from right hemisphere. Here we see the lateral pathways from the corpus cross the motor tracts from the internal capsule.

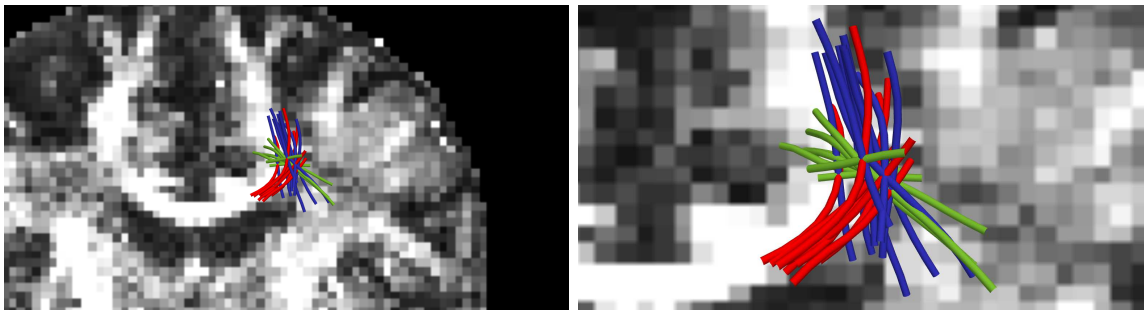
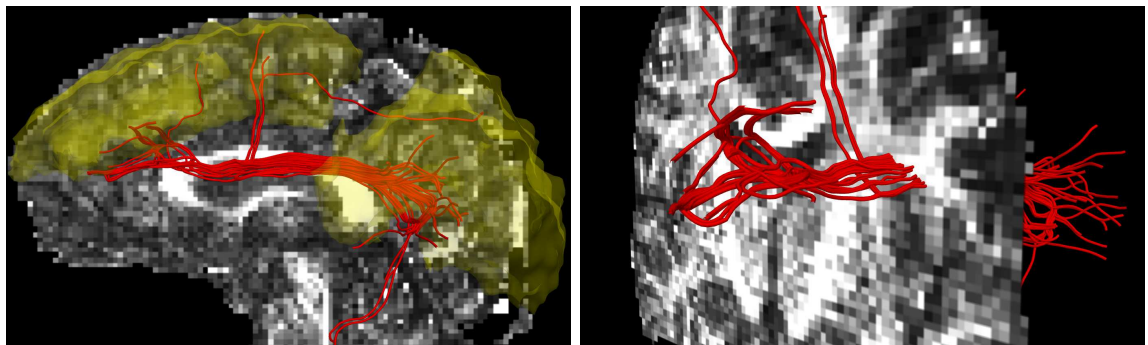
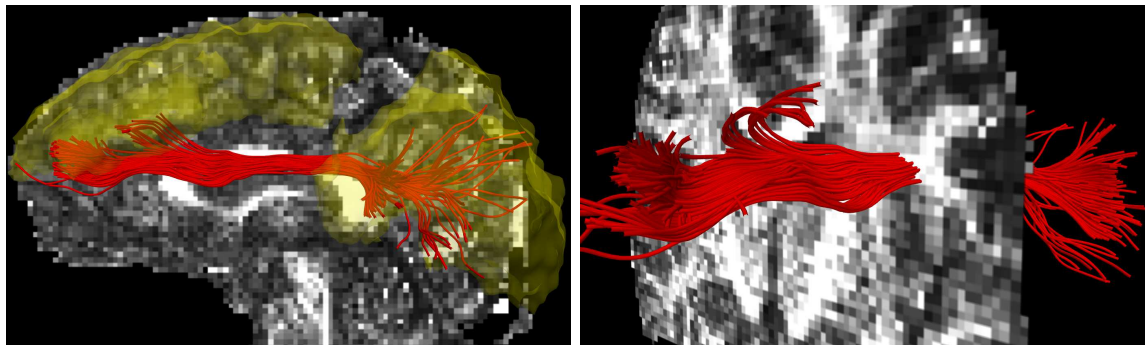


Figure 3.18: The three-tensor filtered approach is able to trace through this intersection of the corticospinal tract (*blue*), corpus callosum (*red*), and superior longitudinal fasciculus (*green*).



(a) Levenberg-Marquardt (causal) two-tensor



(b) Filtered two-tensor

Figure 3.19: A portion of the superior longitudinal fasciculus as it crosses a section of the lateral pathways emanating from the corpus callosum. These fibers were extracted using two regions of interest (*yellow*). While LM reconstructs several of these fibers, filtered estimation produces a more consistent bundle with deeper, uniform penetration into the frontal and occipital lobes. No such fibers were found using the comparison methods.

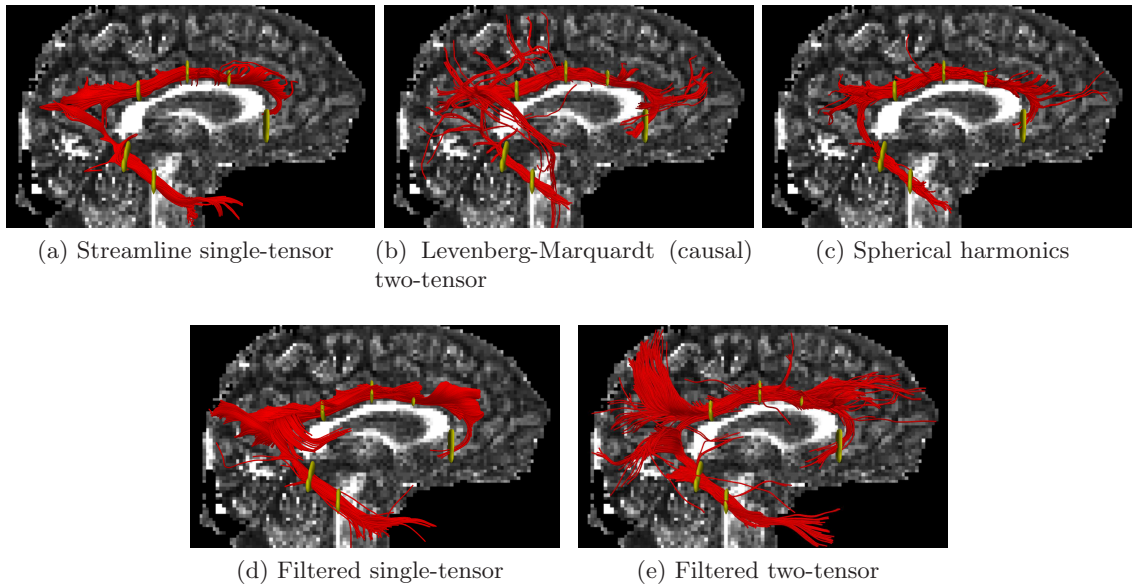


Figure 3.20: Tracing of the right cingulum bundle using various methods. From full-brain seeding, fibers were selected that passed through any two gates (*yellow*). While all methods here produce some false-positives (*e.g.* partial voluming onto the splenium, genu, or tapetum), the filtered methods appear to produce the fullest cingulum reconstructions.

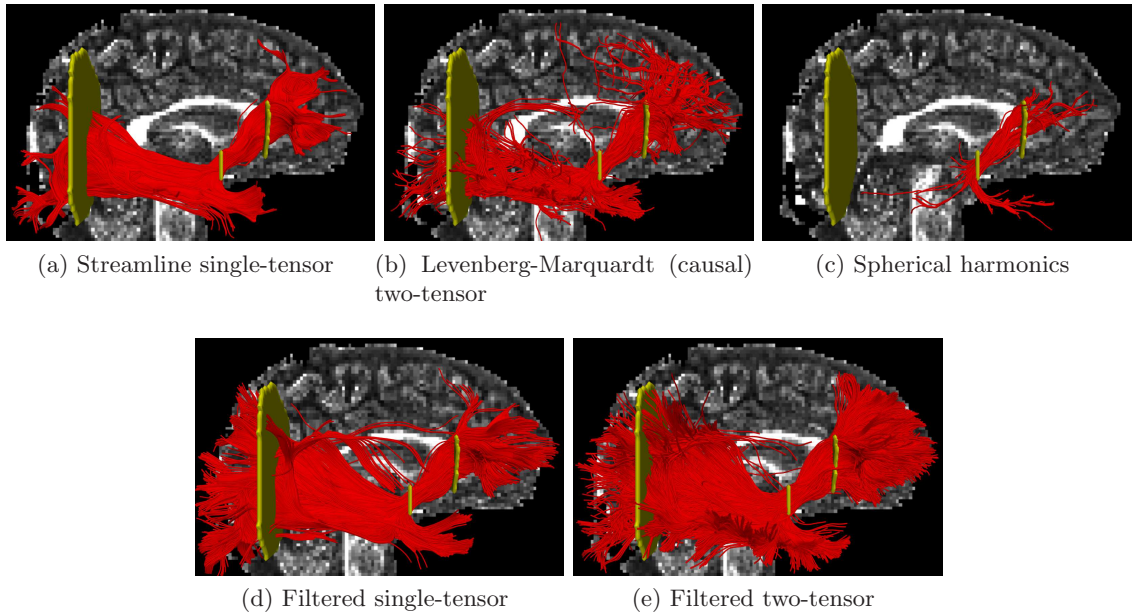


Figure 3.21: Tracing of the right inferior fronto-occipital fasciculus using various methods. From full-brain seeding, fibers were selected that passed through any two gates (*yellow*). Spherical harmonics and Levenberg-Marquardt show sparse and irregular connectivity. Filtered single- and two-tensor results appear to have deeper and more uniform penetration into the occipital lobe.

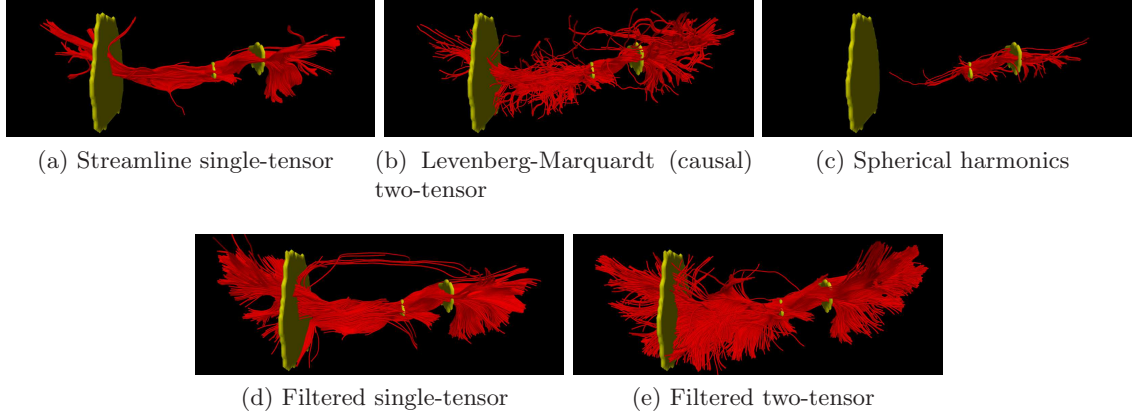


Figure 3.22: A view of the previous figure from above. Note the consistent deeper penetration of the filtered techniques. The two-tensor method infiltrates many minor pathways into the temporal lobe.

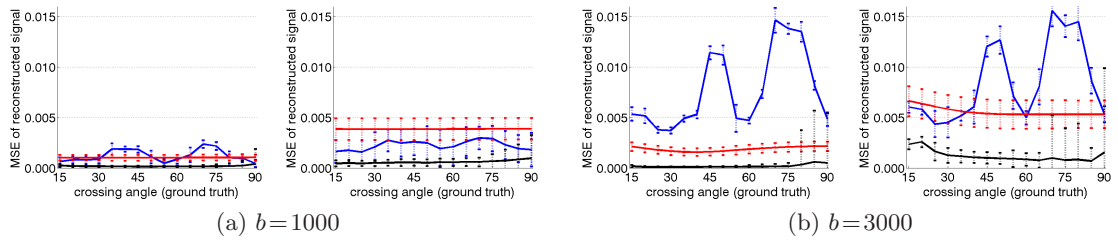


Figure 3.23: Mean squared error (MSE) between reconstructed signal and ground truth signal at various crossing angles (*low-noise on left, high-noise on right*). Notice how the increased noise has little effect on the filter (*black*) compared to using matching pursuit (*blue*) or sharpened spherical harmonics (*red*).

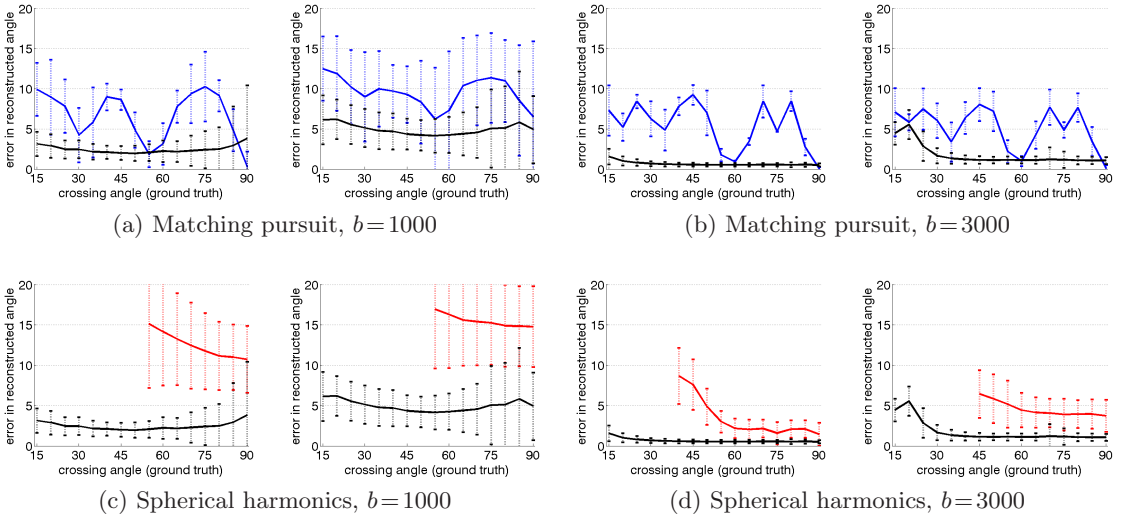


Figure 3.24: Average angle error at various crossing angles comparing all three techniques: matching pursuit (blue), sharpened spherical harmonics (red), and the proposed filter (black). The filter provides stable and consistent estimation compared to either alternative technique. Each subfigure shows both the low-noise and high-noise experiments (left, right).

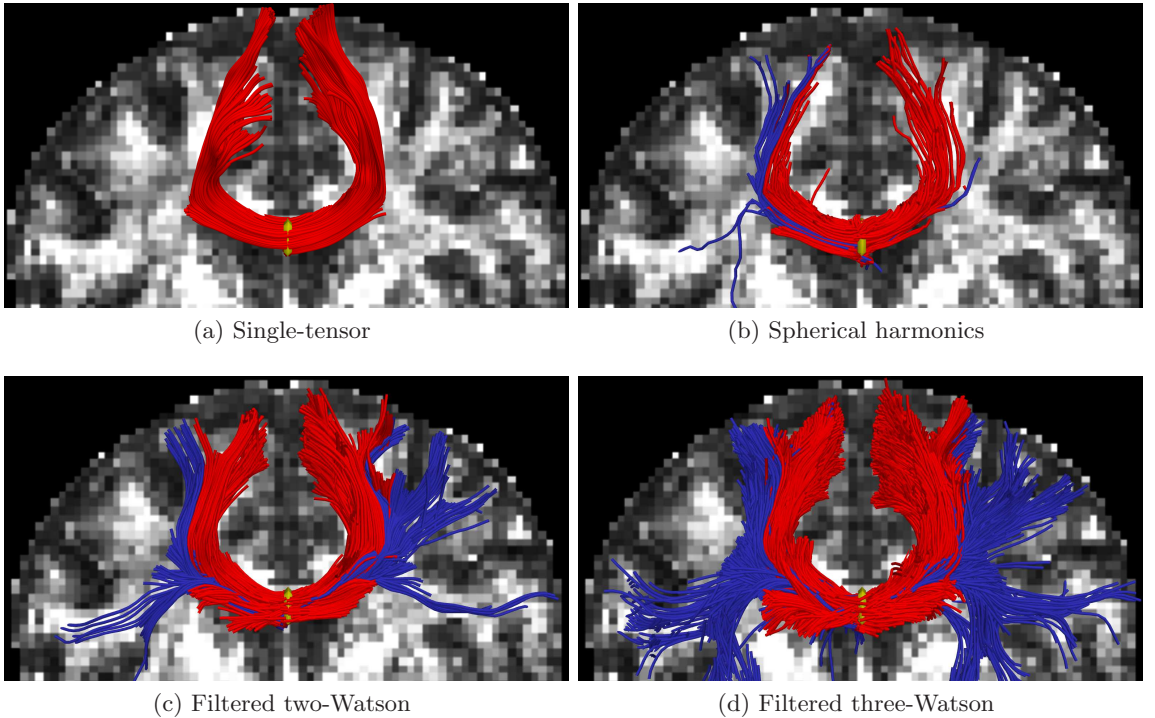
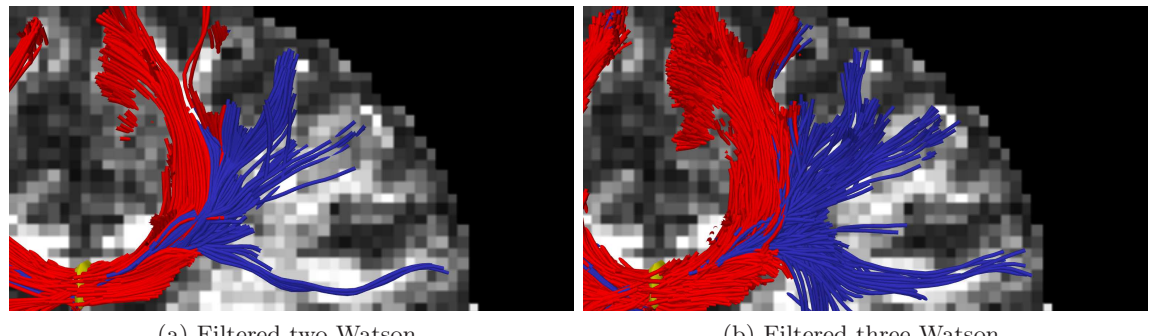


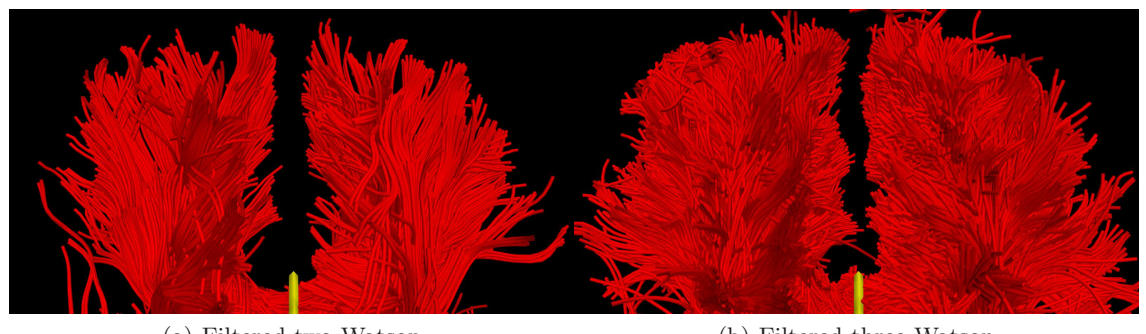
Figure 3.25: Filtered tractography picks up many fiber paths consistent with the underlying structures. Both single-tensor streamline and sharpened spherical harmonics are unable to find the majority of these pathways. Fibers existing ± 22 mm around the mid-sagittal plane are indicated in blue. Seed region indicated in yellow.



(a) Filtered two-Watson

(b) Filtered three-Watson

Figure 3.26: Closeup of upper right in Figure 3.25c and Figure 3.25d.



(a) Filtered two-Watson

(b) Filtered three-Watson

Figure 3.27: Closeup of frontal fibers in Figure 3.31c and Figure 3.31d viewed from above.

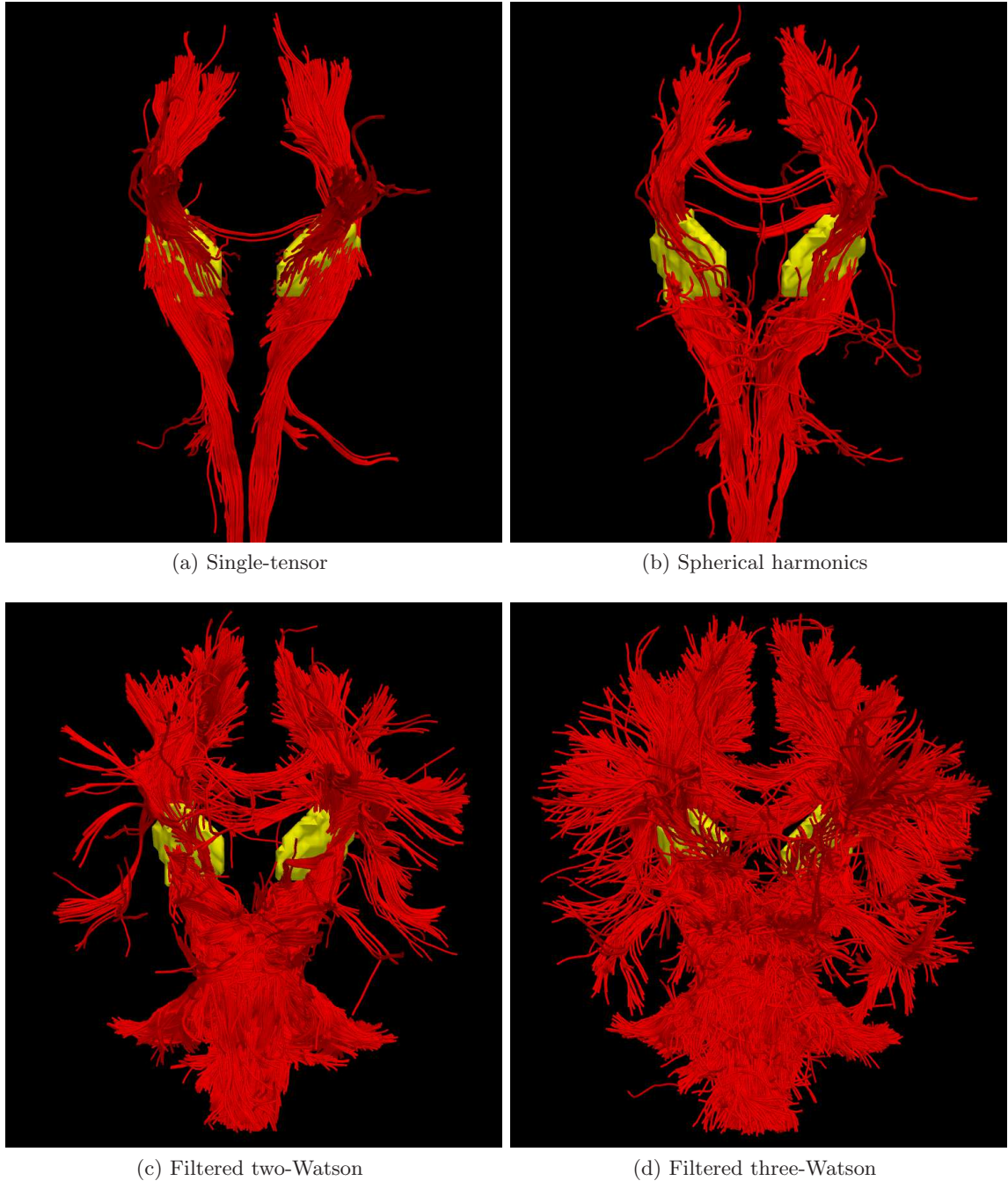


Figure 3.28: Frontal view with seeding in the internal capsule (*blue*). While both single-tensor and spherical harmonics tend to follow the dominant corticospinal tract to the primary motor cortex, the filtered approach follows many more pathways. Seed region indicated in yellow.

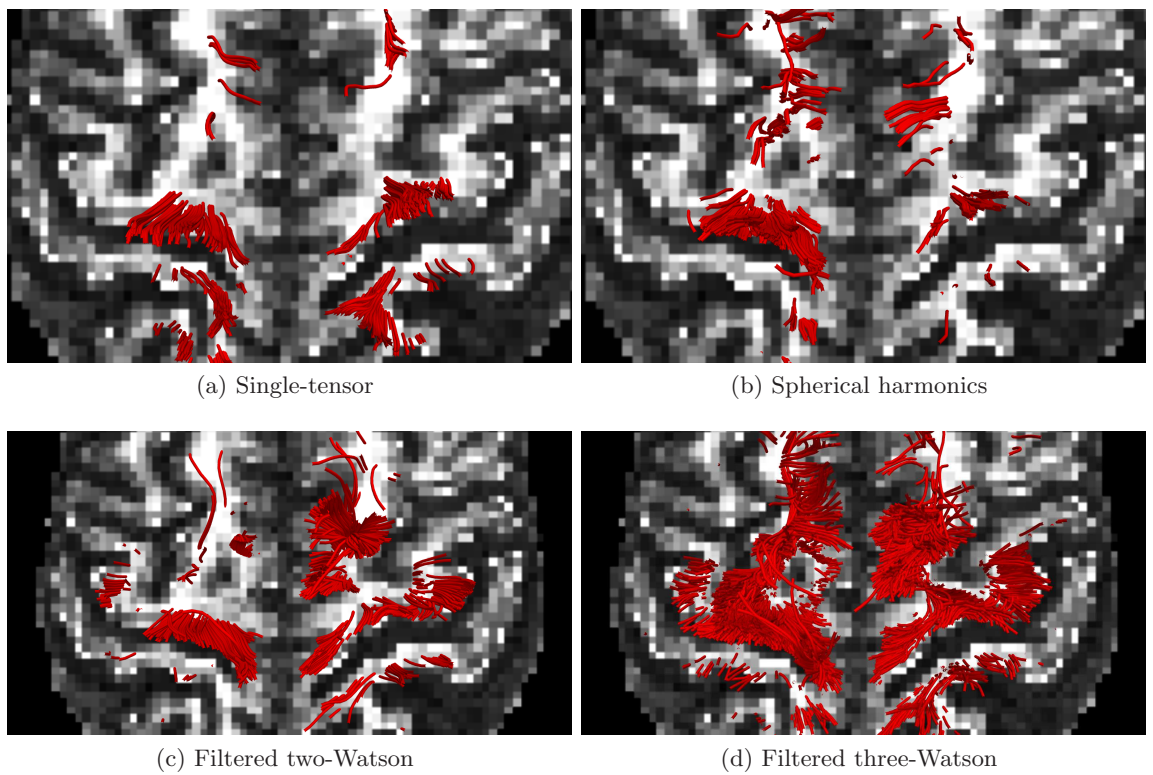


Figure 3.29: View from above showing cortical insertion points for each method. FA backdrop is taken near the top of the brain. The filtered approach shows more lateral insertions compared to single-tensor and spherical harmonic tracts.

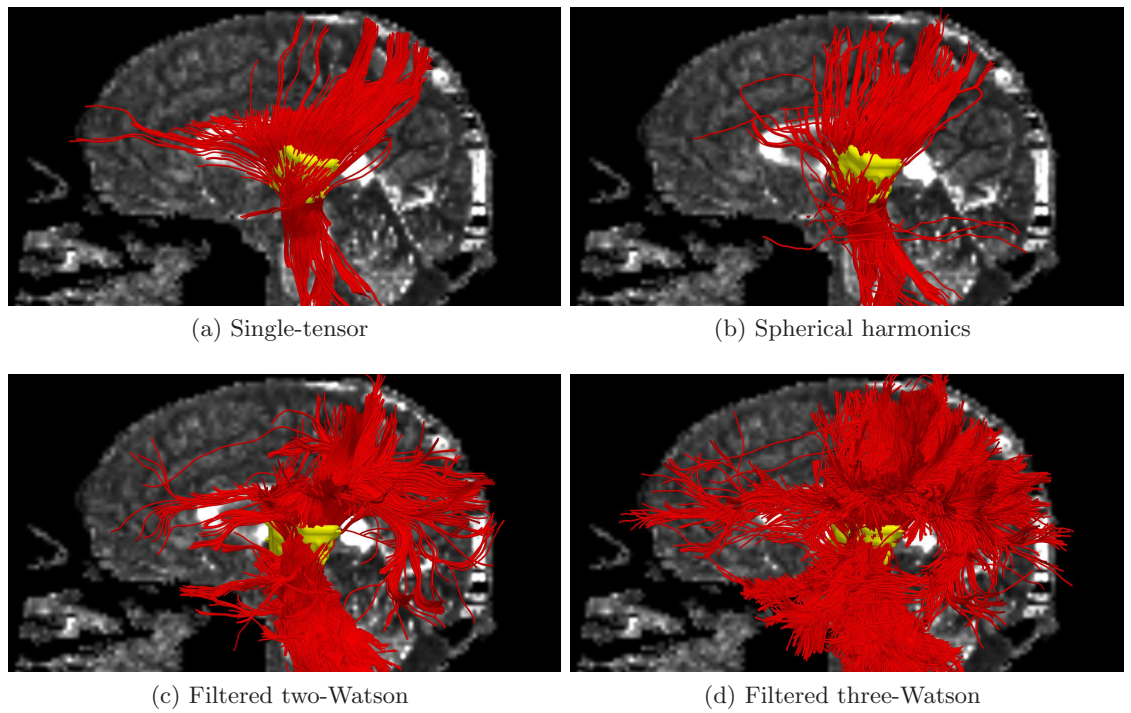
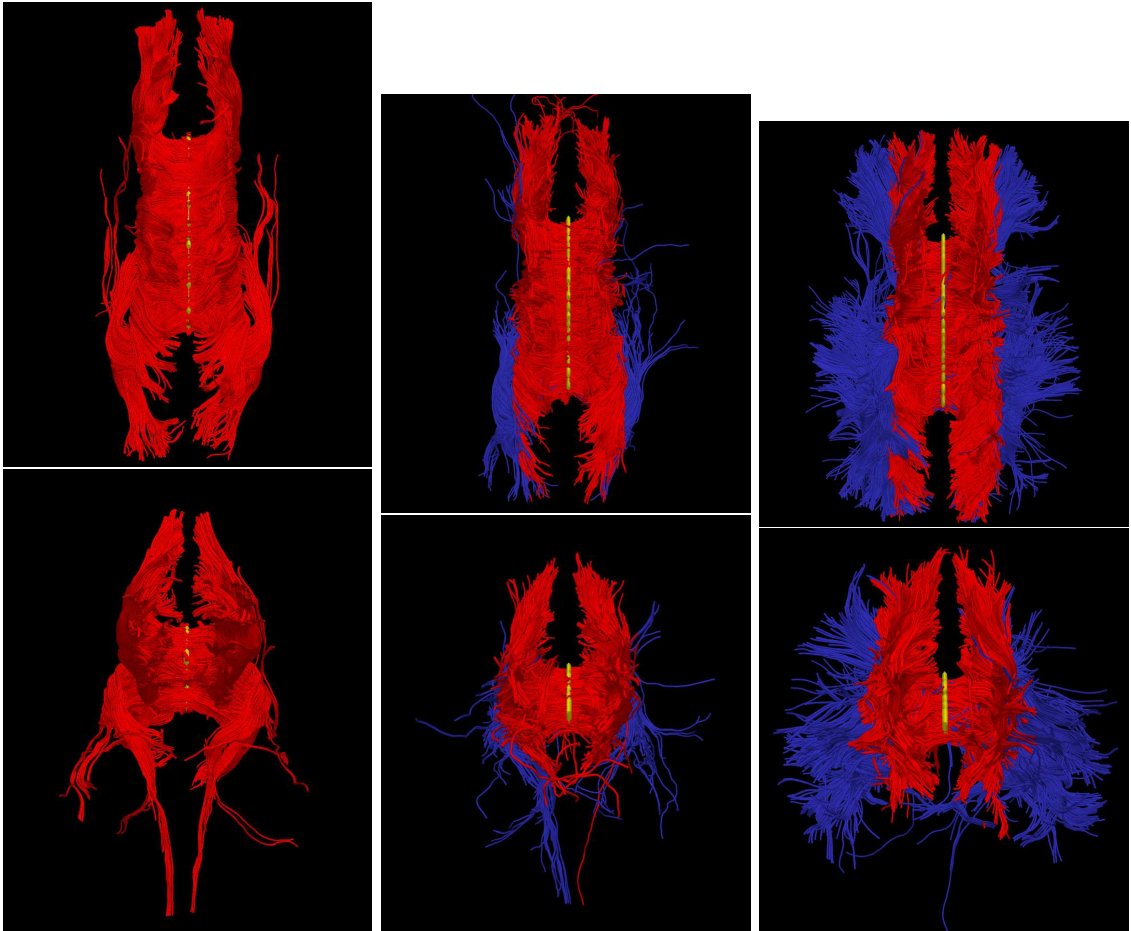


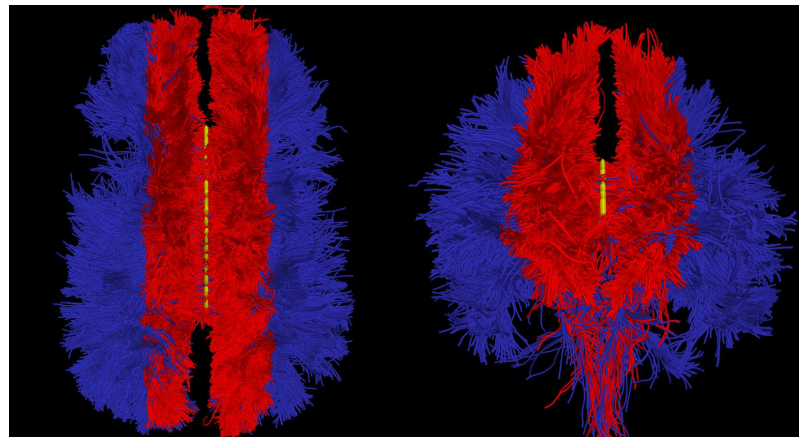
Figure 3.30: Side view with seeding in the internal capsule (*yellow*). Filtered tractography finds many insertions into cortical regions of the parietal and occipital lobes. Seed region indicated in yellow.



(a) Single-tensor

(b) Spherical harmonics

(c) Filtered two-Watson



(d) Filtered three-Watson

Figure 3.31: Tracing fibers originating from the center of the entire corpus callosum with views from above (*top rows*) and front-to-back (*bottom rows*). The proposed filtered trac- tography is able to find many of the lateral projections (*blue*) while single-tensor is unable to find any and few are found with sharpened spherical harmonics. Seed region indicated in yellow.

CHAPTER IV

WEIGHTED MIXTURES

4.1 *Summary*

Until now we have made use of two-component and three-component models, all with fixed volume fractions in the general mixture equation (Equation (1.1),Equation (2.3)). This assumption is forced upon us because update equations of the standard Kalman filter are unable to enforce the convex relationship between mixture coefficients. We began in Section 3.1.4 to explore the impact of this assumption in the presence of mixed fiber populations. A similar problem arises with the eigenvalues needing to be positive; however, for this a practical solution was to clamp these values at small positive values after each update. Our initial efforts at using the log domain to ensure positivity showed promise as an indirect method of influencing the positivity of eigenvalues, but still did not address the convexity constraint [126].

To treat the problem more directly, we began exploring constrained filtering where the state estimate is constrained to a subspace of allowable solutions [136]. In our situation, this ensures that tensor eigenvalues are positive and the mixture weights are non-negative and convex.

Section 4.1.1 defines the weighted two-fiber model employed in this section, and Section 4.1.2 describes how this model fits into the unscented Kalman filter and more importantly how the constraints are enforced. This chapter follows our work in [99, 102].

4.1.1 The weighted model

Following the equally-weighted two-tensor model from earlier (Equation (2.3)), we use it here in its more general form:

$$s_i = s_0 w_1 e^{-b \mathbf{u}_i^T D_1 \mathbf{u}_i} + s_0 w_2 e^{-b \mathbf{u}_i^T D_2 \mathbf{u}_i}, \quad (4.19)$$

Algorithm 3 Constrained Unscented Kalman Filter

1: Form weighted sigma points $\mathbf{X}_t = \{w_i, \mathbf{x}_i\}_{i=0}^{2n}$ around current mean \mathbf{x}_t and covariance P_t with scaling factor ζ

$$\mathbf{x}_0 = \mathbf{x}_t \quad \mathbf{x}_i = \mathbf{x}_t + [\sqrt{\zeta P_t}]_i \quad \mathbf{x}_{i+n} = \mathbf{x}_t - [\sqrt{\zeta P_t}]_i$$

2: Project onto the constrained subspace (Equation (4.22))

3: Predict the new sigma points and observations

$$\mathbf{X}_{t+1|t} = f[\mathbf{X}_t] \quad \mathbf{Y}_{t+1|t} = h[\mathbf{X}_{t+1|t}]$$

4: Project onto the constrained subspace (Equation (4.22))

5: Compute weighted means and covariances, *e.g.*

$$\bar{\mathbf{x}}_{t+1|t} = \sum_i w_i \mathbf{x}_i \quad P_{xy} = \sum_i w_i (\mathbf{x}_i - \bar{\mathbf{x}}_{t+1|t})(\mathbf{y}_i - \bar{\mathbf{y}}_{t+1|t})^T$$

6: Update estimate using Kalman gain K and scanner measurement \mathbf{y}_t

7: Project onto the constrained subspace (Equation (4.22))

$$\mathbf{x}_{t+1} = \bar{\mathbf{x}}_{t+1|t} + K(\mathbf{y}_t - \bar{\mathbf{y}}_{t+1|t}) \quad P_{t+1} = P_{xx} - K P_{yy} K^T \quad K = P_{xy} P_{yy}^{-1}$$

where w_1, w_2 are convex weights and D_1, D_2 are each expressible as $D = \lambda_1 \mathbf{m} \mathbf{m}^T + \lambda_2 (\mathbf{p} \mathbf{p}^T + \mathbf{q} \mathbf{q}^T)$, with $\mathbf{m}, \mathbf{p}, \mathbf{q} \in \mathbb{S}^2$ forming an orthonormal basis aligned to the principal diffusion direction \mathbf{m} . The free model parameters are then $\mathbf{m}_1, \lambda_{11}, \lambda_{21}, w_1, \mathbf{m}_2, \lambda_{12}, \lambda_{22}$, and w_2 . Lastly, we wish to constrain this model to have positive eigenvalues and convex weights ($w_1, w_2 \geq 0$ and $w_1 + w_2 = 1$).

4.1.2 Constrained estimation

As in the standard estimation process, we begin with the application-specific definition of four filter components. The only difference here is for that we directly include the weighting parameters for the two-tensor model in Equation (4.19):

$$\mathbf{x} = [\mathbf{m}_1 \ \lambda_{11} \ \lambda_{21} \ w_1 \ \mathbf{m}_2 \ \lambda_{12} \ \lambda_{22} \ w_2]^T, \quad \mathbf{m} \in \mathbb{S}^2, \lambda \in \mathbb{R}^+, w \in [0, 1]. \quad (4.20)$$

For the state transition we again assume identity dynamics, and our observation is the signal reconstruction, $\mathbf{y} = h[\mathbf{x}] = \mathbf{s} = [s_1, \dots, s_m]^T$ using s_i described by the model in Equation (4.19), and our measurement is the actual signal interpolated directly on the diffusion weighted images at the current position.

In the standard formulation (Section 2.3), we ignored the constraints on our model. This results in instabilities: the diffusion tensors may become degenerate with zero or negative eigenvalues, or the weights may become negative. To enforce appropriate constraints, one can directly project any unconstrained state \mathbf{x} onto the constrained subspace [136]. In

other words, we wish to find the state $\hat{\mathbf{x}}$ closest to the unconstrained state \mathbf{x} which still obeys the constraints, $A\hat{\mathbf{x}} \leq \mathbf{b}$. Using P_t as a weighting matrix, this becomes a quadratic programming problem:

$$\min_{\hat{\mathbf{x}}} (\mathbf{x} - \hat{\mathbf{x}})^T P_t^{-1} (\mathbf{x} - \hat{\mathbf{x}}) \quad \text{subject to} \quad A\hat{\mathbf{x}} \leq \mathbf{b}. \quad (4.21)$$

This projection procedure is applied within unscented Kalman filter procedure to correct at every place where we move in the state-space: after spreading the sigma points \mathbf{X}_t , after transforming the sigma points $\mathbf{X}_{t+1|t}$, and after the final estimate \mathbf{x}_{t+1} . See Algorithm 3.

In this study, for voxels that can be modeled with only one tensor, we found it preferable to have both the tensor components similarly oriented. Upon encountering a region of dispersion, the second component is poised and ready to begin branching instead of having zero weight and arbitrary orientation. To favor such solutions, we require the weights of each of the components to be not just non-negative but also greater than 0.2, and so, in our current implementation, A and \mathbf{b} are constructed to encode the following state constraints:

$$\lambda_{11}, \lambda_{21}, \lambda_{12}, \lambda_{22} > 0 \quad w_1, w_2 \geq 0.2 \quad w_1 + w_2 = 1. \quad (4.22)$$

4.2 Experiments

We first use experiments with synthetic data to validate our technique against ground truth. We confirm that our approach accurately recognizes crossing fibers over a broad range of angles and consistently estimates the partial volumes (Section 4.2.1). We then examine a real dataset to demonstrate how causal estimation is able to pick up fibers and branchings known to exist *in vivo* yet absent using other techniques (Section 4.2.2).

In these experiments, we compare against two alternative techniques. First, we use sharpened spherical harmonics with peak detection as described in [42] (order $l = 8$, regularization $L = 0.006$). This provides a comparison with an independently estimated non-parametric representation. Second, when performing tractography on real data, we also compare against single-tensor streamline tractography for a baseline.

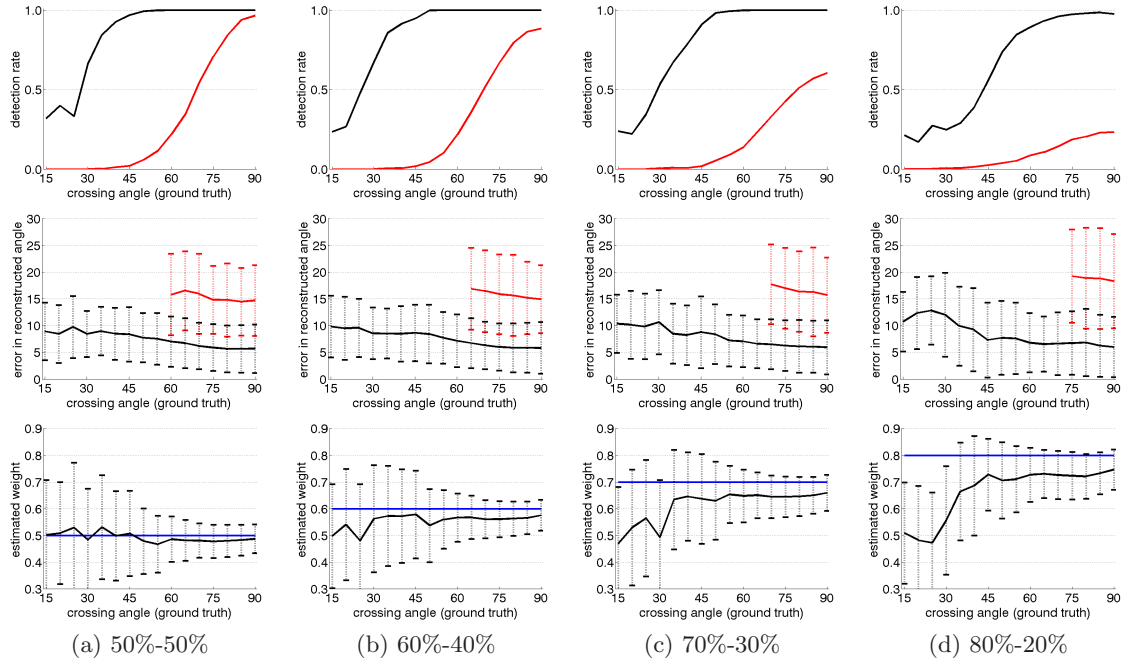


Figure 4.32: Comparison of sharpened spherical harmonics (*red*) against filtered approach (*black*) over several different metrics: detection rate, angular resolution, estimated primary fiber weight (*rows, top to bottom*). Each column is a different primary fiber weighting. The filter provides superior detection rates, accurate angular resolution, and consistent weight estimation. Trendlines indicate mean while dashed bars indicate one standard deviation.

4.2.1 Synthetic validation

Following the experimental method of generating multi-compartment synthetic data found in [42, 135, 146], we averaged the eigenvalues of the 300 voxels with highest fractional anisotropy (FA) in our real data set: $\{1200, 100, 100\} \mu\text{m}^2/\text{msec}$. We used these eigenvalues to generate synthetic MR signals according to Equation (1.1) at $b = 1000$ with 81 gradient directions on the hemisphere and introduced Rician noise ($\text{SNR} \approx 5 \text{ dB}$).

As before, we constructed a set of two-dimensional fields through which to navigate (Section 3.1.1). In the middle is one long pathway where the filter starts at one end estimating a single tensor but then runs into voxels with two crossed fibers at a fixed angle and weighting. In this crossing region we calculated error statistics to compare against sharpened spherical harmonics.

From these synthetic sets, we examined detection rate, angular resolution, and estimated volume fractions and we plot the results in Figure 4.32. Each column looks at a different

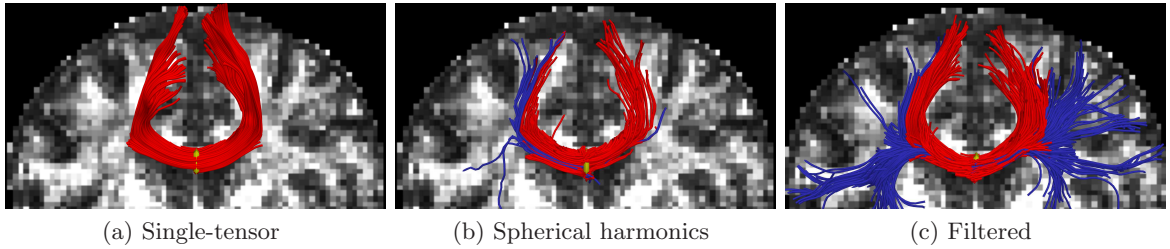


Figure 4.33: Filtered tractography picks up many fiber paths consistent with the underlying structures. Both single-tensor streamline and sharpened spherical harmonics are unable to find the majority of these pathways. Seed region indicated in yellow.

primary-secondary weighting combination, and each row looks at a different metric. In the top row, we count how many times each technique distinguishes two separate fibers. The filtered approach (*black*) is able to detect two distinct fibers at crossing angles far below that using spherical harmonics (*red*). Further, the filtered approach maintains such relatively high detection rates even at 80/20 partial voluming (*far right column*). In the middle row, we look at where each technique reported two fibers and we record the error in estimated angles. From this, we see that spherical harmonics result in an angular error of roughly 15° at best and fails to detect a second component at angles below 60°. In contrast, the filtered approach has an error between 5-10° and is able to accurately estimate down to crossing angles of 30°. In the bottom row, we look at the primary fiber weight estimated by the filter. As expected, this estimate is most accurate closer to 90° (*blue line indicates true weight*).

4.2.2 *In vivo* tractography

Our work focuses on fibers originating in the corpus callosum. Specifically, we sought to trace out the lateral transcallosal fibers that run through the corpus callosum out to the lateral gyri. It is known that single-tensor streamline tractography only traces out the dominant pathways forming the U-shaped callosal radiation while spherical harmonics only capture some of these pathways [42, 135]. These fibers have been reported in using diffusion spectrum imaging [64], probabilistic tractography [8, 42, 78], and more recently with tensor decomposition [135]; however, all of these techniques require lengthy scans at high b -values along with significantly more processing time than streamline techniques.

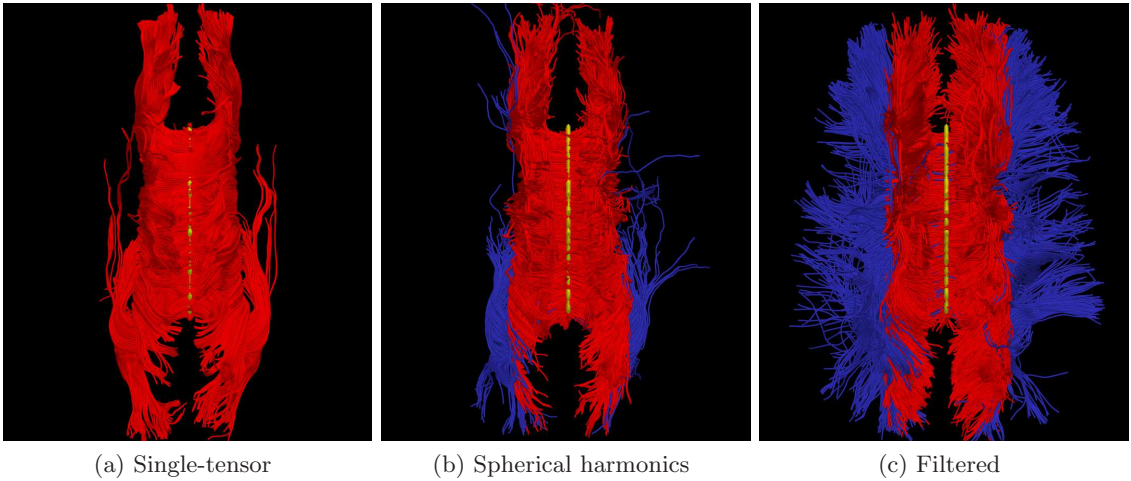


Figure 4.34: Tracing fibers originating from the center of the entire corpus callosum viewed from above. The proposed filtered tractography is able to find many of the lateral projections (*blue*) while single-tensor is unable to find any and few are found with sharpened spherical harmonics. Seed region indicated in yellow.

We begin by seeding each algorithm up to thirty times in voxels at the intersection of the mid-sagittal plane and the corpus callosum. To explore branchings found using the proposed technique, we considered a component to be branching if it was separated from the primary component by less than 40° with $\text{FA} \geq 0.15$ and weight above 0.3. Similarly, with sharpened spherical harmonics, we considered it a branch if we found additional maxima over the same range. We terminated fibers when either the generalized fractional anisotropy [146] of the estimated signal fell below 0.1 or the primary component FA fell below 0.15 or weight below 0.3.

We tested our approach on a human brain scan using a 3-Tesla magnet to collect 51 diffusion weighted images on the hemisphere at $b = 900 \text{ s/mm}^2$, a scan sequence comparable those of [42, 135]. Figure 4.33 shows tracts originating from within a few voxels intersecting a chosen coronal slice. Confirming the results in [42, 135], sharpened spherical harmonics only pick up a few fibers intersecting the U-shaped callosal radiata. In contrast, our proposed algorithm traces out many pathways consistent with the apparent anatomy. Figure 4.34 shows a view of the whole corpus callosum from above. The filtered approach is able to pick up many transcallosal fibers throughout the corpus callosum as well as infiltrating the frontal gyri to a greater degree than either alternate technique. To emphasize

transcallosal tracts, we color as blue those fibers exiting a corridor of ± 22 mm around the mid-sagittal plane.

4.3 Summary

In this section, we demonstrated that the constrained approach gives significantly lower angular error ($5\text{-}10^\circ$) in regions with fiber crossings than using sharpened spherical harmonics ($15\text{-}20^\circ$), and it reliably estimates the partial volume fractions.

While these initial results are promising, there are several aspects to be improved. First, without a prior, the weights tend toward the middle of their range, each tending to hover around 0.6 (halfway between 0.2 and 1.0). The effect is that both components show some presence, even in strongly coherent fields. The solution might be to induce priors over their distribution, hopefully forcing them to zero without signal evidence of a second component. Second, solving the quadratic constraint is expensive. A practical alternative might be to simply project as close to the subspace as possible [136]; although, this allows solutions not necessarily on the subspace and may again open the possibility for non-convex weights and negative eigenvalues. In practice, this may still be sufficient.

CHAPTER V

VALIDATION

5.1 *Summary*

In attempting to reconstruct neural pathways virtually, it is important to keep in mind the inherent uncertainty in such reconstructions. The resolution of dMRI scanners is at the level of 3-10mm³ while physical fiber axons are often an order of magnitude smaller in diameter—a relationship which leaves much room for error. Some noise or a complex fiber configuration could simply look like a diffuse signal and cause probabilistic tractography to stop in its tracks, while a few inaccurate voxel estimations could easily send the deterministic tracing off course to produce a false-positive connection. Even global methods could produce a tract that fits the signal quite well but incidentally jumps over an actual boundary in one or two voxels it thinks are noise. Consequently, a common question is: Are these pathways really present?

With this in mind, an active area of study is validating such results. Since physical dissection often requires weeks of tedious effort, many techniques have been used for validating these virtual dissections. A common starting point is to employ synthetic and physical phantoms with known parameters when evaluating new methods [122]. When possible, imaging before and after injecting radio-opaque dyes directly into the tissue can provide some of the best evidence for comparison [37,93]. Another powerful approach is to apply bootstrap sampling or other non-parametric statistical tests to judge the sensitivity and reproducibility of resulting tractography against algorithm parameters, image acquisition, and even signal noise [33,34,54,76,87,153].

To begin validating these filtered approaches, we applied this technique to a phantom simulating several complex pathway interactions and highlight tracts passing through several prescribed seed positions. This section follows our work in [100].

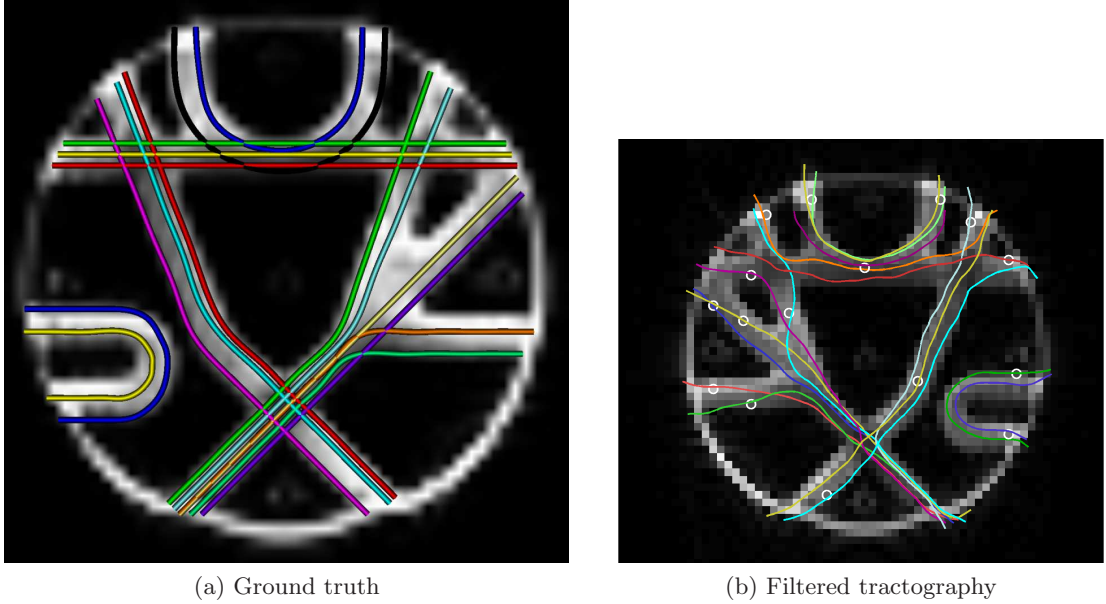


Figure 5.35: Baseline image from the synthetic phantom (3mm, $b = 1500$) overlaid with ground truth and selected fiber tracts (colored) and seed points (white). The filter is capable of tracing through regions of crossing, branching, and fanning.

5.2 Results and Discussion

Among the phantoms provided in the 2009 MICCAI Fiber Cup, we present results using the 3mm version at $b=1500$ [122]. Instead of initializing tractography from the prescribed seed points, we begin by seeding in voxels with nonzero baseline intensity and terminating tractography when the estimate becomes isotropic, essentially “full-brain” tractography. From these potential pathways, Figure 5.35 shows a representative fiber for each seed point. We further restricted movement to the image plane.

With the explosion of techniques for mapping connectivity, it is often difficult to assess the relative merits among various approaches, and each application has its particular goals. For connectivity studies, one may only be interested in the final resolved pathway; however, questions arise such as whether to branch or whether to represent connectivity as a discrete path or a voxel-to-voxel connectivity matrix possibly telling more about the relative certainty of connectivity. For tissue studies, one may be primarily concerned with the estimated microstructure at each position. Filtered approaches like this provide not only an estimate of these quantities (mean) but also an additional measure of uncertainty

(variance).

The approach presented here may be considered a local method: at the current position we estimate a direction and take a step. With such approaches, one mistake can send the subsequent trajectory off track. We believe that more global approaches should be considered, ones that take into account larger portions of the fiber pathway. Further, we believe that anatomical priors should be incorporated. Such a progression of techniques may be considered analogous to how level set methods developed from local edge-based computations, to more global region-based approaches, and further with integration of shape priors.

CHAPTER VI

TRACT-BASED STATISTICAL ANALYSIS

6.1 *Summary*

Diffusion tensor imaging has made it possible to evaluate the organization and coherence of white matter fiber tracts. Hence, it has been used in many population studies, most notably, to find abnormalities in schizophrenia. To date, most population studies analyzing fiber tracts have used a single tensor as the local fiber model. While robust, this model is known to be a poor fit in regions of crossing or branching pathways. Nevertheless, the effect of using better alternative models on population studies has not been studied. The goal of this section is to compare white matter abnormalities as revealed by two-tensor and single-tensor models. To this end, we compare three different regions of the brain from two populations: schizophrenics and normal controls. Preliminary results demonstrate that regions with significant statistical difference indicated using one-tensor model do not necessarily match those using the two-tensor model and vice-versa. We demonstrate this effect using various tensor measures. This chapter follows our work in [97].

6.2 *Introduction*

Diffusion tensor imaging (DTI) has become an established tool for investigating tissue structure, and many studies have used it to understand the effects of aging or disease. Using this imaging technique, neuroscientists wish to ask how regions of tissue compare or how well-defined various connections may be. For example, several DTI studies have indicated a disturbance in connectivity between different brain regions, rather than abnormalities within any specific region as responsible for the cognitive dysfunctions observed in schizophrenia [85]. For such studies, the quality of the results depends on the accuracy of the underlying model.

The most common local fiber model used in population studies is a single diffusion tensor which provides a Gaussian estimate of diffusion orientation and strength. While robust, this

model can be inadequate in cases of mixed fiber presence or more complex orientations, and so various alternatives have been introduced including mixture models [2, 65, 118, 146] as well as nonparametric approaches [42, 70, 73, 141, 146]. Probabilistic techniques have also been developed in connectivity studies [22, 116].

Despite this wide selection of available models, nearly all population studies thus far have been based on the single-tensor model, and as such it is important to examine the limits of this model and potential impact this has. To start, some works have focused on the effects of noise and acquisition schemes and have found nontrivial effects on estimated fractional anisotropy (FA) and other quantities [15, 57, 75]. Beyond such factors, it is known that in regions containing crossing or fanning pathways the single-tensor model itself provides a poor fit that results in lower FA [6, 146]. It is estimated that as much as one third of white matter may contain such putative fiber populations [22]. It is here that this present study focuses.

In forming studies, there are several approaches for comparing patient populations. For example, voxel-based studies examine tissue characteristics in regions of interest [9]. In contrast, tract-based studies incorporate the results of tractography to use fiber pathways as the frame of reference [44, 137], and several studies have demonstrated the importance of taking into account local fluctuations in estimated diffusion [36, 50, 58, 95, 110].

To date, many studies have focused on schizophrenia, but the findings vary. For example, the review by Kubicki et al. [85] cites one voxel-based study where the genu of the corpus callosum has significant differences and another that finds nothing. A recent tract-based study showed statistical differences not only in the genu of the corpus callosum but also in regions known to have fiber crossings and branchings [95]. The question then arises, as to whether the same effect can be seen by better models able to resolve crossings and branchings? Is the population difference simply a result of poor modeling? We seek to answer such questions in this present work.

6.3 Our contributions

In this chapter, we make a first attempt towards confirming or creating doubts regarding the results reported using the single-tensor model. Specifically, we compare various tensor metrics as estimated using two-tensor and single-tensor models on a number of fiber tracts generated using our recently proposed method for deterministic two-tensor tractography [101]. Hence we are continuing this work with a focus on how such techniques will begin affecting clinical studies. It is important to note that this is the first time the same population study has been performed using two different underlying models.

We begin with synthetic experiments to examine the difference in reported FA using single- and two-tensor models. We find that the single-tensor model consistently underestimates the FA by as much as 30% in crossing regions, a difference considered statistically significant in many studies. Then, we look at connections between three different cortical regions of the brain and show that statistical group differences reported using the single-tensor model do not necessarily show differences using the two-tensor model and vice-versa. Specifically, the regions known to have branchings and crossings reports significant differences in the single tensor study, but not in the two-tensor study, and conversely, certain regions which show subtle abnormalities using the two-tensor method are lost in the single-tensor model. Thus, model error may have contributed to the statistical differences found in previous DTI studies.

6.4 Method

In this chapter, we form a tract-based study using the two-tensor tractography method described in Section 2.2.1, and we compare this against the results from a single-tensor model typically used in such studies. Section 2.2 provides the necessary background on modeling the measured signal using tensors and defines the specific two-fiber model employed in this study. Section 6.5 looks at the seed regions and the resulting fibers connecting each hemisphere and finally how these fibers are compared within a tract-based coordinate system.

Several scalar measures have been proposed for quantifying various aspects of tensors,

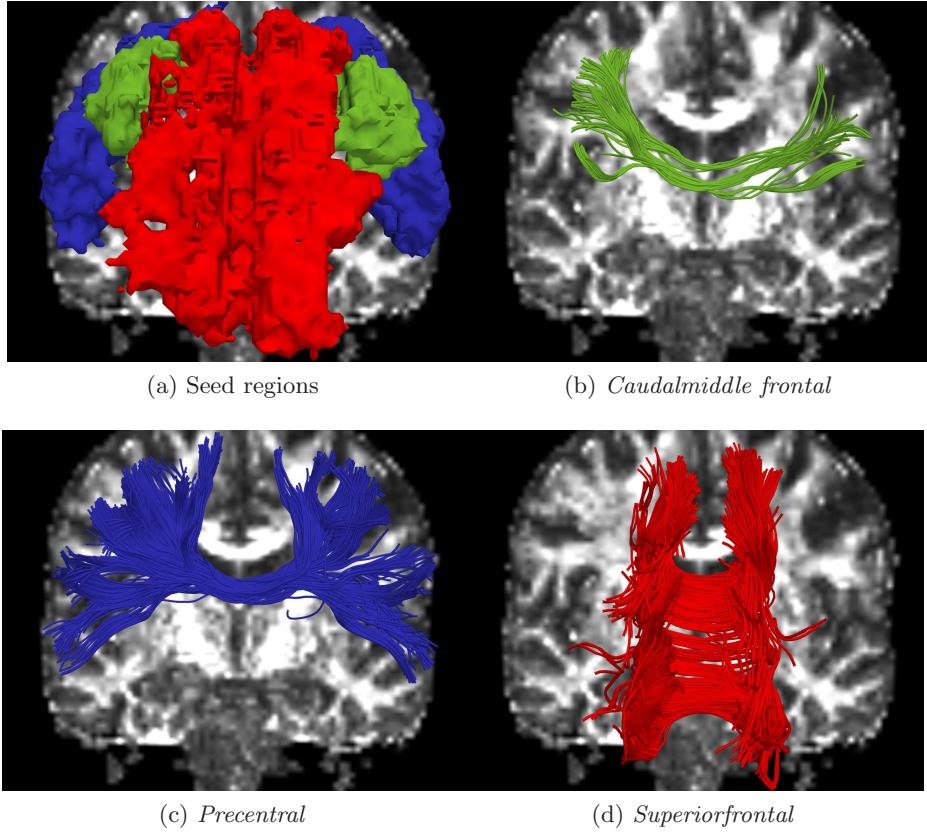


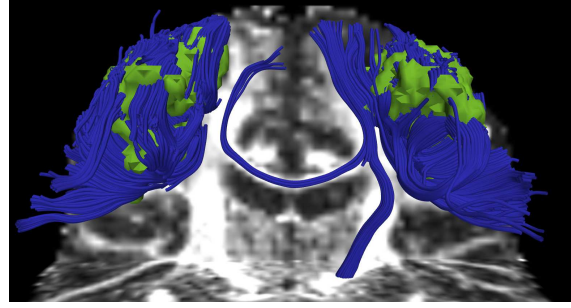
Figure 6.36: For each patient, we seed in three different cortical regions and select only those fibers that connect the hemispheres.

and in this study we focus on fractional anisotropy (FA), trace, and the ratio between eigenvalues (λ_2/λ_1). Since these measures are defined for the single-tensor model, when computing their value on the two-tensor model, we record the value from the tensor most aligned with the local fiber tangent.

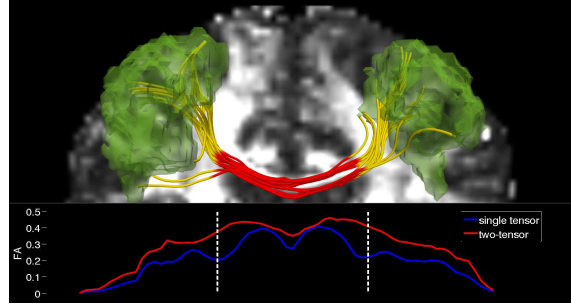
6.5 Tractography and fiber comparison

For each patient, we have manually delineated cortical regions from which we choose three regions covering the frontal and parietal lobe. For one patient, Figure 6.36 shows these seed regions and the resulting fibers that connect each hemisphere. Specifically, the regions are the *superiorfrontal*, *precentral*, and *caudalmiddle frontal*.

We followed the deterministic fiber tracking procedure in [101]. We begin by seeding each algorithm several times in each voxel of the seed regions. To explore branchings found



(a) Single-tensor.

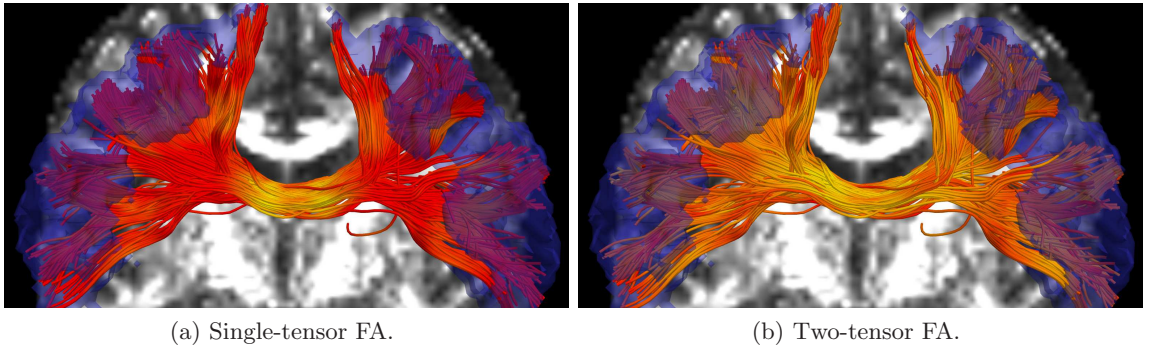


(b) Two-tensor and FA curves

Figure 6.37: Single-tensor tractography finds no connections. Two-tensor passes through the region of crossing (*red/yellow boundary*). FA curves show drop in single-tensor FA (*blue*) in this region (*indicated by dashed white line*).

using the proposed technique, we considered a component to be branching if it was separated from the primary component by less than 40° with $\text{FA} \geq 0.15$. We terminated fibers when either the general fractional anisotropy [146] of the estimated signal fell below 0.1 or the primary component FA fell below 0.15. While such parameters are heuristic in nature and could be examined in their own right, we found the resulting tractography to be sufficient for the purposes of this work.

It is known that single-tensor streamline tractography is only able to trace out the dominant pathways forming the U-shaped callosal radiation, so previous tract-based studies looking at the corpus callosum have been restricted to only studying portions of the corpus radiata, typically focusing on the splenium and genu [36, 50, 56, 95]. One of the main advantages of using the multi-tensor filtering approach in [101] is that it is one of the few techniques capable of following, not only these dominate pathways, but also the transcallosal pathways out to the lateral gyri. For example, Figure 6.37a shows that for the



(a) Single-tensor FA.

(b) Two-tensor FA.

Figure 6.38: Two-tensor fibers overlayed with FA intensity using both models (*red to yellow is low to high*). Both methods show high FA in the corpus callosum but single-tensor FA drops as fibers enter the gray matter.

caudalmiddle frontal region, using single-tensor tractography leads to nearly all fibers looping back into another sulci instead of finding any connection to the opposite hemisphere. In contrast, Figure 6.37b demonstrates that the filtered two-tensor approach finds several connecting pathways. Therefore, this is the first attempt at tract-oriented analysis along such pathways.

Since this study focuses on comparing fiber models, we simply perform direct single-tensor estimation at the same locations as we have two-tensor estimates, thus providing an exact correspondence for averaging within each patient. Figure 6.38 shows the *precentral* region and colors the same fibers with FA intensity to show the relative FA differences reported by either model.

After performing tractography, we placed fibers from each patient within a common coordinate system by registering the seed regions to a template. Each seed region was registered separately. The mid-sagittal plane was automatically determined and provided a common reference point for each fiber as it passed through the corpus callosum. From this reference point, we record arc-length moving outward to the cortical regions. The fibers of each patient being registered with a template and having an origin, we can plot the various scalar tensor measures along this arc-length as in other tract-based studies. For example, Figure 6.37b shows FA as a function of arc-length for the *caudalmiddle frontal* region using the single-tensor model (*blue*) and two-tensor model (*red*). Since the single- and two-tensor estimates line up exactly, any correspondence error is confined to the matching within fiber

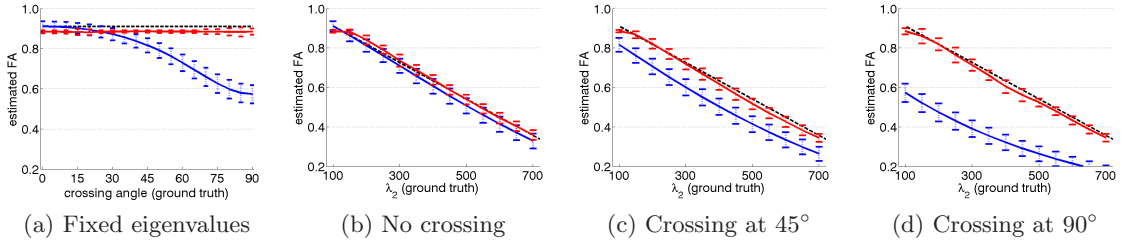


Figure 6.39: Estimated fractional anisotropy (FA) using single-tensor (*blue*) and two-tensor (*red*) models on synthetic data with known FA (*dashed black*). The two-tensor model accurately captures the FA across a wide range of angles and eigenvalues.

bundles and among patients—not across models which was our focus here. As in [95, 110], statistical significance was tested as a function of arc-length.

6.6 Results

We first use experiments with synthetic data to validate our technique against ground truth. By varying crossing angle or eigenvalues used to construct voxels, we confirm that our approach accurately estimates the fractional anisotropy while using the single-tensor model can under-estimate FA by as much as 30-40%. (Section 6.6.1). Then, we examine our real dataset to demonstrate the different results reported using either model (Section 6.6.2).

6.6.1 Synthetic validation

Following the experimental method of generating synthetic data found in [42, 141], we generated synthetic MR signals according to Equation (2.3) using eigenvalues determined from out *in vivo* data. We use 81 gradient directions uniformly spread on the hemisphere and Rician noise ($\text{SNR} \approx 10 \text{ dB}$) based on the unweighted signal. Using these we constructed a set of two-dimensional fields through which to navigate while estimating FA.

Figure 6.39 shows the resulting FA estimates using direct single-tensor estimation (*blue*) and filtered two-tensor estimation (*red*). As expected, Figure 6.39a demonstrates that crossing regions can lead to single-tensor FA estimates as much as 0.3 lower than expected. In Figure 6.39b we look at both techniques accurately estimating the FA of a single tensor as we adjust the second eigenvalue (λ_2 in Equation (2.3)). However, Figure 6.39c and 6.39d demonstrate a consistent drop in FA under the same range of eigenvalues. This experiment

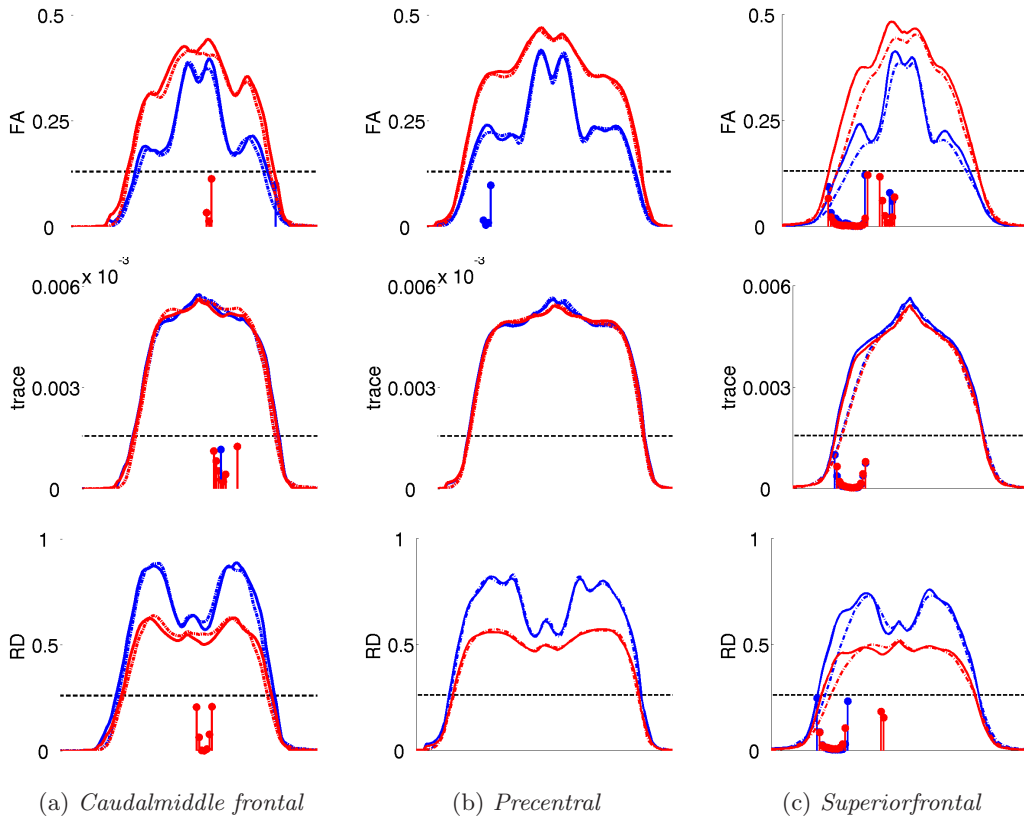


Figure 6.40: Average of various tensor metrics as a function of arc-length using single-tensor (blue) and two-tensor (red) models comparing normal patients (solid lines) with schizophrenic patients (dotted lines). Rows show FA, trace, eigenvalue ratio. Areas of statistical significance are indicated along the bottom (*black dashes indicate 95% confidence*). While each metric generally indicates the same area of significance (*looking down columns*), the areas of significance vary with each model (*comparing red and blue*)

demonstrates that we may expect as much as 0.2 to 0.3 drop in FA in regions of crossing and branching.

6.6.2 *In vivo* model comparison

We tested our approach on a human brain scans using a 3-Tesla magnet to collect 51 diffusion weighted images on the hemisphere at a voxel size of $1.66 \times 1.66 \times 1.7 \text{ mm}^3$ and with $b = 900 \text{ s/mm}^2$ in addition to eight baseline scans. Included in this study are 17 normal controls and 22 schizophrenics; however, since not connecting fibers were not found in all patients for all regions, not all patients were represented in each regional group. Below are the sizes for each region and group.

	<i>Caudalmiddle frontal</i>	<i>Precentral</i>	<i>Superiorfrontal</i>
Normals	16	17	8
Schizophrenics	20	22	17

For each region and patient group, Figure 6.40 shows the resulting average curves using the single-tensor (*blue*) and two-tensor (*red*) models. Along the bottom of each plot we indicate local regions of statistical significance between groups. In Figure 6.40a we see that the two-tensor model detected a region of significance across all three measures whereas the single-tensor model found only one small portion of that in the trace. As Figure 6.37b indicates, this a region known to contain branching and crossing, hence the single-tensor FA drop. Thus, we suspect that the single-tensor was unable to provide a tight enough fit in this region to detect the difference found using the two-tensor model. In Figure 6.40b we see that the single-tensor model found a slight area again in a region of known branching, yet the two-tensor model found nothing. In Figure 6.40c we see the most reported differences and further we see those differences reported using both models. We note that these differences may in part be due to the relative size of each population supporting this region. In summary, among these three regions, we see areas where each model either confirmed or denied the findings of the other.

6.7 Conclusion

There are many challenges in building automatic frameworks for detecting population differences. By repeating the same tract-based study and changing only the model, we have demonstrated that the ultimate findings may vary. Specifically, our results indicate that some areas reported as significant using the single-tensor model may in fact be due to poor modeling at branchings or crossings.

While our results are preliminary, we believe that exploring both alternative models and methods of reconstructing pathways will provide more accurate and comprehensive information about neural pathways and ultimately enhance non-invasive diagnosis and treatment of brain disease.

Considering future work, we expect that further model discrepancies may be revealed

with more accurate fiber and patient correspondences [95, 110] or functional representations [56].

CHAPTER VII

SUMMARY

Studies involving deterministic tractography rely on the underlying model estimated at each voxel as well as the reconstructed pathways. Most of the work on deterministic and probabilistic tractography has involved estimating the fiber-ODF independently at each voxel and performing tractography as a post-processing step with path regularization. In this work, we proposed a method for simultaneous estimation and tractography using two- and three-tensor mixtures. Using an unscented Kalman filter provided robust parameter estimation and demonstrated significantly higher angular accuracy compared to various nonparametric and independent optimization techniques. Specifically we found an angular error of 5-10° in regions with fiber crossings compared to 15-20° using a common spherical harmonic technique, and it is able to reliably resolve crossings down to 20-30° compared to spherical harmonics which reaches only down to 50-60°. *In vivo* experiments demonstrate the ability of the proposed method to reveal fibers known to exist anatomically, *e.g.* lateral transcallosal fibers or temporal insertions along the fronto-occipital fasciculus, yet absent using the comparison techniques.

Nevertheless, there are several aspects of this technique that could be improved in future work. First, we believe improvements can certainly be made with the local model. For example, switching filters may provide a natural method for reduced parameter estimation where appropriate. Further, we believe it is still important to explore constrained models (convex weights, positive eigenvalues) [102] as well as approaches at model selection [22].

Second, as is often the case in tractography, reported connections may be invalid (false-positives). For example, the partial voluming along the cingulum bundle in Figure 3.20 causes many spurious traces. There are several possible approaches to suppressing such false positives (*e.g.* higher resolution scans, more appropriate local models, alternative filter formulations), but we believe that incorporating global information will ultimately have

more effect than more local choices in the model or filter.

In summary, we believe that filtering techniques offer significant increases in sensitivity over traditional independent optimization methods, but care must be taken ensuring anatomically correct results. We believe that exploring both alternative models and filtering techniques will provide more accurate and comprehensive information about neural pathways and ultimately enhance non-invasive diagnosis and treatment of brain disease.

REFERENCES

- [1] AJA-FERNANDEZ, S., NIETHAMMER, M., KUBICKI, M., SHENTON, M. E., and WESTIN, C.-F., “Restoration of DWI data using a Rician LMMSE estimator,” *Trans. on Med. Imag.*, vol. 27, pp. 1389–1403, 2008.
- [2] ALEXANDER, A., HASAN, K., TSURUDA, J., and PARKER, D., “Analysis of partial volume effects in diffusion-tensor MRI,” *Magnetic Resonance in Medicine*, vol. 45, pp. 770–780, 2001.
- [3] ALEXANDER, D. C., “An introduction to computational diffusion MRI: the diffusion tensor and beyond,” in *Visualization and Image Processing of Tensor Fields* (WEICHERT, J. and HAGEN, H., eds.), ch. 5, Springer, 2005.
- [4] ALEXANDER, D. C., “Maximum entropy spherical deconvolution for diffusion MRI,” in *Information Processing in Medical Imaging (IPMI)*, pp. 76–87, 2005.
- [5] ALEXANDER, D. C., “Modelling, fitting and sampling in diffusion MRI,” in *Visualization and Processing of Tensor Fields*, ch. 1, pp. 3–20, Springer, 2009.
- [6] ALEXANDER, D. C., BARKER, G., and ARRIDGE, S., “Detection and modeling of non-Gaussian apparent diffusion coefficient profiles in human brain data,” *Magnetic Resonance in Medicine*, vol. 48, pp. 331–340, 2002.
- [7] ANDERSON, A., “Measurement of fiber orientation distributions using high angular resolution diffusion imaging,” *Magnetic Resonance in Medicine*, vol. 54, no. 5, pp. 1194–1206, 2005.
- [8] ANWANDER, A., DESCOTEAUX, M., and DERICHE, R., “Probabilistic Q-Ball tractography solves crossings of the callosal fibers,” in *Human Brain Mapping*, p. 342, 2007.
- [9] ASHBURNER, J. and FRISTON, K., “Voxel-based morphometry—The methods,” *NeuroImage*, vol. 11, no. 6, pp. 805–821, 2000.
- [10] ASSAF, Y. and BASSER, P., “Composite hindered and restricted model of diffusion (CHARMED) MR imaging of the human brain,” *NeuroImage*, vol. 27, pp. 48–58, 2005.
- [11] ASSAF, Y., BLUMENFELD-KATZIR, T., YOVEL, Y., and BASSER, P. J., “AxCaliber: A method for measuring axon diameter distribution from diffusion MRI,” *Magnetic Resonance in Medicine*, vol. 59, pp. 1347–1354, 2008.
- [12] ASSEMLAL, H.-E., TSCHUMPERLÉ, D., and BRUN, L., “Robust variational estimation of PDF functions from diffusion MR signal,” in *Workshop on Computational Diffusion MRI*, 2008.

- [13] BARMPOUTIS, A., HWANG, M. S., HOWLAND, D., FORDER, J., and VEMURI, B., “Regularized positive-definite fourth order tensor field estimation from DW-MRI,” *Neuroimage*, 2009.
- [14] BASSER, P., MATTIELLO, J., and LEBIHAN, D., “Estimation of the effective self-diffusion tensor from the NMR spin echo,” *J. of Magnetic Resonance*, vol. 103, pp. 247–254, 1994.
- [15] BASSER, P. and PAJEVIC, S., “Statistical artifacts in diffusion tensor MRI (DT-MRI) caused by background noise,” *Magnetic Resonance in Medicine*, vol. 44, no. 1, pp. 41–50, 2000.
- [16] BASSER, P., PAJEVIC, S., PIERPAOLI, C., DUDA, J., and ALDROUBI, A., “In vivo fiber tractography using DT-MRI data,” *Magnetic Resonance in Medicine*, vol. 44, pp. 625–632, 2000.
- [17] BASSER, P. J. and PAJEVIC, S., “Spectral decomposition of a 4th-order covariance tensor: Applications to diffusion tensor MRI,” *Signal Processing*, vol. 87, pp. 220–236, 2007.
- [18] BASSER, P. J. and PIERPAOLI, C., “Microstructural features measured using diffusion tensor imaging,” *J. of Magnetic Resonance*, vol. 111, pp. 209–219, 1996.
- [19] BATCHELOR, P. G., HILL, D. L., CALAMANTE, F., and ATKINSON, D., “Study of connectivity in the brain using the full diffusion tensor from MRI,” in *Information Processing in Medical Imaging (IPMI)*, pp. 121–133, 2001.
- [20] BATCHELOR, P. G., MOAKHER, M., ATKINSON, D., CALAMANTE, F., and CONNELLY, A., “A rigorous framework for diffusion tensor calculus,” *Magnetic Resonance in Medicine*, vol. 53, no. 1, pp. 221–225, 2005.
- [21] BEAULIEU, C., “The basis of anisotropic water diffusion in the nervous system—A technical review,” *NMR in Biomedicine*, vol. 15, pp. 438–455, 2002.
- [22] BEHRENS, T., JOHANSEN-BERG, H., JBABDI, S., RUSHWORTH, M., and WOOLRICH, M., “Probabilistic diffusion tractography with multiple fibre orientations: What can we gain?,” *NeuroImage*, vol. 34, pp. 144–155, 2007.
- [23] BEHRENS, T., WOOLRICH, M., JENKINSON, M., JOHANSEN-BERG, H., NUNES, R., CLARE, S., MATTHEWS, P., BRADY, J., and SMITH, S., “Characterization and propagation of uncertainty in diffusion-weighted MR imaging,” *Magnetic Resonance in Medicine*, vol. 50, pp. 1077–1088, 2003.
- [24] BEHRENS, T. E. J., JOHANSEN-BERG, H., WOOLRICH, M. W., SMITH, S. M., WHEELER-KINGSHOTT, C. A. M., BOULBY, P. A., BARKER, G. J., SILLERY, E. L., SHEEHAN, K., CICCRELLI, O., THOMPSON, A. J., BRADY, J. M., and MATHEWS, P. M., “Non-invasive mapping of connections between human thalamus and cortex using diffusion imaging,” *Nature Neuroscience*, vol. 6, no. 7, pp. 750–757, 2003.
- [25] BERGMANN, O., KINDLMANN, G., LUNDERVOLD, A., and WESTIN, C.-F., “Diffusion k-tensor estimation from Q-Ball imaging using discretized principal axes,” in *Medical Image Computing and Computer Assisted Intervention (MICCAI)*, pp. 268–275, 2006.

- [26] BIHAN, D. L., "Looking into the functional architecture of the brain with diffusion MRI," *Nature Reviews Neuroscience*, vol. 4, pp. 469–480, 2003.
- [27] BJÖRNEMO, M., BRUN, A., KIKINIS, R., and WESTIN, C.-F., "Regularized stochastic white matter tractography using diffusion tensor MRI," in *Medical Image Computing and Computer Assisted Intervention (MICCAI)*, pp. 435–442, 2002.
- [28] BLOY, L. and VERMA, R., "On computing the underlying fiber directions from the diffusion orientation distribution function," in *Medical Image Computing and Computer Assisted Intervention (MICCAI)*, pp. 1–8, 2008.
- [29] BRUN, A., KNUTSSON, H., PARK, H. J., SHENTON, M. E., and WESTIN, C.-F., "Clustering fiber traces using normalized cuts," in *Medical Image Computing and Computer Assisted Intervention (MICCAI)*, pp. 368–375, 2004.
- [30] BULLMORE, E. and SPORNS, O., "Complex brain networks: graph theoretical analysis of structural and functional systems," *Nature Reviews Neuroscience*, vol. 10, pp. 186–198, 2009.
- [31] CAAN, M., VERMEER, K., VAN VLIET, L., MAJOIE, C., PETERS, B., DEN HEETEN, G., and VOS, F., "Shaving diffusion tensor images in discriminant analysis: A study into Schizophrenia," *Medical Image Analysis*, vol. 10, no. 6, pp. 841–849, 2006.
- [32] CAMPBELL, J. S. W., SIDDIQI, K., RYMAR, V. V., SADIKOT, A. F., and PIKE, G. B., "Flow-based fiber tracking with diffusion tensor and Q-ball data: Validation and comparison to principal diffusion direction techniques," *NeuroImage*, vol. 27, no. 4, pp. 725–736, 2005.
- [33] CHUNG, S., LU, Y., and HENRY, R., "Comparison of bootstrap approaches for estimation of uncertainties of DTI parameters," *NeuroImage*, vol. 33, no. 2, pp. 531–541, 2006.
- [34] CLAYDEN, J., STORKEY, A., and BASTIN, M., "A probabilistic model-based approach to consistent white matter tract segmentation," *Trans. on Med. Imag.*, vol. 26, no. 11, pp. 1555–1561, 2007.
- [35] CLAYDEN, J. D., STORKEY, A. J., MANIEGA, S. M., and BASTIN, M. E., "Reproducibility of tract segmentation between sessions using an unsupervised modelling-based approach," *NeuroImage*, vol. 45, pp. 377–385, 2009.
- [36] COROUGE, I., FLETCHER, P. T., JOSHI, S., GOUTTARD, S., and GERIG, G., "Fiber tract-oriented statistics for quantitative diffusion tensor MRI analysis," *Medical Image Analysis*, vol. 10, no. 5, pp. 786–798, 2006.
- [37] DAUGUET, J., PELED, S., BEREZOVSKII, V., DELZESCAUX, T., WARFIELD, S. K., BORN, R., and WESTIN, C.-F., "Comparison of fiber tracts derived from in-vivo DTI tractography with 3D histological neural tract tracer reconstruction on a macaque brain," *NeuroImage*, vol. 37, pp. 530–538, 2007.
- [38] DE LUIS-GARCIA, R. and ALBEROLA-LOPEZ, C., "Mixtures of Gaussians on tensor fields for the segmentation of DT-MRI," in *Medical Image Computing and Computer Assisted Intervention (MICCAI)*, pp. 319–326, 2007.

- [39] DERICHE, R., CALDER, J., and DESCOTEAUX, M., “Optimal real-time Q-Ball imaging using regularized Kalman filtering with incremental orientation sets,” *Medical Image Analysis*, vol. 13, no. 4, pp. 564–579, 2009.
- [40] DESCOTEAUX, M., *High Angular Resolution Diffusion MRI: from Local Estimation to Segmentation and Tractography*. PhD thesis, University of Nice-Sophia Antipolis, 2008.
- [41] DESCOTEAUX, M., ANGELINO, E., FITZGIBBONS, S., and DERICHE, R., “Regularized, fast, and robust analytical Q-ball imaging,” *Magnetic Resonance in Medicine*, vol. 58, pp. 497–510, 2007.
- [42] DESCOTEAUX, M., DERICHE, R., and ANWANDER, A., “Deterministic and probabilistic Q-ball tractography: from diffusion to sharp fiber distributions,” Tech. Rep. 6273, INRIA, 2007.
- [43] DESCOTEAUX, M., DERICHE, R., KNOESCHE, T., and ANWANDER, A., “Deterministic and probabilistic tractography based on complex fiber orientation distributions,” *Trans. on Med. Imag.*, vol. 28, no. 2, pp. 269–286, 2009.
- [44] DING, Z., GORE, J., and ANDERSON, A., “Classification and quantification of neuronal fiber pathways using diffusion tensor MRI,” *Magnetic Resonance in Medicine*, vol. 49, pp. 716–721, 2003.
- [45] DURRLEMAN, S., FILLARD, P., PENNEC, X., TROUVÉ, A., and AYACHE, N., “A statistical model of white matter fiber bundles based on currents,” in *Information Processing in Medical Imaging (IPMI)*, pp. 114–125, 2009.
- [46] ECKSTEIN, I., SHATTUCK, D. W., STEIN, J. L., McMAHON, K. L., DE ZUBICARAY, G., WRIGHT, M. J., THOMPSON, P. M., and TOGA, A. W., “Active fibers: Matching deformable tract templates to diffusion tensor images,” *NeuroImage*, vol. 47, pp. T82–T89, 2009.
- [47] ENNIS, D. B., KINDLMANN, G., RODRIGUEZ, I., HELM, P. A., and MCVEIGH, E. R., “Visualization of tensor fields using superquadric glyphs,” *Magnetic Resonance in Medicine*, vol. 53, pp. 169–176, 2005.
- [48] FILLARD, P., POUPEON, C., and MANGIN, J.-F., “A novel global tractography algorithm based on an adaptive spin glass model,” in *Medical Image Computing and Computer Assisted Intervention (MICCAI)*, pp. 927–934, 2009.
- [49] FLETCHER, P. T. and JOSHI, S., “Riemannian geometry for the statistical analysis of diffusion tensor data,” *Signal Processing*, vol. 87, no. 2, pp. 250–262, 2007.
- [50] FLETCHER, P. T., TAO, R., JOENG, W. K., and WHITAKER, R., “A volumetric approach to quantifying region-to-region white matter connectivity in diffusion tensor MRI,” in *Information Processing in Medical Imaging (IPMI)*, pp. 346–358, 2007.
- [51] FRANK, L., “Characterization of anisotropy in high angular resolution diffusion-weighted MRI,” *Magnetic Resonance in Medicine*, vol. 47, pp. 1083–1099, 2002.

- [52] FREIDLIN, R. Z., ÖZARSLAN, E., KOMLOSH, M. E., CHANG, L.-C., KOAY, C. G., JONES, D. K., and BASSER, P. J., “Parsimonious model selection for tissue segmentation and classification applications: A study using simulated and experimental DTI data,” *Trans. on Med. Imag.*, vol. 26, no. 11, pp. 1576–1584, 2007.
- [53] FRIMAN, O., FARNEBÄCK, G., and WESTIN, C.-F., “A Bayesian approach for stochastic white matter tractography,” *Trans. on Med. Imag.*, vol. 25, no. 8, pp. 965–978, 2006.
- [54] GIGANDET, X., HAGMANN, P., KURANT, M., CAMMOUN, L., MEULI, R., and THIRAN, J.-P., “Estimating the confidence level of white matter connections obtained with MRI tractography,” *PLoS ONE*, vol. 3, no. 12, p. e4006, 2008.
- [55] GONG, G., HE, Y., CONCHA, L., LEBEL, C., GROSS, D. W., EVANS, A. C., and BEAULIEU, C., “Mapping anatomical connectivity patterns of human cerebral cortex using in vivo diffusion tensor imaging tractography,” *Cerebral Cortex*, vol. 19, no. 3, pp. 524–536, 2009.
- [56] GOODLETT, C., FLETCHER, P. T., GILMORE, J., and GERIG, G., “Group statistics of DTI fiber bundles using spatial functions of tensor measures,” in *Medical Image Computing and Computer Assisted Intervention (MICCAI)*, pp. 1068–1075, 2008.
- [57] GOODLETT, C., FLETCHER, P. T., LIN, W., and GERIG, G., “Quantification of measurement error in DTI: Theoretical predictions and validation,” in *Medical Image Computing and Computer Assisted Intervention (MICCAI)*, pp. 10–17, 2007.
- [58] GOODLETT, C. B., FLETCHER, P. T., GILMORE, J. H., and GERIG, G., “Group analysis of DTI fiber tract statistics with application to neurodevelopment,” *NeuroImage*, vol. 45, pp. S133–S142, 2009.
- [59] GÖSSL, C., FAHRMEIR, L., PUTZ, B., AUER, L., and AUER, D., “Fiber tracking from DTI using linear state space models: Detectability of the pyramidal tract,” *NeuroImage*, vol. 16, pp. 378–388, 2002.
- [60] GUO, W., ZENG, Q., CHEN, Y., and LIU, Y., “Using multiple tensor deflection to reconstruct white matter fiber traces with branching,” in *Int. Symp. on Biomedical Imaging*, pp. 69–72, 2006.
- [61] HAGMANN, P., *From Diffusion MRI to Brain Connectomics*. PhD thesis, Université de Lausanne, 2005.
- [62] HAGMANN, P., CAMMOUN, L., GIGANDET, X., MEULI, R., HONEY, C. J., WEDEEN, V. J., and SPORNS, O., “Mapping the structural core of human cerebral cortex,” *PLoS Biology*, vol. 6, no. 7, p. e159, 2008.
- [63] HAGMANN, P., KURANT, M., GIGANDET, X., THIRAN, P., WEDEEN, V. J., MEULI, R., and THIRAN, J. P., “Mapping human whole-brain structural networks with diffusion MRI,” *PLoS ONE*, vol. 2, no. 7, p. e597, 2007.
- [64] HAGMANN, P., REESE, T., TSENG, W.-Y., MEULI, R., THIRAN, J.-P., and WEDEEN, V. J., “Diffusion spectrum imaging tractography in complex cerebral white matter: An investigation of the centrum semiovale,” in *Int. Symp. on Magnetic Resonance in Medicine (ISMRM)*, p. 623, 2004.

- [65] HALL, M. G. and ALEXANDER, D. C., “Agreement and disagreement in two models of synthetic diffusion MR data,” in *Int. Symp. on Magnetic Resonance in Medicine (ISMRM)*, p. 1780, 2008.
- [66] HESS, C., MUKHERJEE, P., HAN, E., XU, D., and VIGNERON, D., “Q-ball reconstruction of multimodal fiber orientations using the spherical harmonic basis,” *Magnetic Resonance in Medicine*, vol. 56, pp. 104–117, 2006.
- [67] HONEY, C. J., SPORNS, O., CAMMOUN, L., GIGANDET, X., THIRAN, J. P., MEULIC, R., and HAGMANN, P., “Predicting human resting-state functional connectivity from structural connectivity,” *Proc. National Academy of Sciences*, vol. 106, no. 6, pp. 2035–2040, 2009.
- [68] HORSFIELD, M. A. and JONES, D. K., “Neuropsychiatric applications of DTI – A review,” *NMR in Biomedicine*, vol. 15, pp. 587–593, 2002.
- [69] HOSEY, T., WILLIAMS, G., and ANSORGE, R., “Inference of multiple fiber orientations in high angular resolution diffusion imaging,” *Magnetic Resonance in Medicine*, vol. 54, pp. 1480–1489, 2005.
- [70] JANSONS, K. and ALEXANDER, D. C., “Persistent angular structure: New insights from diffusion MRI data,” *Inverse Problems*, vol. 19, pp. 1031–1046, 2003.
- [71] JBABDI, S., WOOLRICH, M., ANDERSSON, J., and BEHRENS, T., “A bayesian framework for global tractography,” *NeuroImage*, vol. 37, pp. 116–129, 2007.
- [72] JIAN, B. and VEMURI, B., “A unified computational framework for deconvolution to reconstruct multiple fibers from diffusion weighted MRI,” *Trans. on Med. Imag.*, vol. 26, no. 11, pp. 1464–1471, 2007.
- [73] JIAN, B., VEMURI, B., ÖZARSLAN, E., CARNEY, P. R., and MARECI, T. H., “A novel tensor distribution model for the diffusion-weighted MR signal,” *NeuroImage*, vol. 37, no. 1, pp. 164–176, 2007.
- [74] JONES, D. K., “Determining and visualizing uncertainty in estimates of fiber orientation from diffusion tensor MRI,” *Magnetic Resonance in Medicine*, vol. 49, pp. 7–12, 2003.
- [75] JONES, D. K. and BASSER, P. J., “Squashing peanuts and smashing pumpkins: How noise distorts diffusion-weighted MR data,” *Magnetic Resonance in Medicine*, vol. 52, no. 5, pp. 979–993, 2004.
- [76] JONES, D. K. and PIERPAOLI, C., “Confidence mapping in diffusion tensor magnetic resonance imaging tractography using a bootstrap approach,” *Magnetic Resonance in Medicine*, vol. 53, no. 5, pp. 1143–1149, 2005.
- [77] JULIER, S. and UHLMANN, J., “Unscented filtering and nonlinear estimation,” *IEEE*, vol. 92, no. 3, pp. 401–422, 2004.
- [78] KADEN, E., KNÖSCHE, T., and ANWANDER, A., “Parametric spherical deconvolution: Inferring anatomical connectivity using diffusion MR imaging,” *NeuroImage*, vol. 37, pp. 474–488, 2007.

- [79] KINDLMANN, G., ENNIS, D. B., WHITAKER, R. T., and WESTIN, C.-F., “Diffusion tensor analysis with invariant gradients and rotation tangents,” *Trans. on Med. Imag.*, vol. 26, no. 11, pp. 1483–1499, 2007.
- [80] KINDLMANN, G., ESTEPAR, R., NIETHAMMER, M., HAKER, S., and WESTIN, C.-F., “Geodesic-loxodromes for diffusion tensor interpolation and difference measurement,” in *Medical Image Computing and Computer Assisted Intervention (MICCAI)*, pp. 1–9, 2007.
- [81] KOAY, C. G. and BASSER, P. J., “Analytically exact correction scheme for signal extraction from noisy magnitude MR signals,” *J. of Magnetic Resonance*, vol. 179, pp. 317–322, 2006.
- [82] KOCH, M. A., NORRIS, D. G., and HUND-GEORGIADIS, M., “An investigation of functional and anatomical connectivity using magnetic resonance imaging,” *NeuroImage*, vol. 16, no. 1, pp. 241 – 250, 2002.
- [83] KREHER, B., MADEER, I., and KISELEV, V., “Gibbs tracking: A novel approach for the reconstruction of neuronal pathways,” *Magnetic Resonance in Medicine*, vol. 60, pp. 953–963, 2008.
- [84] KREHER, B., SCHNEIDER, J., MADER, I., MARTIN, E., HENNIG, J., and IL’YASOV, K., “Multitensor approach for analysis and tracking of complex fiber configurations,” *Magnetic Resonance in Medicine*, vol. 54, pp. 1216–1225, 2005.
- [85] KUBICKI, M., MCCARLEY, R., WESTIN, C.-F., PARK, H.-J., MAIER, S., KIKINIS, R., JOLESZ, F. A., and SHENTON, M. E., “A review of diffusion tensor imaging studies in schizophrenia,” *J. of Psychiatric Research*, vol. 41, pp. 15–30, 2007.
- [86] LANKTON, S., MELONAKOS, J., MALCOLM, J., DAMBREVILLE, S., and TANNENBAUM, A., “Localized statistics for DW-MRI fiber bundle segmentation,” in *Mathematical Methods in Biomedical Image Analysis (MMBIA)*, pp. 1–8, 2008.
- [87] LAZAR, M. and ALEXANDER, A., “Bootstrap white matter tractography (Boot-Tract),” *NeuroImage*, vol. 24, pp. 524–532, 2005.
- [88] LAZAR, M., WEINSTEIN, D. M., TSURUDA, J. S., HASAN, K. M., ARFANAKIS, K., MEYERAND, M. E., BADIE, B., ROWLEY, H. A., HAUGHTON, V., FIELD, A., and ALEXANDER, A. L., “White matter tractography using diffusion tensor deflection,” *Human Brain Mapping*, vol. 18, pp. 306–321, 2003.
- [89] LEEMANS, A. and JONES, D. K., “A new approach to fully automated fiber tract clustering using affinity propagation,” in *Int. Symp. on Magnetic Resonance in Medicine (ISMRM)*, vol. 17, p. 856, 2009.
- [90] LEFEBVRE, T., BRUYNINCKX, H., and SCHUTTER, J. D., “Kalman filters for non-linear systems: a comparison of performance,” *International Journal of Control*, vol. 77, no. 7, pp. 639–653, 2004.
- [91] LENGLLET, C., DERICHE, R., and FAUGERAS, O., “Inferring white matter geometry from diffusion tensor MRI: Application to connectivity mapping,” in *European Conf. on Computer Vision*, pp. 127–140, 2004.

- [92] LIM, K. and HELPERN, J., “Applications of diffusion-weighted and diffusion tensor MRI to white matter diseases – a review,” *NMR in Biomedicine*, vol. 15, pp. 570–577, 2002.
- [93] LIN, C.-P., WEDEEN, V. J., CHEN, J.-H., YAO, C., and TSENG, W.-Y., “Validation of diffusion spectrum magnetic resonance imaging with manganese-enhanced rat optic tracts and ex vivo phantoms,” *NeuroImage*, vol. 19, pp. 482–495, 2003.
- [94] MADDAH, M., GRIMSON, W. E. L., WARFIELD, S. K., and WELLS, W. M., “A unified framework for clustering and quantitative analysis of white matter fiber tracts,” *Medical Image Analysis*, vol. 12, no. 2, pp. 191–202, 2008.
- [95] MADDAH, M., KUBICKI, M., WELLS, W., WESTIN, C.-F., SHENTON, M., and GRIMSON, W., “Findings in schizophrenia by tract-oriented DT-MRI analysis,” in *Medical Image Computing and Computer Assisted Intervention (MICCAI)*, 2008.
- [96] MALCOLM, J., RATHI, Y., and TANNENBAUM, A., “A graph cut approach to image segmentation in tensor space,” in *Component Analysis Methods (in CVPR)*, pp. 1–8, 2007.
- [97] MALCOLM, J. G., KUBICKI, M., SHENTON, M. E., and RATHI, Y., “The effect of local fiber model on population studies,” in *Diffusion Modeling and Fiber Cup (in MICCAI)*, pp. 33–40, 2009.
- [98] MALCOLM, J. G., MICHAILOVICH, O., BOUIX, S., WESTIN, C.-F., SHENTON, M. E., and RATHI, Y., “A filtered approach to neural tractography using the Watson directional function,” *Medical Image Analysis*, vol. 14, pp. 58–69, 2010.
- [99] MALCOLM, J. G., SHENTON, M. E., and RATHI, Y., “Filtered tractography: State estimation in a constrained subspace,” in *Diffusion Modeling and Fiber Cup (in MICCAI)*, pp. 122–133, 2009.
- [100] MALCOLM, J. G., SHENTON, M. E., and RATHI, Y., “Filtered tractography: Validation on a physical phantom,” in *Diffusion Modeling and Fiber Cup (in MICCAI)*, pp. 220–223, 2009.
- [101] MALCOLM, J. G., SHENTON, M. E., and RATHI, Y., “Neural tractography using an unscented Kalman filter,” in *Information Processing in Medical Imaging (IPMI)*, pp. 126–138, 2009.
- [102] MALCOLM, J. G., SHENTON, M. E., and RATHI, Y., “Two-tensor tractography using a constrained filter,” in *Medical Image Computing and Computer Assisted Intervention (MICCAI)*, vol. 12, pp. 894–902, 2009.
- [103] MALCOLM, J. G., SHENTON, M. E., and RATHI, Y., “Filtered multi-tensor tractography,” *Trans. on Med. Imag.*, vol. 29, pp. 1664–1675, 2010.
- [104] MALLAT, S. and ZHANG, Z., “Matching pursuits with time-frequency dictionaries,” *Trans. on Signal Processing*, vol. 41, pp. 3397–3415, 1993.
- [105] McGRAW, T., VEMURI, B., YEZIERSKI, B., and MARECI, T., “Von Mises-Fisher mixture model of the diffusion ODF,” in *Int. Symp. on Biomedical Imaging*, pp. 65–68, 2006.

- [106] MINATI, L. and WĘGONGLARZ, W. P., “Physical foundations, models, and methods of diffusion magnetic resonance imaging of the brain: A review,” *Concepts in Magnetic Resonance Part A*, vol. 30, no. 5, pp. 278–307, 2007.
- [107] MORI, S. and VAN ZIJL, P. C. M., “Fiber tracking: principles and strategies – A technical review,” *NMR in Biomedicine*, vol. 15, pp. 468–480, 2002.
- [108] NORRIS, D. G., “The effects of microscopic tissue parameters on the diffusion weighted magnetic resonance imaging experiment,” *NMR in Biomedicine*, vol. 15, pp. 438–455, 2001.
- [109] O’DONNELL, L., HAKER, S., and WESTIN, C.-F., “New approaches to estimation of white matter connectivity in diffusion tensor MRI: elliptic PDE’s and geodesics in tensor-warped space,” in *Medical Image Computing and Computer Assisted Intervention (MICCAI)*, pp. 459–466, 2002.
- [110] O’DONNELL, L., WESTIN, C.-F., and GOLBY, A., “Tract-based morphometry,” in *Medical Image Computing and Computer Assisted Intervention (MICCAI)*, pp. 161–168, 2007.
- [111] O’DONNELL, L. J. and WESTIN, C.-F., “Automatic tractography segmentation using a high-dimensional white matter atlas,” *Trans. on Med. Imag.*, vol. 26, pp. 1562–75, 2007.
- [112] O’DONNELL, L. J., WESTIN, C.-F., and GOLBY, A. J., “Tract-based morphometry for white matter group analysis,” *NeuroImage*, vol. 45, no. 3, pp. 832–844, 2009.
- [113] ÖZARSLAN, E. and MARECI, T., “Generalized diffusion tensor imaging and analytical relationships between diffusion tensor imaging and high angular resolution diffusion imaging,” *Magnetic Resonance in Medicine*, vol. 50, pp. 955–965, 2003.
- [114] ÖZARSLAN, E., SHEPHERD, T., VEMURI, B., BLACKBAND, S., and MARECI, T., “Resolution of complex tissue microarchitecture using the diffusion orientation transform,” *NeuroImage*, vol. 31, no. 3, pp. 1086–1103, 2006.
- [115] ÖZARSLAN, E., VEMURI, B. C., and MARECI, T. H., “Generalized scalar measures for diffusion MRI using trace, variance, and entropy,” *Magnetic Resonance in Medicine*, vol. 53, pp. 866–876, 2005.
- [116] PARKER, G. and ALEXANDER, D. C., “Probabilistic Monte Carlo based mapping of cerebral connections utilizing whole-brain crossing fiber information,” in *Information Processing in Medical Imaging (IPMI)*, pp. 684–696, 2003.
- [117] PARKER, G. and ALEXANDER, D. C., “Probabilistic anatomical connectivity derived from the microscopic persistent angular structure of cerebral tissue,” *Phil. Trans. R. Soc. B*, vol. 360, pp. 893–902, 2005.
- [118] PELED, S., FRIMAN, O., JOLESZ, F., and WESTIN, C.-F., “Geometrically constrained two-tensor model for crossing tracts in DWI,” *Magnetic Resonance in Medicine*, vol. 24, no. 9, pp. 1263–1270, 2006.

- [119] PERRIN, M., POUPON, C., COINTEPAS, Y., RIEUL, B., GOLESTANI, N., PALLIER, C., RIVIERE, D., CONSTANTINESCO, A., BIHAN, D. L., and MANGIN, J.-F., “Fiber tracking in Q-ball fields using regularized particle trajectories,” in *Information Processing in Medical Imaging (IPMI)*, pp. 52–63, 2005.
- [120] PICHON, E., WESTIN, C.-F., and TANNENBAUM, A., “A hamilton-jacobi-bellman approach to high angular resolution diffusion tractography,” in *Medical Image Computing and Computer Assisted Intervention (MICCAI)*, pp. 180–187, 2005.
- [121] POHL, K. M., KIKINIS, R., and WELLS, W. M., “Active mean fields: Solving the mean field approximation in the level set framework,” in *Information Processing in Medical Imaging (IPMI)*, pp. 26–37, 2007.
- [122] POUPON, C., RIEUL, B., KEZELE, I., PERRIN, M., POUPON, F., and MANGIN, J. F., “New diffusion phantoms dedicated to the study and validation of high-angular-resolution diffusion imaging (HARDI) models,” *Magnetic Resonance in Medicine*, vol. 60, no. 6, pp. 1276–83, 2008.
- [123] POUPON, C., ROCHE, A., DUBOIS, J., MANGIN, J.-F., and POUPON, F., “Real-time MR diffusion tensor and Q-ball imaging using Kalman filtering,” *Medical Image Analysis*, vol. 12, no. 5, pp. 527–534, 2008.
- [124] PRADOS, E., LENGLER, C., PONS, J., WOTAWA, N., DERICHE, R., FAUGERAS, O., and SOATTO, S., “Control theory and fast marching techniques for brain connectivity mapping,” in *Computer Vision and Pattern Recognition (CVPR)*, pp. 1076–1083, 2006.
- [125] QAZI, A., RADMANESH, A., O’DONNELL, L., KINDLMANN, G., PELED, S., WHALEN, S., WESTIN, C.-F., and GOLBY, A., “Resolving crossings in the corticospinal tract by two-tensor streamline tractography: Method and clinical assessment using fMRI,” *NeuroImage*, vol. 47, pp. 98–106, 2008.
- [126] RATHI, Y., MALCOLM, J. G., MICHAILOVICH, O., WESTIN, C.-F., SHENTON, M. E., and BOUIX, S., “Tensor-kernels for simultaneous fiber model estimation and tractography,” *Magnetic Resonance in Medicine*, vol. 64, no. 1, pp. 138–148, 2010.
- [127] RATHI, Y., MICHAILOVICH, O., SHENTON, M. E., and BOUIX, S., “Directional functions for orientation distribution estimation,” *Medical Image Analysis*, vol. 13, pp. 432–444, 2009.
- [128] RATHI, Y., MICHAILOVICH, O., and TANNENBAUM, A., “Segmenting images on the tensor manifold,” in *Computer Vision and Pattern Recognition (CVPR)*, 2007.
- [129] REISERT, M., MADER, I., and KISELEV, V., “Global reconstruction of neuronal fibres,” in *Diffusion Modeling and Fiber Cup (in MICCAI)*, pp. 70–81, 2009.
- [130] ROHLFING, T., SULLIVAN, E. V., and PFEFFERBAUM, A., “Regression models of atlas appearance,” in *Information Processing in Medical Imaging (IPMI)*, pp. 151–162, 2009.
- [131] ROUSSON, M., LENGLER, C., and DERICHE, R., “Level set and region based propagation for diffusion tensor MRI segmentation,” in *ECCV, Workshops CVAMIA-MMBIA*, 2004.

- [132] SAVADJIEV, P., CAMPBELL, J., PIKE, G., and SIDDIQI, K., “3D curve inference for diffusion MRI regularization and fibre tractography,” *Medical Image Analysis*, vol. 10, pp. 799–813, 2006.
- [133] SAVADJIEV, P., CAMPBELL, J. S., DESCOTEAUX, M., DERICHÉ, R., PIKE, G. B., and SIDDIQI, K., “Labeling of ambiguous subvoxel fibre bundle configurations in high angular resolution diffusion MRI,” *NeuroImage*, vol. 41, pp. 58–68, 2008.
- [134] SAVADJIEV, P., KINDLMANN, G., BOUIX, S., SHENTON, M. E., and WESTIN, C.-F., “Local white matter geometry indices from diffusion tensor gradients,” in *Medical Image Computing and Computer Assisted Intervention (MICCAI)*, pp. 345–352, 2009.
- [135] SCHULTZ, T. and SEIDEL, H., “Estimating crossing fibers: A tensor decomposition approach,” *Trans. on Visualization and Computer Graphics*, vol. 14, no. 6, pp. 1635–1642, 2008.
- [136] SIMON, D. and SIMON, D. L., “Kalman filtering with inequality constraints for turbopfan engine health estimation,” *IEE Proc.–Control Theory and Appl.*, vol. 153, no. 3, pp. 371–378, 2006.
- [137] SMITH, S. M., JENKINSON, M., JOHANSEN-BERG, H., RUECKERT, D., MACKAY, T. E., WATKINS, K. E., CICCARELLI, O., CADER, M. Z., MATTHEWS, P. M., and BEHRENS, T. E., “Tract-based spatial statistics: Voxelwise analysis of multi-subject diffusion data,” *NeuroImage*, vol. 31, pp. 1487–1505, 2006.
- [138] SPORNS, O., HONEY, C. J., and KÖTTER, R., “Identification and classification of hubs in brain networks,” *PLoS ONE*, vol. 2, no. 10, p. e1049, 2007.
- [139] TOURNIER, J.-D., CALAMANTE, F., and CONNELLY, A., “Robust determination of the fibre orientation distribution in diffusion MRI: Non-negativity constrained super-resolved spherical deconvolution,” *NeuroImage*, vol. 35, pp. 1459–1472, 2007.
- [140] TOURNIER, J.-D., CALAMANTE, F., GADIAN, D., and CONNELLY, A., “Diffusion-weighted magnetic resonance imaging fibre tracking using a front evolution algorithm,” *NeuroImage*, vol. 20, pp. 276–288, 2003.
- [141] TOURNIER, J.-D., CALAMANTE, F., GADIAN, D., and CONNELLY, A., “Direct estimation of the fiber orientation density function from diffusion-weighted MRI data using spherical deconvolution,” *NeuroImage*, vol. 23, pp. 1176–1185, 2004.
- [142] TSCHUMPERLÉ, D., *PDE-Based Regularization of Multivalued Images and Applications*. PhD thesis, University of Nice-Sophia Antipolis, 2002.
- [143] TUCH, D., *Diffusion MRI of Complex Tissue Structure*. PhD thesis, Massachusetts Institute of Technology, 2002.
- [144] TUCH, D., “Q-ball imaging,” *Magnetic Resonance in Medicine*, vol. 52, pp. 1358–1372, 2004.
- [145] TUCH, D., BELLIVEAU, J., and WEDEEN, V. J., “A path integral approach to white matter tractography,” in *Int. Symp. on Magnetic Resonance in Medicine (ISMRM)*, p. 791, 2000.

- [146] TUCH, D., REESE, T., WIEGELL, M., MAKRIS, N., BELLIVEAU, J., and WEDEEN, V., “High angular resolution diffusion imaging reveals intravoxel white matter fiber heterogeneity,” *Magnetic Resonance in Medicine*, vol. 48, pp. 577–582, 2002.
- [147] VAN DER MERWE, R. and WAN, E., “Sigma-point Kalman filters for probabilistic inference in dynamic state-space models,” in *Workshop on Advances in Machine Learning*, 2003.
- [148] VILANOVA, A., ZHANG, S., KINDLMANN, G., and LAIDLAW, D., “An introduction to visualization of diffusion tensor imaging and its applications,” in *Visualization and Processing of Tensor Fields*, ch. 7, pp. 121–153, Springer, 2006.
- [149] WANG, X., GRIMSON, W. E. L., and WESTIN, C.-F., “Tractography segmentation using a hierarchical dirichlet processes mixture model,” in *Information Processing in Medical Imaging (IPMI)*, pp. 101–113, 2009.
- [150] WASSERMANN, D., BLOY, L., KANTERAKIS, E., VERMA, R., and DERICHE, R., “Unsupervised white matter fiber clustering and tract probability map generation: Applications of a gaussian process framework for white matter fibers,” Tech. Rep. 7005, INRIA, 2009.
- [151] WEDEEN, V. J., HAGMANN, P., TSENG, W.-Y., REESE, T., and WEISSKOFF, R. M., “Mapping complex tissue architecture with diffusion spectrum magnetic resonance imaging,” *Magnetic Resonance in Medicine*, vol. 54, pp. 1377–1386, 2005.
- [152] WESTIN, C.-F., MAIER, S., MAMATA, H., NABAVI, A., JOLESZ, F., and KIKINIS, R., “Processing and visualizationfor diffusontensor MRI,” *Medical Image Analysis*, vol. 6, pp. 93–108, 2002.
- [153] WHITCHER, B., TUCH, D., WISCO, J., SORENSEN, A., and WANG, L., “Using the wild bootstrap to quantify uncertainty in diffusion tensor imaging,” *Human Brain Mapping*, vol. 29, no. 3, pp. 346–362, 2008.
- [154] YUSHKEVICH, P. A., ZHANG, H., SIMON, T. J., and GEE, J. C., “Structure-specific statistical mapping of white matter tracts,” *NeuroImage*, vol. 41, pp. 448–461, 2008.
- [155] ZHAN, W. and YANG, Y., “How accurately can the diffusion profiles indicate multiple fiber orientations? A study on general fiber crossings in diffusion MRI,” *J. of Magnetic Resonance*, vol. 183, pp. 193–202, 2006.
- [156] ZHANG, F., HANCOCK, E., GOODLETT, C., and GERIG, G., “Probabilistic white matter fiber tracking using particle filtering and von Mises-Fisher sampling,” *Medical Image Analysis*, vol. 13, pp. 5–18, 2009.
- [157] ZHUKOV, L. and BARR, A., “Oriented tensor reconstruction: Tracing neural pathways from diffusion tensor MRI,” in *Visualization*, pp. 387–394, 2002.